Quasi-Two-Dimensional Flamelet Models for a Three-Feed Non-Premixed Combustion System

余, 盼龍

https://doi.org/10.15017/2534447

Quasi-Two-Dimensional Flamelet Models for a Three-Feed Non-Premixed Combution System

KYUSHU
UNIVERSITY

Yu Panlong

Department of Mechanical Engineering
Kyushu University

This dissertation is submitted for the degree of
Doctor of Philosophy

July 2019

I would like to dedicate this thesis to my loving parents and wife.

Declaration

I hereby declare that except where specific reference is made to the work of others, the contents of this dissertation are original and have not been submitted in whole or in part for consideration for any other degree or qualification in this, or any other university. This dissertation is my own work and contains nothing which is the outcome of work done in collaboration with others, except as specified in the text and Acknowledgements. This dissertation contains fewer than 65,000 words including appendices, bibliography, footnotes, tables and equations and has fewer than 150 figures.

Yu Panlong
July 2019

Acknowledgements

Firstly, I would like to express my gratitude to my supervisor Prof. WATANABE Hiroaki, for indoctrinating me into the ways of flamelet model and computational fluid dynamics, for his limitless patience and continual encouragement. Secondly, I am sincerely grateful to Prof. KITAGAWA Toshiaki, for giving me the opportunity to do research in *reactive gas dynamics laboratory* and contineously providing me with helpful suggestions for my researches. I am deeply appreciated for Prof. KUROSE Ryoichi and his group members in Kyoto University for the in-house code FK^3 and other help. I benefited a lot from the valuable discussions with Dr. PILLAI Abhishek. I am also grateful to Prof. PITSCH Heinz in RWTH Aachen University, for the inspiring discussions and valuable suggestions. I would also like to thank Prof. TAKATA Yasuyuki for his helpful comments on a draft of this dissertation. In addition, I would like to thank Prof. NAGANO Yukihide, and postdoctoral fellow Dr. AHN Seongyool for their suggestions for my research. Besides, I also want to thank Dr. ZHANG Wei who graduated from our laboratory. He helped me a lot both in the research and daily life when I was a novice. When I was a student in Tianjin Univeristy, Prof. LI Xun introduced me the CFD first and cultivated my interest in this field. I want to show my greatest respect to him here.

I will never forget the period in *reactive gas dynamics laboratory* which is an international big family. I am really fortunately I am a member here, and I am grateful to all the other members in our laboratory. Members here are always accommodating and helpful, and they helped me get used to the life in Japan.

Last, I want to express my gratitude to my beloved family, especially my parents and my wife, for their steadfast support and encouragement. I also want to thank my good friends, thanks for giving me the encouragements.

Abstract

This dissertation mainly develops an extension of the one-dimensional flamelet progress-variable (FPV) approach in order to tackle with the issues in a three-feed non-premixed combustion system into which a diluent is injected. The conventional one-dimensional FPV is based on the two-feed counterflow system which is composed of a fuel port and an oxidizer port. Since the mixture fraction space is one-dimensional, for a one-dimensional flamelet model it cannot interpret the mixing flow in a three-feed system. However, the flamelet-based model is such a powerful approach which can not only allow us to get access to the detailed chemistry mechanism but also solve the temperature and species transport equations prior to the simulation; these make it appealing in terms of turbulent combustion issues. So it is of great significance to develop a flamelet-based model to address the three-feed non-premixed combustion challenges. In the current work, three quasi-two-dimensional flamelet (Q2DF) models are proposed, and they are validated by means of direct numerical simulation (DNS) first, afterwards, with proper modelings of the tracking parameters proposed they are also applied in large-eddy simulation (LES) on a lab-scale facility.

CO is a dominant composition in the three-feed non-premixed combustion system in this work, but it was pointed out that the CO concentration cannot be captured accurately by the FPV in some researches, and an unsteady flamelet model (USFM) is considered as a good remedy. However, the USFM is not desirable in the current research due to its excessive dimensions in the library. The purpose of this work is to develop a flamelet model with the additional dimension in it called the diluent fraction; the diluent fraction is the very focus. So the extension on the basis of the one-dimensional FPV would be favorable if the CO could be predicted reliably. Considering conditions have been varied from those researches, a priori test is necessary and of significance. A LES is applied in a lab-scale facility by means of the one-dimensional FPV, in which the CO is a product and plays an important role and coal tar species are taken into account. According to the results, the prediction of

the CO can achieve good agreement with the experimental data, and it is concluded that the FPV is suitable to be an extension base.

The Q2DF models in this work are derived based on the two-dimensional flamelet (2DF) model. By setting a zero scalar dissipation rate for the diluent stream mixture fraction in the three-feed counterflow system, the 2DF can be reduced to the one-dimensional flamelet model, and a series of one-dimensional flamelet libraries can be integrated by the parameter diluent fraction. These Q2DF models are derived from the 2DF, but the reduced flamelet model can still keep the influence of the third stream; this is the reason we call it quasi-two-dimensional flamelet model. These models are validated by DNS first, in which no turbulence model is employed. Comparisons are made between three model cases and a reference case in which the identical detailed mechanism coupled with the Arrhenius formation (ARF) is used. It has been confirmed that three Q2DF model cases can obtain good agreements with the ARF case, however, differences among the three models are not apparent.

To have further understanding of these models and apply them in the industry field, LES has been implemented. LES modelings for the Q2DF models are quite essential, and they would be complicate especially when the nonlinear connection for the mixture fractions turns up. Instead of solving the transport equations, the LES modelings for the mean value and its variance have been figured out directly based on the connection of the three mixture fractions in this work. According to the results by comparing the simulation and experiments, these modelings are confirmed to be quite effective and accurate. Based on the LES and flamelet formulations solving results, comparisons are made between Q2DF models and 2DF model in terms of the cross-scalar and scalar dissipation rates. It has been confirmed that the Q2DF models are essentially the 2DF model in which the cross-scalar and scalar dissipation rates are considered incompletely and diluent fraction is discretely distributed. Furthermore, the fluxes of the streams in the three-feed non-premixed combustion system also affect the performances of the Q2DF models through the tracking parameters such as mixture fraction with its variance, as well as the diluent fraction. Therefore, the models can be selected according to the dominant stream flux in the flow field. The best accuracy may could be achieved by the complete 2DF model, however, owing to too excessive dimensions of the library, especially in terms of the LES, it is still undesirable.

Contents

List of figures

List of tables

Nomenclature

Roman Symbols

Aa	Fluctuation magnitude
a_{ij}	Number of the atoms of the element j in a molecule of species i
C	Progress varible
c_{p}	Specific heat capacity
C_{t}	Smagorinsky coefficient
$D_{\phi_{\mathrm{i}}}$	Diffusivity of quantity ϕ_i
h	Total enthalpy
hi	Specific enthalpy of species i
J_{ϕ}^{sgs}	Residual subgrid scalar flux of quantity ϕ
k_b	Reaction rate coefficient of the backward reaction
k_f	Reaction rate coefficient of the forward reaction
M	Molecular weight
$\dot{m}_1$	Mass flux of the fuel stream
$\dot{m}_2$	Mass flux of the oxidizer stream
$\dot{m}_{3\mathrm{f}}$	Mass flux of the diluent stream put in on the fuel side
$\dot{m}_{3\mathrm{o}}$	Mass flux of the diluent stream put in on the oxidizer side
Sc_{t}	Schmidt number

S_{ij} Rate-of-strain tensor

Sta Strouch Number

U_f Fuel stream velocity

u_i Velocity vector

U_o Oxidizer stream velocity

V_k Diffusion velocity of species k

W_i Diluent fraction

Y_i Mass fracion of the species i

Z Mixture fracion

Z_1 Mixture fraction for fuel stream in a three-feed system

Z_2 Mixture fraction for oxidizer stream in a three-feed system

Z_3 Mixture fraction for diluent stream in a three-feed system

Z_j Mass fracion of element j

Greek Symbols

χ Scalar dissipation rate

χ_1 Scalar dissipation rate for fuel mixture fracion in a three-feed system

χ_2 Scalar dissipation rate for oxidizer mixture fracion in a three-feed system

χ_3 Scalar dissipation rate for diluent mixture fracion in a three-feed system

χ_{ij} Cross scalar dissipation rate in a three-feed system

χ_{ref} Reference scalar dissipation rate

χ_{st} Stoichiometric scalar dissipation rate

δ_{ij} Kronecker delta function

ε Transformed space base 1

η Transformed space base 2

Λ Reaction progress variable in stoichiometric condition

λ Thermal conductivity

μ_t Eddy viscosity

$\dot{\omega}$ Reaction term

ϕ_i A reactive scalar

ρ Mixture density

τ_{ij} Viscous stress tensor

ϑ Initial momentum thickness

Acronyms / Abbreviations

2DF Two-Dimensional Flamelet

ARF Arrhenius Formation

CCS CO2 Capture and Storage

CFD Computational Fluid Dynamics

CRIEPI Central Research Institute of Electric Power Industry

DNS Direct Numerical Simulation

FFR Front Flow Red

FPV Flamelet Progress-Variable

GHG Greenhouse Gas

HCOG Hot Coke Oven Gas

IGCC Integrated Gasification Combined Cycle

LES Large-Eddy Simulation

MILD Moderate or Intense Low Oxygen

PAH Polycyclic Aromatic Hydrocarbon

Q2DF Quasi-Two-Dimensional Flamelet

RANS Reynolds-Average Navier-Stokes

RMS Root mean square

SFM Steady Flamelet Model

USFM Unsteady Flamelet Model

WENO Weighted Essentially Non-Oscillatory

Chapter 1

Introduction

1.1 Background and Motivation

Besides searching energy alternatives and develop renewable energy sources, it is of great significance to make the most of the available fossil fuels since it is the dominant energy currently and will be the primary energy resource for the forseeable future. According to the U.S. Energy Information Administration (2018), the world energy consumption steadily increases and the fossil fuels account for a large share as shown in Figure 1.1. Although the renewable resource and nuclear energy are playing more and more important roles, fossil fuel is still the largest portion regarding the world net electricity generation as it is illustrated in Figure 1.2. The combustion of the fossil fuels is considered the primary reason of the emissions of the CO_2, making it a significant issue at the center of the climate change debate. According to the reports of the world energy, CO_2 emissions increase from 32.3 billion metric tons

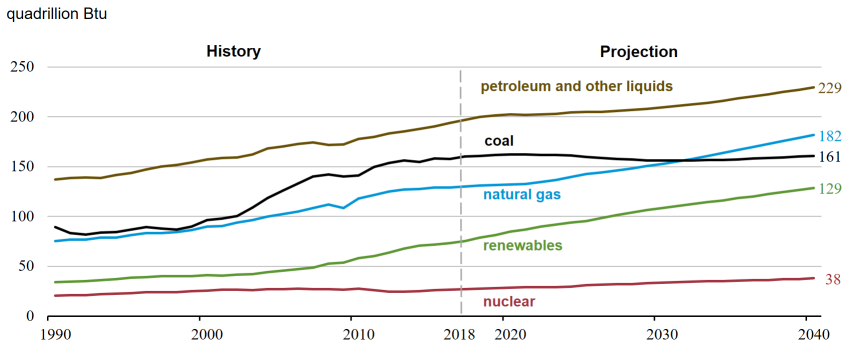

Fig. 1.1 Historic data and projected world energy comsumption by energy source. (Source: U.S. Energy Information Administration (2018).)

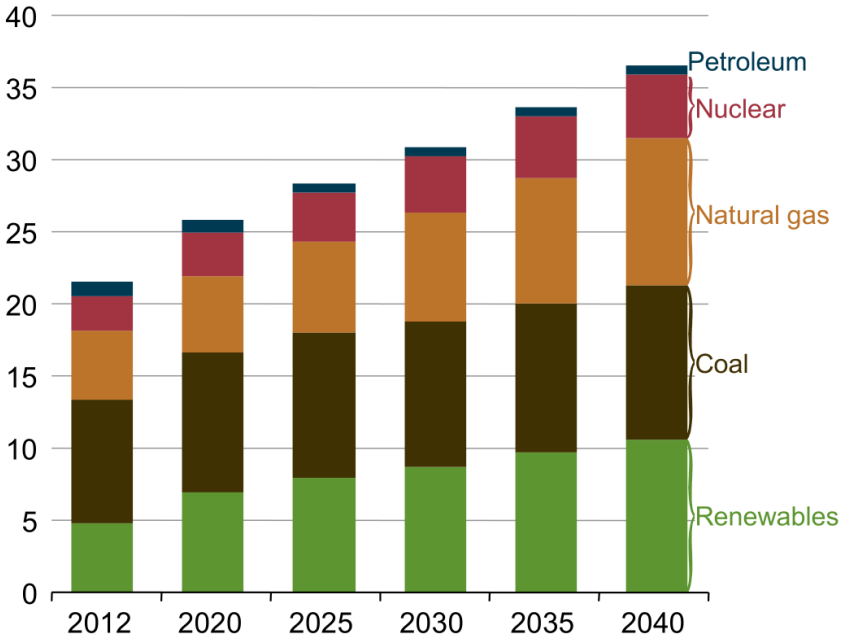

Fig. 1.2 Historic data and projected world net electricity generation by fuel types. (Unit: trillion kilowatthours, Source: U.S. Energy Information Administration (2016).)

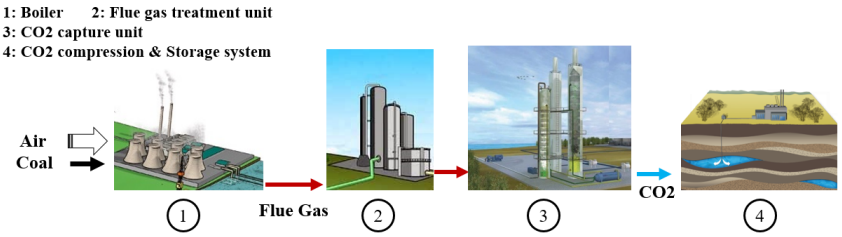

Fig. 1.3 Post combustion.

in 2012 to 35.6 billion metric tons in 2020, and it will achieve 43.2 billion metric tons in 2040 [1].

Various CO_2 capture and storage (CCS) technologies are developed for the sake of decreasing the greenhouse gas (GHG) emissions. With regard to the conventional coal-fired power plants, there are three typical CCS routes. The first one is to implement the CCS in the boiler flue gas, which is called the post-combustion, as shown in Figure 1.3. In this method, flue gas is led to the CO_2 capture units which is equipped with matured chemical absorption technology. However, other than the large absorb equipments, absorber regenerating costs large quantity of thermal energy and thus decreases the thermal efficiency. The second one is called the oxy-fuel combustion, as shown in Figure 1.4. In this proposal, the pure oxygen is injected to

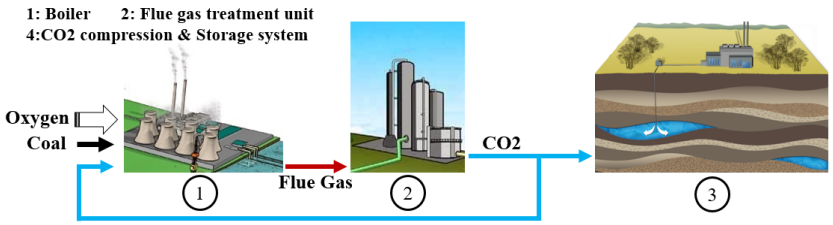

Fig. 1.4 Oxy-fuel combustion.

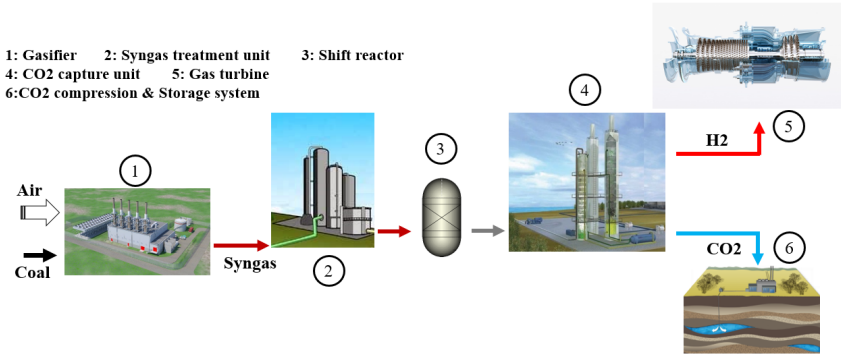

Fig. 1.5 Pre-combustion

the boiler, therefore, the CO_2 separation units are removed. But the air separation units are indispensable, and equipments are needed to control the furnace temperature. The above mentioned two cases are based on the conventional pulverized boiler combustion system. Figure 1.5 shows the the so-called pre-combustion method in which CO_2 is captured from the fuel prior to combustion in the integrated coal gasification combined cycle (IGCC) system. Although the CO_2 separation units are much smaller than that in the first case mentioned forgoing, the shift reactor for converting CO to CO_2 is required which is mainly responsible for the the thermal efficiency decrease. The applications of these conventional CCS routes reduce about 10% of the net thermal efficiency [2], which motivates researchers to find a more efficient and effective solution.

Oki et al. proposed a new concept that combines IGCC and CCS, namely the oxy-fuel IGCC [3, 2, 4]. In this proposal, the shift converter and CO_2 separation apparatus are removed, and part of the recirculated CO_2 is conducted to the gasification process and the gas turbine. Pure oxygen and fuel are also injected into the gas turbine combustion chamber, forming a three-feed non-premixed combustion system, as Figure 1.6 shown. With respect to the gas turbine, the CO_2 concerntration is so high and the specific heat ratio is quite small, which makes the inlet and outlet temperature

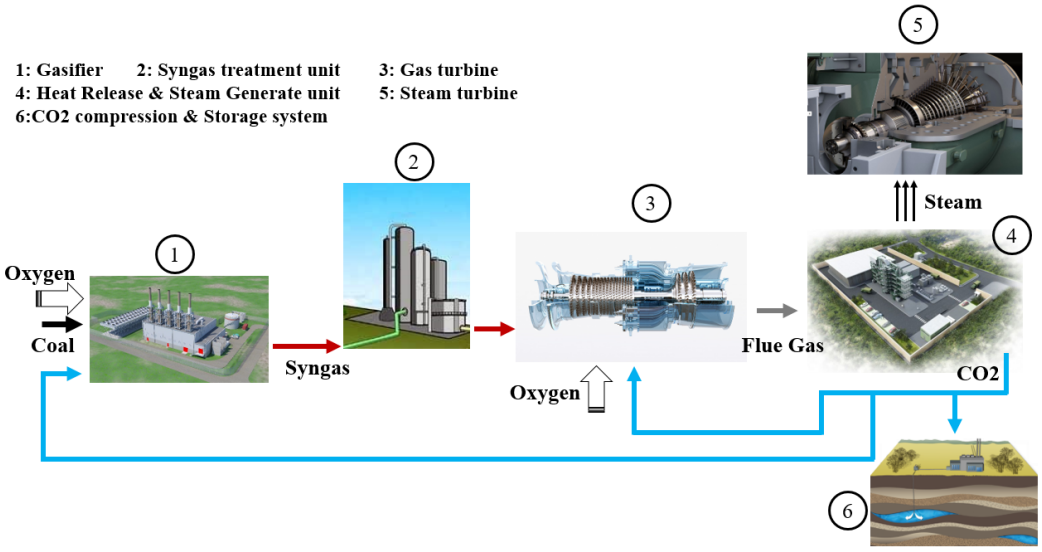

Fig. 1.6 Oxy-fuel combined with IGCC

difference is smaller than that in the conventional IGCC system. And finally the thermal efficiency in this system achieves more than 40% after the CCS treatment.

In order to have a deeper insight of the mixing flow in this three-feed non-premixed combustion system, both experiments and numerical simulation are necessary. Owing to the complexity of the system and the cost of the experimental study, the advantages of the numerical simulation are appealing [5]. By means of the computational fluid dynamics (CFD) method, it is expected to reduce the cost and make it much lower than that in the experimental investigation. Furthermore, numerical simulation can provide remarkable speed regarding to the research process and development cycle. Although the deviations are inevitable due to the ideal conditions adopted in the numerical simulations, it allows the researchers to obtain access to the complete information of interests, which may be limited by the experimentations.

Generally speaking, numerical simulation of combusition issues include two large parts: turbulent flow and chemical reaction. Chemical reactions are of the great interests of combustion, as hundreds and thousands complicated reactions are invovled in the processes which still remain to be explored. Various chemistry models for combustion are exist and being developed, and one of the most promising ones is the flamelet model. The flamelet models enable researchers to get access to the fully detailed chemical mechanisms. In addition, optimized and efficient tabulated techniques provide a mapping of a flamelet library in turbulent combustion simulations [6], which greatly reduces computational cost. With these attractive merits, the developments of the flamelet model have never been stopped since it has

been proposed. The conventional one-dimensional flamelet model is established on the basis of two-feed counterflow system and interprets all events of the reacting flows in an one-mixture-fraction space. As for the three-feed non-premixed combustion system mentioned forgoing, since three mixture fractions for the corresponding three streams exist, the one-dimensional flamelet model is insufficient to tackle with the chemistry events any more. In order to employ the flamelet-based model to have deeper understanding for the mixing and interaction in the three-feed non-premixed combustion system, an extension is necessary.

1.2 Non-premixed Flamelet Model and Literature Survey

Flamelet formulations in the mixture fraction space with the scalar dissipation rate for the mixing process is originally proposed and developed by Peters [7, 8]. Flamelet is a thin reaction zone structure that is embedded in the turbulent flow field. Since the reaction timescale is much smaller than that of the mixing process, it is reasonable to assume that the chemical reactions are so fast that they occur in these reaction zone structures around the stoichiometric mixture on a scale smaller than the size of Kolmogorov eddy. This flamelet assumption leads to two fundamental consequences [9]: First, the reaction structure can be considered as locally laminar and then the diffusive transports occur mainly, especially in the stoichiometric mixture normal direction. On the other side, scalar transports can be expressed in the mixture fraction space.

Reacting speices are consumed and generated in the chemical reactions, but the chemical elements are conserved during these processes. For a particular chemical element j, no matter how many streams exist and how many reactions occur, its mass fraction Z_j should be kept unvaried if the initial and boundary conditions were fixed.

$$Z_j = \sum_{i=1}^{n} \frac{a_{ij} M_j}{M_i} Y_i, \tag{1.1}$$

here, i is the number of the species, j is the particular element j, a_{ij} is the number of the atoms of the element j in a molecule of species i, M is the molecular weight and Y_i is the mass fraction of the species i. In terms of each stream, the correspoding particular chemical element mass fraction based on the total mass of all streams should be also conserved. So, for a particular stream, the mass fraction of the total

elements should be also conserved and can be expressed as follows:

$$Z = \sum_{j=1}^{k} Z_j = \sum_{j=1}^{k} \sum_{i=1}^{n} \frac{a_{ij} M_j}{M_i} Y_i, \tag{1.2}$$

here, k is the element number in a particular stream. It can be easily observed that this Z is equal to the mass fraction of the corresponding stream. If Z is defined for the fuel stream mixture fraction, then for a two-feed system:

$$Z = \frac{\dot{m}_1}{\dot{m}_1 + \dot{m}_2}, \tag{1.3}$$

here, $\dot{m}_1$ is the mass flux of the fuel stream and $\dot{m}_2$ is the mass flux of the oxdizer stream.

As it is mentioned above that the mixture fraction is a conserved scalar, then it would be transported without a source term or a sink term.

$$\frac{\partial \rho Z}{\partial t} + \frac{\partial \rho u_i Z}{\partial x_i} = \frac{\partial}{\partial x_i} \left(\rho D_{\mathrm{z}} \frac{\partial Z}{\partial x_i} \right), \tag{1.4}$$

or sometimes expressed as:

$$\rho \frac{\partial Z}{\partial t} + \rho u_i \frac{\partial Z}{\partial x_i} = \frac{\partial}{\partial x_i} \left(\rho D_{\mathrm{z}} \frac{\partial Z}{\partial x_i} \right), \tag{1.5}$$

here, D_z is the mixture fraction diffusivity, and in the present work the diffusivity of a specific scalar ϕ for species k will be written as $D_{\phi_{\mathrm{k}}}$, and it would be put as D hereafter if the unity Lewis number assumption was adopted. In the above transport equation ρ is the density, and u_i is the velocity. According to the mixture fraction transport, mixture fraction can provide the information of the the stream mixing.

The flamelet formulations can be derived from the two-scale asymptotic analysis [8]. Here the scalar transport in the mixture fraction space will be derived by another approach. For a reactive scalar (species mass fraction), it can be transported in the physic space as:

$$\underbrace{\frac{\partial \rho \phi_k}{\partial t}}_{\text{the unsteady term}} + \underbrace{\frac{\partial \rho u_i \phi_k}{\partial x_i}}_{\text{the convection term}} = \underbrace{\frac{\partial}{\partial x_i} \left(\rho D_{\phi_{\mathrm{k}}} \frac{\partial \phi_k}{\partial x_i} \right)}_{\text{the diffision term}} + \underbrace{\rho \dot{\omega}_{\phi_{\mathrm{k}}}}_{\text{the reaction term}} . \tag{1.6}$$

In the above equation t is the time and ω_{ϕ_k} is the corresponding reaction rate. The connection between the physic space and the mixture fraction can be expressed as:

$$\frac{\partial}{\partial x_i} = \frac{\partial}{\partial Z}\frac{\partial Z}{\partial x_i}, \tag{1.7}$$

and in the mixture fraction space

$$\frac{\mathrm{d}}{\mathrm{d}t} = \frac{\partial}{\partial Z}\frac{\mathrm{d}Z}{\mathrm{d}t} + \frac{\partial}{\partial t}, \tag{1.8}$$

assuming that ρ is constant (ignore the compressibility) then

$$\frac{\mathrm{d}\phi_k}{\mathrm{d}t} = \frac{\partial \phi_k}{\partial Z}\frac{\mathrm{d}Z}{\mathrm{d}t} + \frac{\partial \phi_k}{\partial t} = \frac{\partial \phi_k}{\partial Z}\frac{\partial}{\partial x_i}\left(D_z\frac{\partial Z}{\partial x_i}\right) + \frac{\partial \phi_i}{\partial t} = \frac{\partial}{\partial x_i}\left(D_{\phi_k}\frac{\partial \phi_k}{\partial x_i}\right) + \rho\dot{\omega}_{\phi_k}, \tag{1.9}$$

and then

$$\frac{\partial \phi_k}{\partial t} = \frac{\partial}{\partial x_i}\left(D_{\phi_\mathrm{k}}\frac{\partial \phi_k}{\partial x_i}\right) - \frac{\partial \phi_k}{\partial Z}\frac{\partial}{\partial x_i}\left(D_\mathrm{z}\frac{\partial Z}{\partial x_i}\right) + \rho\dot{\omega}_{\phi_\mathrm{k}}. \tag{1.10}$$

Introducing the unity Lewis number assumption which is given by

$$\rho D = \lambda / c_\mathrm{p}, \tag{1.11}$$

where λ is the thermal conductivity and c_p is the specific heat capacity of the mixture gas at contant pressure. Then Eq.(1.10) can be transferred to:

$$\frac{\partial \phi_k}{\partial t} = D\left(\frac{\partial^2 \phi_k}{\partial x_i^2} - \frac{\partial \phi_k}{\partial Z}\frac{\partial^2 Z}{\partial x_i^2}\right) + \rho\dot{\omega}_{\phi_\mathrm{k}}. \tag{1.12}$$

Knowing that:

$$\frac{\partial^2 \phi_k}{\partial x_i^2} = \frac{\partial}{\partial x_i}\left(\frac{\partial \phi_k}{\partial x_i}\right) = \frac{\partial}{\partial x_i}\left(\frac{\partial \phi_k}{\partial Z}\frac{\partial Z}{\partial x_i}\right) = \frac{\partial \phi_k}{\partial Z}\frac{\partial^2 Z}{\partial x_i^2} + \frac{\partial Z}{\partial x_i}\frac{\partial^2 \phi_k}{\partial x_i \partial Z}, \tag{1.13}$$

and in Eq.(1.13), the second derivative of ϕ_k can be replaced

$$\frac{\partial^2 \phi_k}{\partial x_i \partial Z} = \frac{\partial}{\partial x_i}\frac{\partial \phi_k}{\partial Z} = \frac{\partial}{\partial Z}\frac{\partial Z}{\partial x_i}\frac{\partial \phi_k}{\partial Z} = \frac{\partial^2 \phi_k}{\partial Z^2}\frac{\partial Z}{\partial x_i}. \tag{1.14}$$

Considering the above Eq.(1.4)$\sim$(1.14)

$$\rho\frac{\partial \phi_k}{\partial t} = \rho\frac{\chi}{2}\frac{\partial^2 \phi_k}{\partial Z^2} + \rho\dot{\omega}_{\phi_k}. \tag{1.15}$$

here, ϕ_k can be the mass fraction for species k, and χ is the scalar dissipation rate of the mixture fraction which can be expressed by

$$\chi = 2D\left(\frac{\partial Z}{\partial x_i}\right)\left(\frac{\partial Z}{\partial x_i}\right). \tag{1.16}$$

The total enthalpy can be expressed as [10]:

$$\begin{aligned} \frac{\partial \rho h}{\partial t} + \frac{\partial \rho u_i h}{\partial x_i} = \\ \frac{\partial p}{\partial t} - \frac{\partial q_i}{\partial x_i} + \frac{\partial \tau_{ij} u_i}{\partial x_j} + \dot{Q} + \rho \sum_{k=1}^{N} Y_k f_{k,i}\left(u_i + V_{k,i}\right). \end{aligned} \tag{1.17}$$

Here, h is the total enthalpy, N is the total number of the species, p is the pressure, $\dot{Q}$ is the heat source term, τ_{ij} is the stress tensor, f_k is the volume force, $V_{k,i}$ is the i-component of the diffusion velocity (V_k) of species k which is given by Fick's Law form:

$$\begin{aligned} \sum_{k=1}^{N} Y_k V_{k,i} = 0, \\ V_k = -D_k \frac{1}{Y_k}\frac{\partial Y_k}{\partial x_i}. \end{aligned} \tag{1.18}$$

In the Eq. (1.17) q_i is the heat flux and can be expressed as:

$$q_i = -\lambda \frac{\partial T}{\partial x_i} + \rho \sum_{k=1}^{N} h_k Y_k V_{k,i} \tag{1.19}$$

here h_k is the specific enthalpy of species k. Ignore the viscous dissipation and assume constant pressue field, neglect the body force as well as heat loss. The the total enthalpy will be simplified to:

$$\begin{aligned} \frac{\partial \rho h}{\partial t} + \frac{\partial \rho u_i h}{\partial x_i} &= -\frac{\partial q_i}{\partial x_i} \\ &= \frac{\partial}{\partial x_i}\left(-\lambda \frac{\partial T}{\partial x_i} + \rho \sum_{k=1}^{N} h_k Y_k V_{k,i}\right). \end{aligned} \tag{1.20}$$

And the relation between enthalpy and temperature can be also described as:

$$\frac{\partial h}{\partial x_i} = c_{\mathrm{p}} \frac{\partial T}{\partial x_i} + \sum_{k}^{N} h_k \frac{\partial Y_k}{\partial x_i}. \tag{1.21}$$

Here, the T is the temperature, h_k is the specific enthalpy of species k. Combine Eqs. (1.20) and (1.21) then the temperature can be expressed as:

$$\frac{\partial \rho T}{\partial t}+\frac{\partial \rho u_i T}{\partial x_i}=\frac{\partial}{\partial x_i}\left(\lambda\frac{\partial T}{\partial x_i}\right)-\sum_{k=1}^{N}\rho c_{\mathrm{p,k}}Y_k V_{k,i}\frac{\partial T}{\partial x_i}-\sum_{k=1}^{N}\rho h_k\dot{\omega}_{\mathrm{Y_k}}. \tag{1.22}$$

Transfer the physical space to mixture fraction space then:

$$\rho\frac{\partial T}{\partial t}=\rho\frac{\chi}{2}\left(\frac{\partial^2 T}{\partial Z^2}+\frac{1}{c_{\mathrm{p}}}\frac{\partial c_{\mathrm{p}}}{\partial Z}\frac{\partial T}{\partial Z}\right)-\sum_{k}^{N}\frac{\rho\chi}{2}\left(\frac{\partial Y_k}{\partial Z}+\frac{Y_k}{M}\frac{\partial M}{\partial Z}\right)\times\left(1-\frac{c_{\mathrm{p,k}}}{c_{\mathrm{p}}}\frac{\partial T}{\partial Z}\right)-\frac{\rho}{c_{\mathrm{p}}}\sum_{k}^{N}(h_k\dot{\omega}_{\mathrm{Y_k}}). \tag{1.23}$$

Here $c_{\mathrm{p,k}}$ is the specific heat capacity of species k at contant pressure, and M is the mean molecular weight of the mixture. As it is observed that the velocity is not imposed continuity and momentum equations are no need to solve in the mixture fraction space. Ignoring the unsteady term since the reactions are assumped to be very fast, then Eqs. (1.15) and (1.23) can be transferred to one-dimensional steady flamelet model (SFM), combined with equation of state they can be solved to generate flamelet library.

χ plays a very important role in the non-premixed flamelet model. It is interesting if we viewed the definition of the scalar dissipation rate from another perspective:

$$\chi=2\times\underbrace{\left(\frac{\partial Z}{\partial x_i}\right)}_{\text{mixture fraction gradient}}\times\underbrace{\left[D\left(\frac{\partial Z}{\partial x_i}\right)\right]}_{\text{mixture fraction diffusion velocity}}. \tag{1.24}$$

The mixture fraction is a conserved scalar, neither consumption nor generation in the gas phase combustion. The gradient of the mixture fraction can be attributed to both convection and diffusion, then the χ can be symbolic of the convection and diffusion ability, and the dissipation does not mean consumption. The scalar dissipation rate can be also assumed as

$$\chi(Z)=\frac{a_s}{\pi}\exp\{-2[\mathrm{erfc}^{-1}(2Z)^2]\}. \tag{1.25}$$

Here erfc^{-1} is the inverse of the complementary error function [7, 11]. a_s is the strain rate and can be discribed as $(U_f+U_o)/L$ in the two-feed counterflow system, where the U_f and U_o are the velocity in the fuel side and oxidizer side, repectively, and L is the distance of the two ports. This expression indicates the scalar dissipation rate is

associated with the maximum velocity gradient. In the mixture fraction space, there is no velocity as mention above, which means that the combustion in the mixture fraction space is just a laminar diffusion-reaction process. It should be noted that this mixture space is an unsteady straining environment which is created by the turbulent flow, in which mixture fraction transported by Eq. (1.4).

According to Eq. (1.15), the variables can be expressed as a function of the mixture fraction and scalar dissipation rate, and the scalar dissipation rate connects the mixture fraction space with the physical space. The fuction can be expressed as:

$$\phi_i = \phi_i(Z, \chi). \tag{1.26}$$

The scalar dissipation rate can be stated by its stoichiometric value [12]

$$\chi(Z) = \chi_{\text{ref}} \frac{f(Z)}{f(Z_{\text{ref}})}, \tag{1.27}$$

here the $f(\phi)$ is related to the erfc^{-1}, the Z_{ref} and χ_{ref} are the stoichiometric mixture fraction and scalar dissipation rate, respectively. Then the expression of the function can be transferred to

$$\phi_i = \phi_i(Z, \chi_{\text{ref}}). \tag{1.28}$$

The stoichiometric scalar dissipation rate is also the scalar dissipation rate in the physical flow field, thus the stoichiometric scalar dissipation rate is used as a reference to generate the flamelet state in the mixture fraction space. Those generated flamelet states constitute the flamelet library in which all the chemical states can be indentified. However, looking up the library by the Eq.(1.28) will give rise to ambiguity since the chemical state can be stable or unstable burning, or even extinction for a specific scalar dissipation rate. Figure 1.7 is the S-shaped curve for a case in Chapter 2, in which the intersection points 1, 2, 3 between the S-shaped curve and the dashed line are corresponding to the stable burning, unstable burning, and the extinction state. Pierce and Moin [13] then originally extended the diffusion flamelet model to the FPV approach which can overcome this ambiguity. Mixture fraction does not contain any information about the chemical reaction in the mixing flow, thus it cannot account for the chemical variations progress in the directions perpendicular to its gradient. So, an additional reactive scalar is needed; this scalar is the very progress variable. A reaction progress parameter Λ is introduced. Combined with the mixture fraction, this reaction progress parameter is assumed can identify the

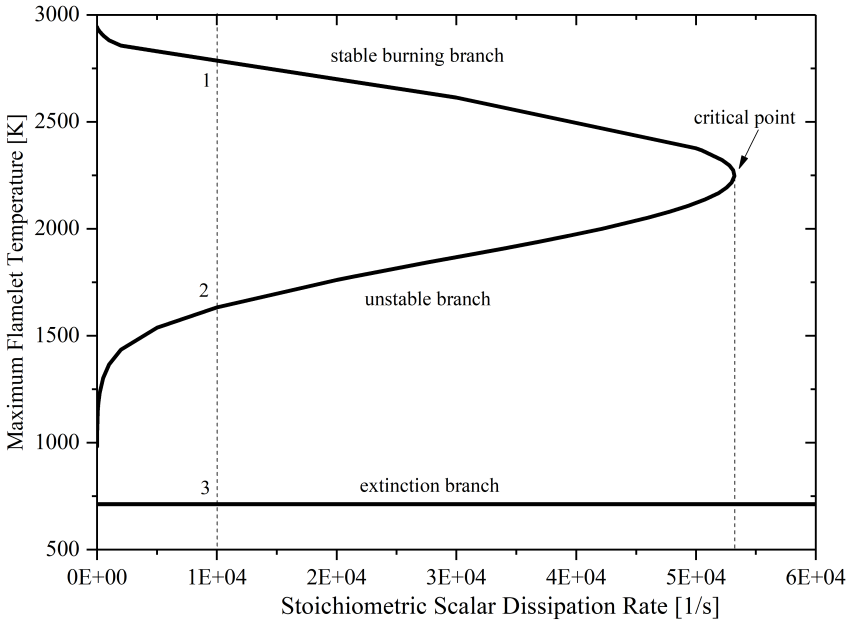

Fig. 1.7 Typical S-shaped curve for the flamelets.

chemical state uniquely along the S-shaped curve, and can be given as:

$$\phi = \Psi_\phi(Z,\Lambda). \tag{1.29}$$

Here, Λ equals to the stoichiometric conditioned progress variable C [14], and this is the fundamental difference between Λ and C. The tracking parameter χ can be replaced by Λ if its transport equation can be solved. However, the unclosed terms in the transport equation is difficult to model [15, 16], so Λ cannot be used directly. The progress varible C can be mapped from the flamelet library as

$$C = \Psi_C(Z,\Lambda). \tag{1.30}$$

Since C reflects the reaction progress and it is reasonable to assume that Ψ_C is a strict monotonic function. Thus Λ can be expressed as a function of the mixture fraction and the progress variable can be given as

$$\Lambda = \Psi_C^{-1}(Z,C). \tag{1.31}$$

Combined with Eq.(1.29), then

$$\phi = \Psi_\phi(Z,\Psi_C^{-1}(Z,C)). \tag{1.32}$$

So with solving the transport equation of Z and C, the library can be looked up and all chemical states can be tracked by Z and C.

There are various definitions of C [17], and it should be stressed that the progress variable selection should provide a unique mapping of all chemical states in the library. In the current work, the progress variable is defined as the sum of the mass fraction for four species and it can be expressed as

$$C = Y_{CO_2} + Y_{H_2O} + Y_{CO} + Y_{H_2}. \tag{1.33}$$

Sometimes researchers stated that the components are the product gases [14, 18, 19], but this maybe not strict enough since those components can be the species both in the feeds and products. However, it is reasonable to express that these four species are product species since these four speceis are neither exist in the issued streams nor in the initial flow filed in their researches.

The FPV exhibits great potential and is proved to be powerful for its application in many aspects. It was applied in a lab-scale burner for pulverized coal combustion [20, 21] and obtained reliable results. It was also extended and used for the spray flame [22, 18, 19, 23, 24] to investigate the characteristics and a deeper understanding have been achieved. And it was also developed to be the non-adibatic flamelet model [25–27] by changing the source term of the enthalpy when the heat loss is considered. The unsteady flamelet model (USFM) has also been developed [28] and used in the prediton of a lift-off flame [29, 30].

These are based on the two-feed combustion system, as for a three-feed combustion system, many researchers have also made great efforts. Besides maintaining high thermal efficiency, moderate or intense low oxygen dilution (MILD) combustion is a promising technology to reduce the emissions of nitrogen oxides as well as carbon monoxide [31]. Some experimenatal researches have shown that the thin reaction zones and flamelet-like structures exist in the MILD combustion [32, 33], which is also consistant with the DNS results [34, 35]. One of the MILD combustion modes is the jet-in-hot-coflow [36], and it has been confirmed that the one-dimensional SFM is inadequate for predicting characteristics [37] of this three streams system. However, by adding additional parameter called the oxidizer split in the extended FPV the prediction had been improved greatly [38, 39]. The oxidizer split is 0 in the coflow stream while it is unity in the oxidizer stream, and then the oxidizer split transport equation in the flow field for large-eddy simulation (LES) can be solved. The connection between the diluent coflow and the air stream has been considered by

the oxidizer split. It is essential to interpret the diluent interaction effects in MILD combustion [40], especially in the jet-in-hot-coflow three streams system. The conventional SFM, which is based on two independent feeds in a one-mixture-fraction space, is insufficient for describing the mixing processes that occur in the three-feed system, which means, compared with the one-dimensional flamelet model, more dimensions in the flamelet model would be favorable for the multiple-feed system. Hasse and Peters have derived the two-dimensional flamelet equations, and successfully simulated pressure and NO_x for split injections in a direct-injection Diesel engine by solving the Reynolds-average Navier–Stokes equations [41]. Based on their work, Felsch et al. [42] further extended the representative interactive flamelet model (RIF) [43] and attempted to account for an arbitrary number of injections, and good results were achieved. DNS coupled with a two-dimensional unsteady flamelet formulation was used to model auto-ignition of a multiple-feed system by Doran et al. [44], who obtained quite accurate prediction. LES of the two-dimensional flamelet model has not been implemented yet owing to its complexity. Instead of solving the two-dimensional flamelet formations, some researchers have chosen to extend the one-dimensional flamelet model by considering relationships among the three streams. Watanabe et al. [45] viewed the fuel gas that emanated from the volatile and the char as two separated fuel streams, and introduced a parameter to relate the two corresponding fuel mixture fractions. A series of one-dimensional flamelet libraries were generated, and they were shown to be accurate when their predictions were compared with the detailed chemistry case via DNS. They further applied this model to a large-scale test furnace with an actual pulverized coal burner by LES without providing information about the mixture fraction variance [46]. By means of the same flamelet model to predict the coal combustion, M. Rieth et al. solved a transport equation for the mixture fraction variance in their LES case [47]. For these LES studies, although good agreements between the simulations and the experiments were obtained overall, the reason for the discrepancies is not clear in terms of the extended flamelet models themselves, and the essence of the models is yet to be unveiled. To have a better understanding of the model and to clarify the existing discrepancies, further studies are needed; moreover, simpler but accurate models for the tracking parameters in LES modeling would be favorable.

1.3 Aims and Objectives

Considering the above disscussions, it is worth trying to employing the flamelet-based model for the three-feed non-premixed combustion system. But the conventional FPV is inadequate to account for the chemistry variations for the three-stream mixing flows. In order to have a better understanding of mixing process and interaction of the the three streams, and also to contribute to the design of the related combsution devices, extending the FPV for the three-feed non-premixed combustion system is of great significance.

The objective of this work is the development of flamlelet models for the three-feed non-premixed combustion system. Researches on the flamelet-based models in the present work are based on the DNS and LES employing a detailed mechanism for syngas combustion. The DNS and LES results are analyzed and discussed specifically to explore the following points based on the above literature survey:

- As it was pointed out that the conventional FPV could not capture the CO accurately, but CO is a dominant species in the syngas. It is advisable to develop a flamelet model based on the conventional FPV, or any modifications are prerequisite concerning the CO reaction term in its transport equation?
- The extention direction is toward to three-feed non-premixed combustion system which means three mixture fractions exist. What kind of the extension can consider the three mixture fraction appropriately? The two-dimensional flamelet model is an option of course, but what is the advantage and disadvantage? Is there any other approach that can achieve the purpose?
- If there is other approach that can be adopted, what is the difference compared with the two-dimensional flamelet model? Can the difference be physically interpreted or not? If the model is reasonable, how is its performance without any turbulence model employed?
- If the extended model can be validated by DNS, how can we make it appliable by LES?
- What is the essence of the model and how can we improve the prediction in the future work?

These questions will be tackled in this thesis in Chapter 2, 3 and 4. A priori test of the FPV will be implemented concerning the CO prediction first in chapter 2. In

chapter 3 extensions of the FPV will be performed with regarding to the three-feed non-premixed combustion system. And DNS will be performed for the validation. Afterwards, LES modeling of the extended FPV model will be implemented in chapter 4. The LES results will be used to compared with the experimental data to validate the LES modeling. In addition, a comprehensive analysis and discussion will be made to explore the essence of the extended model. The conclusions are presented in chapter 5.

Chapter 2

A Priori Test of an Extended FPV by LES

2.1 Background and Objectives

It is considered difficult to capture CO by the conventional FPV according to some researches [13, 28]. In these researches, CO is a species with a low concentration. Our extension of the flamelet model in this work is supposed to target for the three-feed non-premixed combustion system in which the syngas is composed of H_2 and CO with the CO is the dominant composition. So it is necessary to check the performance of the SFM in prediction of CO. In this chapter, the one-dimensional SFM is coupled with LES to predict H_2 and CO in a hot coke oven gas (HCOG) reforming process in which both the H_2 and CO play important roles, and the results will be compared with experimental data. It is worth mentioning in this work, the treatments of polycyclic aromatic hydrocarbon (PAH) is a valuable reference for the raw syngas that contains coal tar.

According to the data from the World Coal Association, nowadays, 70% of steel production all over the world uses coal [48]. In the coking process of steel mills, considerable coke oven gas as a by-product was generated [49], and various routes of its utilization were reported [50]. Jess explored the kinetics of the thermal conversion of modeled coke oven gas in a tubular flow reactor [51]. Hydrogen, steam, naphthalene, toluene, and benzene were used as model compounds. Based on his experimental data, Norinaga et al. performed a detailed chemical kinetic modeling approach to simulate the thermal conversion rate of this modeled coke oven gas and

it was proved to be reliable [52]. They also attempted to use this detailed chemical kinetic model to predict a non-catalytic partial oxidation of HCOG, and the influence of the oxygen concentration in the inlet gas mixture was investigated [53]. In the meanwhile, Norinaga et al. developed a reforming technology of HCOG to obtain products which were suitable for the methanol production [54]. A tubular reactor with four oxygen injectors installed, which was also used in our present study, was used to partially oxidize the HCOG, and the most suitable reforming conditions has been identified. Based on their work, coupling with a detailed kinetic chemical model consisting 2216 reactions with 257 species, a plug flow model and a one-dimensional axial diffusion model were employed by Appari et al. to simulate the reacting flow of the partially oxidized HCOG [55]. By means of the models, both the temperature along the axial length of the reactor and the species concentration of the reactor outlet shared good agreement with the experimental data. However, this research was on the premise of one-dimensional simulation and some other ideal assumptions. In order to capture the features of reacting flow under a more realistic flow condition, Li et al. implemented a three-dimensional CFD simulation [56]. A reduced chemical mechanism with 410 reactions and 47 species was employed, but they conceded that the Reynolds-average Navier-Stokes (RANS) model they used has its limitation.

In this Chapter, LES coupled with an extended FPV approach will be implemented on the HCOG reforming on the same facility in the literature [54, 56]. One of the purposes of this study is to check the CO prediction by the extended FPV approach since CO are the main products with high concentration. The extended FPV approach used in this chapter is based on the conventional FPV which was reviewed in chapter 1. In addition, the performance of the extended FPV approach in this chapter is also can be used as a reference for the raw syngas that contains coal tar. This study will provide reference for the flamelet model extention in chapter 3 and chapter 4.

2.2 Methodology

2.2.1 Governing equations

The governing equations in this study are the mass, momentum, and energy conservation equations presented in Eqs. (2.1), (2.2) and (2.3) respectively. Additional transport equations for the mixture fraction and the progress variable as well as the

PAH species mass fraction are solved by using Eqs. (2.4)∼(2.6).

$$\frac{\partial \overline{\rho}}{\partial t} + \frac{\partial (\overline{\rho}\widetilde{u}_i)}{\partial x_i} = 0, \tag{2.1}$$

$$\frac{\partial (\overline{\rho}\widetilde{u}_j)}{\partial t} + \frac{\partial (\overline{\rho}\widetilde{u}_i\widetilde{u}_j)}{\partial x_i} = -\frac{\partial \overline{p}}{\partial x_j} + \frac{\partial}{\partial x_i}\left[2\widetilde{\mu}\left(\widetilde{S}_{ij} - \frac{1}{3}\delta_{ij}\widetilde{S}_{kk}\right)\right] + \frac{\partial \overline{\tau}_{ij}^{\mathrm{sgs}}}{\partial x_i}, \tag{2.2}$$

$$\frac{\partial (\overline{\rho}\widetilde{h})}{\partial t} + \frac{\partial (\overline{\rho}\widetilde{u}_i\widetilde{h})}{\partial x_i} = \frac{\partial}{\partial x_i}\left(\overline{\rho}\widetilde{D}_{\mathrm{h}}\frac{\partial \widetilde{h}}{\partial x_i}\right) + \frac{\partial J_{\mathrm{h}}^{\mathrm{sgs}}}{\partial x_i} + Q_{\mathrm{rad}}, \tag{2.3}$$

$$\frac{\partial (\overline{\rho}\widetilde{Z})}{\partial t} + \frac{\partial (\overline{\rho}\widetilde{u}_i\widetilde{Z})}{\partial x_i} = \frac{\partial}{\partial x_i}\left(\overline{\rho}\widetilde{D}_{\mathrm{Z}}\frac{\partial \widetilde{Z}}{\partial x_i}\right) + \frac{\partial J_{\mathrm{Z}}^{sgs}}{\partial x_i}, \tag{2.4}$$

$$\frac{\partial (\overline{\rho}\widetilde{C})}{\partial t} + \frac{\partial (\overline{\rho}\widetilde{u}_i\widetilde{C})}{\partial x_i} = \frac{\partial}{\partial x_i}\left(\overline{\rho}\widetilde{D}_{\mathrm{C}}\frac{\partial \widetilde{C}}{\partial x_i}\right) + \frac{\partial J_{\mathrm{C}}^{\mathrm{sgs}}}{\partial x_i} + \widetilde{\dot{\omega}}_{\mathrm{C}}, \tag{2.5}$$

$$\frac{\partial (\overline{\rho}\widetilde{Y}_{\mathrm{Pi}})}{\partial t} + \frac{\partial (\overline{\rho}\widetilde{u}_i\widetilde{Y}_{\mathrm{Pi}})}{\partial x_i} = \frac{\partial}{\partial x_i}\left(\overline{\rho}\widetilde{D}_{\mathrm{Y_{Pi}}}\frac{\partial \widetilde{Y}_{\mathrm{Pi}}}{\partial x_i}\right) + \frac{\partial J_{\mathrm{Y_{Pi}}}^{\mathrm{sgs}}}{\partial x_i} + \widetilde{\dot{\omega}}_{\mathrm{Y_{Pi}}}. \tag{2.6}$$

In this work, the Favre-filtered variable is defined as $\widetilde{f} = \overline{\rho f}/\overline{\rho}$ with the overbar denoting spatial filtering. $\overline{p}$ is the static pressure, $\widetilde{\mu}$ is the molecular viscosity, δ_{ij} is the Kronecker symbol, and $\widetilde{h}$ is the specific total enthalpy. Q_{rad} is the source term of the radiative heat transfer and is solved by using the discrete ordinate method [57, 58]. C is the progress variable defined by the summation of CO_2, CO, H_2, and H_2O mass fraction as mentioned in chapter 1, and $\widetilde{\dot{\omega}}_{\mathrm{C}}$ is the corresponding source term. D_{h}, D_{Z}, D_{C}, and $D_{\mathrm{Y_{Pi}}}$ are diffusivity coefficients for total enthalpy, mixture fraction, progress variable and the PAH species, which are derived based on the unity Lewis number assumption. It should be mentioned that the calculations and the discussions are all based on the unity Lewis number assumption in this work. $\widetilde{Z}$ is the mixture fraction for the fuel stream. S_{ij} is the rate-of-strain tensor which is given by

$$S_{ij} = \frac{1}{2}\left(\frac{\partial u_i}{\partial x_j} + \frac{\partial u_j}{\partial x_i}\right). \tag{2.7}$$

The stress tensor $\overline{\tau}_{ij}^{\mathrm{sgs}}$=$\overline{\rho}\widetilde{u_i u_j} - \overline{\rho}\widetilde{u}_i\widetilde{u}_j$ is modeled by a Smagorinsky model and a dynamic procedure [59]. J_{ϕ}^{sgs} ($\phi = h, Z_k, C$) is the residual subgrid scalar flux that is closed by a gradient transport assumption [60, 61] given by

$$J_{\phi}^{\mathrm{sgs}} = -\frac{\mu_{\mathrm{t}}}{Sc_{\mathrm{t}}}\frac{\partial \widetilde{\phi}}{\partial x_i}, \tag{2.8}$$

Table 2.1 Boundary conditions for LES coupled with the extended FPV.

	RUN 1	RUN 2
Mean velocity,m/s		
Oxygen inlet	1.1386	1.8029
HCOG inlet	1.4843	2.7706
Temperture, K		
Oxygen inlet	300	300
HCOG inlet	677	713
Pressure, kPa	100	100

where Sc_t is 0.4 [62] and eddy viscosity $\mu_t = C_t\Delta^2|\widetilde{S}_{ij}|$. C_t is defined by a dynamic procedure [59]. The Y_{Pi} is the mass fraction for the PAH species, while the ω_{Pi} is the corresponding source terms. The reaction rates of PAHs are considered slower than that of light species owing to the pyrolysis and break processes of the aromatic rings, and they will be overestimated in the SFM which is based on the fast chemistry assumption. Therefore, transport equations are solved rather than picking up and using the mass fractions directly from the flamelet library. The modeling of the reaction terms will be discussed in section 2.2.2.

In the present study, the convection term in the momentum conservation equation is discretized by the second-order central differencing formation, and the derivatives in the convection terms of scalar transport such as energy and chemical species equations are approximated by second-order upwind differencing scheme. The LES solver used in this study is FFR-Comb (NuFD/FrontFlowRed) which is extended by Kyushu University, Kyoto University, CRIEPI and NuFD [63, 19, 64, 65].

2.2.2 Extension of the FPV

In this chapter, two running cases, namely RUN 1 and RUN 2, are described. The crude gas temperature has been adjusted which results in the variations for composition and flux of the crude hot coke oven gas. Additionally, for the RUN 1 and RUN 2 case, the oxygen ratio has been varied, which is 0.34 and 0.17, respectively. The inflow boundary condtions such as velocity, temperature and pressure are listed in Table 2.1.

The inflow oxidizer and fuel compositions for both cases are initialized to generate the libraries, as specified in Table 2.2.

Table 2.2 Compounds of the inflow streams.

	RUN 1	RUN 2
Compounds in Oxygen inlet(mole fraction)		
O_2	1.0	1.0
Compounds in HCOG inlet(mole fraction)		
H_2	0.339032	0.362811
CH_4	0.201790	0.202500
C_2H_4	0.003031	0.004992
C_2H_6	0.000676	0.000809
CO	0.036253	0.043237
CO_2	0.011748	0.016295
N_2	0.031452	0.008231
H_2O	0.353025	0.337632
benzene	0.007371	0.008055
toluene	0.000139	0.000172
styrene	0.000486	0.000480
phenol	0.001064	0.001049
indene	0.001398	0.001379
naphthalene	0.007771	0.007663
2-methylnaphthalene	0.000680	0.000670
1-methylnaphthalene	0.000303	0.000299
acenaphthylene	0.000535	0.000528
acenaphthene	0.000109	0.000108
fluorene	0.000336	0.000332
phenanthrene	0.001091	0.001076
anthracene	0.000274	0.000271
cyclopenta[def]phenanthrene	0.000043	0.000042
2-phenylnaphthalene	0.000020	0.000020
fluoranthene	0.000440	0.000434
acephnanthrylene	0.000017	0.000017
aceanthrylene	0.000014	0.000014
pyrene	0.000302	0.000298
benzo[a]fluorene	0.000024	0.000024
cyclopenta[cd]pyrene	0.000008	0.000008
benz[a]anthracene	0.000120	0.000118
chrysene+triphenylene	0.000127	0.000126
benzo[b]fluoranthene	0.000097	0.000096
benzo[e]pyrene	0.000074	0.000073
benzo[a]pyrene	0.000078	0.000077
perylene	0.000021	0.000020
benzo[ghi]perylene	0.000032	0.000031
anthanthrene	0.000013	0.000012
coronene	0.000004	0.000004

Based on the boundary conditions, flamelet library can be generated by solving the flamelet equations listed in chapter 1. Chemical variables which are function of the first two moments of mixture fraction Z and the progress variable C can be readily obtained from the flamelet libraries. The computational expense is modest by courtesy of running computation prior to the simulation. Flamelet equations are solved by using the FLAMEMASTER code [66]. And a detailed chemistry mechanism including 257 species along with 2216 reactions is used [54, 67]. In order to calculate the mean value for the reactive scalars, a β-pdf is employed when the libraries are built. The extended FPV chemistry libraries are then parameterized by $\widetilde{Z}$, $\widetilde{Z''^2}$ and $\widetilde{C}$, and discretized by $101 \times 51 \times 101$ in the direction of $\widetilde{Z} \times \widetilde{Z''^2} \times \widetilde{C}$.

In the reforming process, 34 PAH species in Table 2.3 from C9 to C30 are considered to be the tarry composition in this study. It is considered that the reaction rates for these large PAH molecules in HCOG reforming process are slower than those of major species and thus have a relatively larger time scale in term of the chemical reactions. It is necessary to model the reaction terms in the mass fraction transport equations for these PAH species because the SFM is based on the fast chemistry assumption and will result in apparent discrepancies for PAH species. The concentration of the PAH species is evaluated by using the similar method as Ihme and Pitsch did [68, 19]. Similar to their approach, forward and backward PAH species reaction rates are separately modeled by the reaction rates taken from the flamelet library as:

$$\widetilde{\dot{\omega}_{P_i}} = \widetilde{\dot{\omega}_{P_i}^{+}} + \widetilde{Y_{P_i}} \frac{\widetilde{\dot{\omega}_{P_i}^{-}}}{\widetilde{Y_{P_i}^{flm}}}, \tag{2.9}$$

where the superscript flm denotes the values taken from the flamelet library, while the subscript P_i is the PAH species i. So $\widetilde{Y_{P_i}^{flm}}$ is the mass fraction of the PAH species i in flamelet library. $\widetilde{\dot{\omega}_{P_i}^{+}}$ and $\widetilde{\dot{\omega}_{P_i}^{-}}$ denote forward and backward reaction rate of PAH species i,respectively. A specific expression will be provided in the following. A one-step reaction of the PAH species i is given:

$$\mathrm{P}_i + \mathrm{B} \underset{k_b}{\overset{k_f}{\rightleftharpoons}} \mathrm{C} + \mathrm{D}, \tag{2.10}$$

here k_f and k_b denote the rate coefficient of the forward and backward reactions, respectively. For this reaction, the chemical reaction rate of the PAH species i can be put as:

$$\dot{\omega}_{P_i} = \dot{\omega}_{P_i}^{+} + \dot{\omega}_{P_i}^{-}, \tag{2.11}$$

Table 2.3 34 tarry speices in the HCOG reforming process.

Molecular Formula	Chemical Name
C_9H_8	Indene
$C_{10}H_8$	Naphthalene
$C_{12}H_8$	Acenaphthylene
$C_{13}H_{10}$	Fluorene
$C_{14}H_{10}$	Phenanthrene
$C_{14}H_{10}$	Anthracene
$C_{16}H_{10}$	Fluoranthene
$C_{16}H_{10}$	Acephenanthlyrene
$C_{16}H_{10}$	Aceanthrylene
$C_{16}H_{10}$	Pyrene
$C_{18}H_{10}$	Cyclopenta[cd]pyrene
$C_{18}H_{10}$	Cyclopenta[cd]fluoranthene
$C_{18}H_{10}$	Benzo[ghi]fluoranthene
$C_{18}H_{12}$	Tetraphene
$C_{18}H_{12}$	Naphthacene
$C_{18}H_{12}$	Chrysene
$C_{20}H_{10}$	Cyclopenta[cd]benzo[ghi]fluoranthene
$C_{20}H_{10}$	Corannulene
$C_{20}H_{10}$	Dicyclopentapyrene-cdfg
$C_{20}H_{12}$	Benzo[a]pyrene
$C_{20}H_{12}$	Benzo[e]pyrene
$C_{20}H_{12}$	Perylene
$C_{20}H_{12}$	Benzo[b]fluoranthene
$C_{20}H_{12}$	Benzo[k]fluoranthene
$C_{22}H_{10}$	Cyclopenta[cd]corannulene
$C_{22}H_{12}$	Anthanthracene
$C_{22}H_{12}$	Benzo[ghi]perylene
$C_{22}H_{12}$	Indeno[1,2,3-cd]pyrene
$C_{24}H_{10}$	Dicyclopenta[cd,fg]corannulene
$C_{24}H_{12}$	Coronene
$C_{24}H_{12}$	Cyclopentabenzo[ghi]perylene
$C_{26}H_{10}$	Tricyclopenta[bc,ef,hi]corannulene
$C_{28}H_{10}$	Tetracyclopenta[bc,ef,hi.kl]corrannulene
$C_{30}H_{10}$	Half-buckminsterfullerene

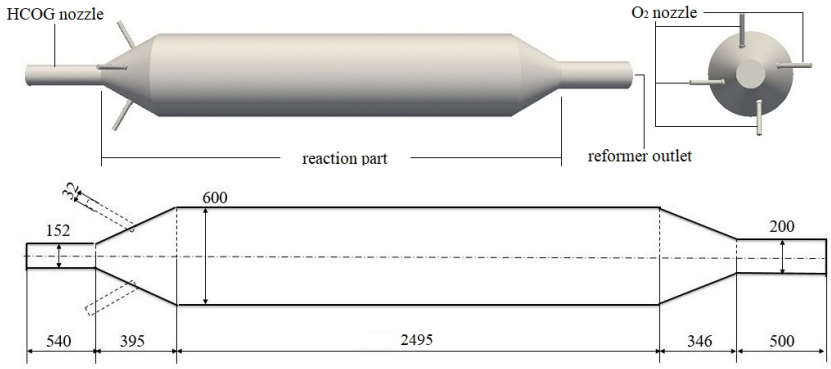

Fig. 2.1 Geometry of HCOG reforming reactor (unit: mm).

in which the consumption rate and production rate can be written as:

$$\dot{\omega}_{P_i}^{+} = -Y_{P_i}^{flm} k_b^{flm} \left(\frac{\rho^{flm} Y_B^{flm}}{M_B}\right), \tag{2.12}$$

$$\dot{\omega}_{P_i}^{-} = \frac{M_{P_i}}{\rho^{flm}} k_f^{flm} \left(\frac{\rho^{flm} Y_C^{flm}}{M_C}\right)\left(\frac{\rho^{flm} Y_D^{flm}}{M_D}\right), \tag{2.13}$$

where M is the molecular weight.

2.2.3 Computational details

The computational domain for the HCOG reformer is designed to match the experiments of Norinaga et al. [54]. Figure 2.1 illustrates the computational domain considered in this study. Unstructured grids are employed, and the total number of the cells is about 10 million. The reactor consists of one fuel nozzle, four oxygen nozzles, one outflow nozzle, and a reaction part. Nozzles are installed on the contracting part and expanding part of the reaction part. The inner diameter of the reaction part cylinder is 0.6 m, while for the fuel nozzle, the oxygen nozzle, and the outflow nozzle, it is 0.152 m, 0.032 m, and 0.2 m, respectively. The total length of the reactor is 4.28 m. The position of the four oxygen nozzles was optimized and therefore making sure the mixing of fuel and oxygen can be completed as quickly as possible.

In order to force turbulent fluctuation and to promote mixing between the fuel and oxygen, Danaila and Boersma's approach [69] that has been successfully employed in the existing works [62] is adopted to add the fluctuation to the measured velocity. Physical parameters are selected according to the geometry of the reactor in the

current case. In cylindrical coordinates, the velocity is set as follow:

$$\frac{V_{Z0}(r_c)}{V_0} = 0.5\left\{1 + tanh[0.25\frac{D}{\vartheta}(\frac{D}{4r_c} - \frac{r_c}{D})]\right\} \tag{2.14}$$

$$V_Z(r_c,t) = V_{Z0}(r_c)[1 + A_a sin(2\pi\frac{StaV_0}{D}t)] \tag{2.15}$$

where V_0 is the centerline velocity, r_c is the distance between the position on the inlet to the inlet area center, ϑ is the initial momentum thickness. D is the diameter of the inlet and D/ϑ is set to be 60, Sta is 0.55, and A_a is constant 0.15. The inflow centerline velocity for both fuel and oxygen can be found in Table 2.2.

For the reactor, although there is a thermal insulation layer outside the reformer, it cannot completely prevent heat releasing to the surrounding. It is necessary to find out the heat transfer coefficient in order to get a more precise result regarding the temperature distribution. In the experiments, the estimated heat loss for the reformer reaction part is 44637 kJ/h, and the temperature along the center line inside the cylinder part is averaged to be 1623 K while the surrounding temperature is considered as 293 K. The overall heat transfer coefficient for the reaction part is then estimated as 1.9823 W/ (m^2·K). As for other parts, since the thermal insulation layer is thicker than that in reaction part, the adiabatic condition is used.

For each case, 1024 cores of SGI ICE-X have been used, and the calculation has been running for about 66 hours of the wall-clock time. 300,000 steps has been computed, with 0.0001 seconds for each time step. Time-averaged values of the parameters are collected from the $250,001^{st}$ step to the last.

2.3 Results and discussion

2.3.1 Temperature distribution

The instantaneous temperature distributions for RUN 1 and RUN 2 have been shown in Figure 2.2. The red regions near the oxygen nozzle exit reflect the combustion position. Even the reacting flow is fully developed, according to the instantaneous contour, the temperature does not distribute evenly, and the turbulent flow coupled with chemical reactions might be responsible for this fluctuation.

In order to compare the simulated temperature with experimental data, the time-averaged temperature is employed as shown in Figure 2.3.

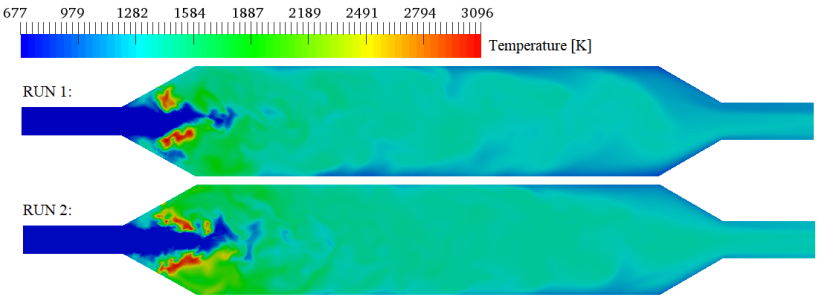

Fig. 2.2 Instantaneous temperature distribution inside the reformer for RUN 1 and RUN 2.

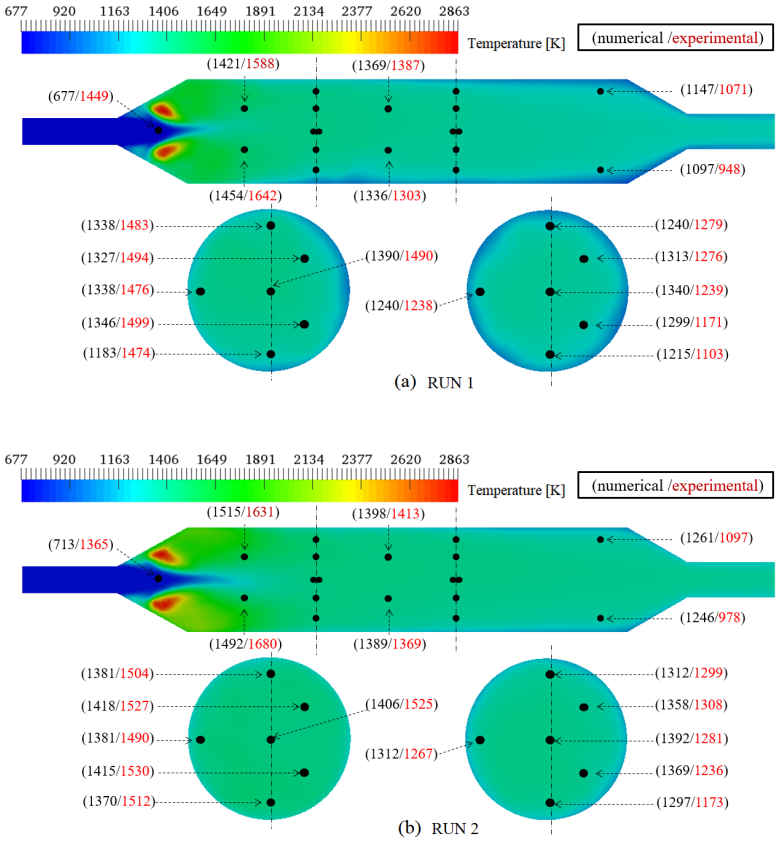

Fig. 2.3 Simulated time-averaged temperature distribution inside the HCOG reformer and its comparison with experimental results in corresponding measured points for (a) RUN 1 and (b) RUN 2.

For both cases, the predicted temperature is in good agreement with the measured data, especially in the middle and downstream of the reformer, whereas the temperature is underestimated in the upstream. Concerning the temperature measurement in the upstream, the radiation plays an important role and cannot be overlooked. As for the first measured point which nearby the reactor inlet, the reason for the temperature difference between the experiment and simulation has already been discussed by Li et al. [56]. Regarding the discrepancy for other points in the upstream, the effect of the carbon deposit which makes the measured value larger than the real one should be considered. In addition, in the present study only one overall heat transfer coefficient has been used, while this coefficient is an averaged estimated value and is not specific enough for both the whole reformer reaction part and the two experimental running cases. Furthermore, considering the heat loss of the reaction, a non-adiabatic flamelet model [25, 26, 63, 27] would be more desirable, however, there is an additional dimension in the flamelet library for the non-adiabatic flamelet model, it would make the library even larger if the we added an additional dimension to consider the three-feed non-premixed system in the next stage. According to the comparisons, even the deviations exist owing to experiment and the model themselves, the results are acceptable.

2.3.2 Reformed HCOG composition comparison

For the predicted gas concentration in the reformer outlet for both the RUN 1 and RUN 2, comparisons have been made with the experimental results, as it is shown in Figure 2.4. The steam and tarry species have been removed and only dry gas is considered in the comparisons. In both cases, the simulated results for H_2 and CO agree well with the experimental data. The product gas composition is altered due to the boundary condition varied from the RUN 1 to the RUN 2. According to the experimental measurements, H_2, CO increased from RUN 1 to RUN 2. And the increment trend from RUN 1 to RUN 2 can be captured well by simulation.

Generally, through the LES coupled with the extende FPV, it is able to predict the gas products composition well, in addition, it can capture the apparent variation trend of major species such as H_2 and CO for reformed dry gas satisfactorily.

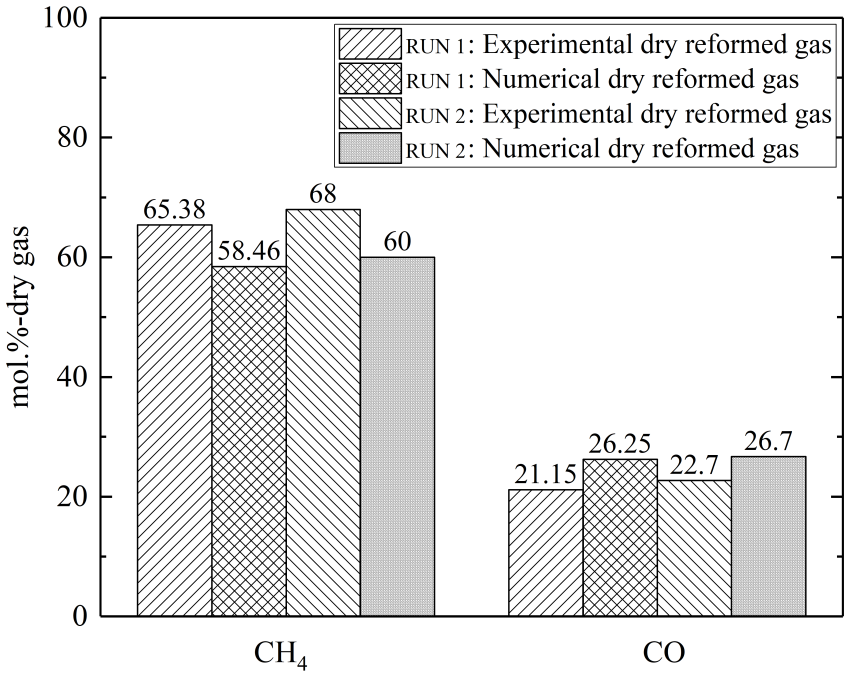

Fig. 2.4 Comparison of major species mole fractions at the exit of the HCOG reformer between numerical study and experimental measurement for RUN 1 and RUN 2.

2.4 Summary

By means of the LES coupled with the extende FPV, predictions of the HCOG partial oxidation reforming processes are presented. The approach is capable of capturing the temperature distribution well, although the temperature discrepancy between the numerical simulation and the experiment exists. This deviation may be considered partially due to the radiation effect and the carbon deposit influence, what is more, the unified estimated overall heat transfer coefficient used in the current study has its limitation. The SFM exluding the heat loss may be another reason, and a non-adibatic flamelet model is under the way to improve the results in terms of the HCOG reforming. As for the concentration of H_2 and CO, good predictions can be obtained through this approach. And the apparent variation trend can be captured. Therefore, the FPV can be used as a basis to extend higher-dimensional flamelet model for the three-feed system. In additiona, since the simulation results agree with the experimental data well, the model of the PAH source terms is validated, and for the combustion of raw syngas that contains coal tar the extended FPV coupled with this model would be a good option.

Chapter 3

Quasi-Two-Dimensional Flamelet Model for DNS

3.1 Background

Oki et al. proposed a new concept [3, 2, 4], namely oxy-fuel IGCC, in which the IGCC system is coupled with CCS. In addition to treating CO_2, this concept is expected to simplify the IGCC system and achieve high thermal efficiency as well. In the oxy-fuel IGCC system, part of the recirculated CO_2 is injected into the gas turbine combustor along with the syngas and pure oxygen from an air separation unit; thus, the combustor forms a three-feed non-premixed combustion system. For gaining deeper insight into this three-stream combustion system, in addition to experimentation, numerical simulation is a powerful tool. The flamelet model has many merits and it is worth employing it with regard to the three-feed system.

The conventional flamelet model is established based on a two-feed counterflow system, and variables are solved in a one-dimensional mixture fraction space. For a three-feed combustion system, on the other hand, a single mixture fraction is insufficient for describing the mixing process for the three streams. In general, a flow system with n ports requires n mixture fractions to form a complete basis, and as the summation of all the mixture fraction is unity, a $(n-1)$-dimensional mixture fraction space is sufficient. Therefore, for the three-feed combustion system, one additional mixture fraction is required to form the two-dimensional flamelet space on top of the standard fuel mixture fraction. In this study, three types of Q2DF models will be derived from a simplification of two-dimensional flamelet, and will be validated by

means of a two-dimensional DNS, in which a three-feed non-premixed combustion system is established and a Arrhenius formation case is used to be a reference.

3.2 Methodology

3.2.1 Governing equations

In this study, three types of Q2DF model are examined by means of DNS. It should be noted that in this study DNS denotes a numerical simulation that eliminates the effects of a turbulence model. In addition, DNS with the ARF is performed as a reference case for comparison with Q2DF models. The basic governing equations for the ARF are presented as Eqs.(3.1)∼(3.4) for the conservation of mass, momentum, energy, and chemical species mass fractions, respectively:

$$\frac{\partial \rho}{\partial t} + \frac{\partial \rho u_i}{\partial x_i} = 0, \tag{3.1}$$

$$\frac{\partial \rho u_i}{\partial t} + \frac{\partial \rho u_i u_j}{\partial x_j} = -\frac{\partial p}{\partial x_i} + \frac{\partial}{\partial x_j}\tau_{ij}, \tag{3.2}$$

$$\frac{\partial \rho h}{\partial t} + \frac{\partial \rho u_i h}{\partial x_i} = \frac{\partial p}{\partial t} + u_i \frac{\partial p}{\partial x_i} + \frac{\partial}{\partial x_i}\left(\rho D_{\mathrm{h}} \frac{\partial h}{\partial x_i}\right) + \tau_{ij}\frac{\partial u_i}{\partial x_i}, \tag{3.3}$$

$$\frac{\partial \rho Y_k}{\partial t} + \frac{\partial \rho u_i Y_k}{\partial x_i} = \frac{\partial}{\partial x_i}\left(\rho D_{\mathrm{Y}_k} \frac{\partial Y_k}{\partial x_i}\right) + \rho \dot{\omega}_{\mathrm{Y}_k}. \tag{3.4}$$

The equation of state for an ideal gas is also solved. To enable comparisons with Q2DF, additional transport equations for mixture fractions (Eqs.(3.5)∼(3.6)) are also considered:

$$\frac{\partial \rho Z_1}{\partial t} + \frac{\partial \rho u_i Z_1}{\partial x_i} = \frac{\partial}{\partial x_i}\left(\rho D_{\mathrm{Z}_1} \frac{\partial Z_1}{\partial x_i}\right), \tag{3.5}$$

$$\frac{\partial \rho Z_2}{\partial t} + \frac{\partial \rho u_i Z_2}{\partial x_i} = \frac{\partial}{\partial x_i}\left(\rho D_{\mathrm{Z}_2} \frac{\partial Z_2}{\partial x_i}\right). \tag{3.6}$$

In the above equations, Z_1 is the mixture fraction for the fuel stream, and Z_2 is that for the oxygen stream. τ is the viscous stress tensor, expressed by:

$$\tau_{ij} = \mu\left(\frac{\partial u_i}{\partial x_j} + \frac{\partial u_j}{\partial x_i}\right) - \frac{2}{3}\mu\delta_{ij}\frac{\partial u_k}{\partial x_k}, \tag{3.7}$$

where δ_{ij} is the Kronecker delta function. Except for k in Eq.(3.4), subscripts i, j and k in the above equations denote the directions in the Einstein notation.

Discretization for the spatial derivatives of the momentum convection term is derived from a fourth-order central differencing scheme, whereas for the scalar transports, a Weighted Essentially Non-Oscillatory (WENO) scheme [70] is used. The spatial derivatives of the stress tensor are evaluated by using a fourth-order central differencing scheme, and the diffusive terms are approximated by the second-order central difference method. For the time advancement, the third-order explicit Runge-Kutta method was adopted.

3.2.2 Quasi-two-dimensional flamelet model

The two-dimensional unsteady flamelet equations of chemical species mass fractions and temperature [44] can be written as:

$$\rho\frac{\partial Y_k}{\partial t} = \frac{\rho}{2}\left(\chi_1\frac{\partial^2 Y_k}{\partial Z_1^2} + \chi_{13}\frac{\partial^2 Y_k}{\partial Z_1 \partial Z_3} + \chi_3\frac{\partial^2 Y_k}{\partial Z_3^2}\right) + \rho\dot{\omega}_{\mathrm{Y}_k}, \tag{3.8}$$

$$\begin{aligned}\rho\frac{\partial T}{\partial t} = \frac{\rho}{2}\left(\chi_1\frac{\partial^2 T}{\partial Z_1^2} + \chi_{13}\frac{\partial^2 T}{\partial Z_1 \partial Z_3} + \chi_3\frac{\partial^2 T}{\partial {Z_3}^2}\right) + \frac{1}{c_\mathrm{p}}\left(\rho\sum_{k=1}^{n_\mathrm{s}} h_k\dot{\omega}_{\mathrm{Y}_k} + \frac{\partial p}{\partial t}\right) \\ + \frac{\rho}{2c_\mathrm{p}}\frac{\partial T}{\partial Z_1}\left[\chi_1\frac{\partial c_\mathrm{p}}{\partial Z_1} + \chi_{13}\frac{\partial c_\mathrm{p}}{\partial Z_3} + \sum_{k=1}^{n_\mathrm{s}}\left(\chi_1\frac{\partial Y_k}{\partial Z_1} + \chi_{13}\frac{\partial Y_k}{\partial Z_3}\right)\right] \\ + \frac{\rho}{2c_\mathrm{p}}\frac{\partial T}{\partial Z_3}\left[\chi_3\frac{\partial c_\mathrm{p}}{\partial Z_3} + \chi_{13}\frac{\partial c_\mathrm{p}}{\partial Z_1} + \sum_{k=1}^{n_\mathrm{s}}\left(\chi_3\frac{\partial Y_k}{\partial Z_3} + \chi_{13}\frac{\partial Y_k}{\partial Z_1}\right)\right].\end{aligned} \tag{3.9}$$

Here, T is the temperature and n_s is the species number in the mixture. χ_1, χ_3 are the scalar dissipation rates for Z_1, Z_3, respectively, and χ_{13} is the cross-scalar dissipation rate; these can be described as:

$$\chi_1 = 2D\left(\frac{\partial Z_1}{\partial x_i}\right)^2, \chi_3 = 2D\left(\frac{\partial Z_3}{\partial x_i}\right)^2, \chi_{13} = 2D\left(\frac{\partial Z_1}{\partial x_i}\right)\left(\frac{\partial Z_3}{\partial x_i}\right). \tag{3.10}$$

It has been confirmed that the scalar dissipation rate tends to be a very small value downstream from the moderate and intense and low oxygen dilution combustor [71], implying the gradient of fuel mixture fraction is very small. If the scalar dissipation rate for Z_2 or Z_3 were also such a tiny value that it can be ignored, then the two-dimensional flamelet equations could be reduced to a series of one-dimensional formations. There are two apparent options for reducing the two-dimensional flamelet model in the three-feed counterflow system: to set the value of Z_3 to be zero or to set the gradient of Z_3 to be zero.

If the Z_3 is set to zero, and the diluent stream is categorized as part of the oxidizer stream while the fuel stream is kept unchanged, then the three-feed counterflow system is transferred into the classical two-feed counterflow system. Z_3 here disappears, but it is still influencing the flamelet implicitly through the ratio of the diluent in the stream it belongs to; this ratio is termed the diluent fraction in the following discussion. With various diluent fractions, there is a one-dimensional flamelet family; this case is denoted Q2DF1.

If the two-dimensional flamelet equations in Eqs. (3.8) and (3.9) are written in terms of Z_2 and Z_3, then in a similar way, Z_3 can be put into the fuel stream with various proportions, and another group of flamelets can be generated. This case is referred to hereinafter as Q2DF2. W_1 and W_2 are defined to be the diluent fractions corresponding to these two cases and can be given as the following:

$$W_1 = \frac{\dot{m}_{3\mathrm{o}}}{\dot{m}_2 + \dot{m}_{3\mathrm{o}}} = \frac{\dot{m}_{3\mathrm{o}}}{\dot{m}_2 + \dot{m}_{3\mathrm{o}}} \times \frac{\dot{m}_1 + \dot{m}_2 + \dot{m}_{3\mathrm{o}}}{\dot{m}_1 + \dot{m}_2 + \dot{m}_{3\mathrm{o}}} = \frac{Z_3}{Z_2 + Z_3}, \tag{3.11}$$

$$W_2 = \frac{\dot{m}_{3\mathrm{f}}}{\dot{m}_1 + \dot{m}_{3\mathrm{f}}} = \frac{\dot{m}_{3\mathrm{f}}}{\dot{m}_1 + \dot{m}_{3\mathrm{f}}} \times \frac{\dot{m}_1 + \dot{m}_2 + \dot{m}_{3\mathrm{f}}}{\dot{m}_1 + \dot{m}_2 + \dot{m}_{3\mathrm{f}}} = \frac{Z_3}{Z_1 + Z_3}, \tag{3.12}$$

where $\dot{m}_1$ is the fuel stream mass, $\dot{m}_2$ is the oxidizer stream mass, $\dot{m}_{3\mathrm{o}}$ is the diluent stream mass put in on the oxidizer side, and $\dot{m}_{3\mathrm{f}}$ is that put in on the fuel side.

For the Q2DF1 case, in the two-feed counterflow system, Z and $1-Z$ can be defined as in Eqs.(3.13) and (3.14), respectively. Hereinafter, Z without a subscript is used to denote the conventional mixture fraction in the one-dimensional flamelet model.

$$Z = \frac{\dot{m}_1}{\dot{m}_1 + \dot{m}_2 + \dot{m}_{3\mathrm{o}}} = Z_1, \tag{3.13}$$

$$1 - Z = \frac{\dot{m}_2 + \dot{m}_{3\mathrm{o}}}{\dot{m}_1 + \dot{m}_2 + \dot{m}_{3\mathrm{o}}} = Z_2 + Z_3. \tag{3.14}$$

If the diluent stream is classified in the fuel stream as in the Q2DF2 case, then the standard mixture fraction Z and $1-Z$ in a one-dimensional flametlet model can be described as given by Eqs.(3.15) and (3.16), respectively:

$$Z = \frac{\dot{m}_1 + \dot{m}_{3\mathrm{f}}}{\dot{m}_1 + \dot{m}_2 + \dot{m}_{3\mathrm{f}}} = Z_1 + Z_3, \tag{3.15}$$

$$1 - Z = \frac{\dot{m}_2}{\dot{m}_1 + \dot{m}_2 + \dot{m}_{3\mathrm{f}}} = Z_2. \tag{3.16}$$

As mentioned earlier, for Eqs. (3.8) and (3.9), the two-dimensional flamelet equations can also be reduced to one-dimensional form by assuming a zero gradient for Z_3 in the three-feed counterflow system; this case is denoted Q2DF3 in this study. Here, the value of Z_3 is considered a constant in the counterflow field but not zero. With different Z_3 values in the range of zero to unity, there will be a group of one-dimensional flamelets. It is approximated by putting the diluent stream into both the fuel stream and the oxidizer stream with the same mass fraction. The diluent fraction W_3 can be defined as given by Eq. (3.17):

$$W_3 = \frac{\dot{m}_{3\mathrm{f}}}{\dot{m}_1 + \dot{m}_{3\mathrm{f}}} = \frac{\dot{m}_{3\mathrm{o}}}{\dot{m}_2 + \dot{m}_{3\mathrm{o}}} = \frac{\dot{m}_{3\mathrm{f}} + \dot{m}_{3\mathrm{o}}}{\dot{m}_1 + \dot{m}_2 + \dot{m}_{3\mathrm{f}} + \dot{m}_{3\mathrm{o}}} = Z_3. \tag{3.17}$$

It is evident that Z_3 affects the flamelet explicitly in this case. Note that the connection between $m_{3\mathrm{f}}$ and m_1 can be determined by Z_3 when Z_3 is neither unity nor zero:

$$\frac{\dot{m}_{3\mathrm{f}}}{\dot{m}_1} = \frac{Z_3}{1 - Z_3}. \tag{3.18}$$

Then, the standard mixture fraction Z in the one-dimensional flametlet model can be given as:

$$\begin{aligned} Z &= \frac{\dot{m}_1 + \dot{m}_{3\mathrm{f}}}{\dot{m}_1 + \dot{m}_2 + \dot{m}_{3\mathrm{f}} + \dot{m}_{3\mathrm{o}}} \\ &= \frac{\dot{m}_1}{\dot{m}_1 + \dot{m}_2 + \dot{m}_{3\mathrm{f}} + \dot{m}_{3\mathrm{o}}} \times (1 + \frac{Z_3}{1 - Z_3}) \\ &= Z_1 \times (1 + \frac{Z_3}{1 - Z_3}) = Z_1 \times \frac{1}{1 - Z_3} = \frac{Z_1}{1 - Z_3}, \end{aligned} \tag{3.19}$$

and in the same way, on the oxidizer side $1-Z$ can be derived as:

$$\begin{aligned} 1-Z &= \frac{\dot{m}_2+\dot{m}_{3\mathrm{o}}}{\dot{m}_1+\dot{m}_2+\dot{m}_{3\mathrm{f}}+\dot{m}_{3\mathrm{o}}} \\ &= \frac{\dot{m}_2}{\dot{m}_1+\dot{m}_2+\dot{m}_{3\mathrm{f}}+\dot{m}_{3\mathrm{o}}} \times (1+\frac{Z_3}{1-Z_3}) \\ &= Z_2 \times (1+\frac{Z_3}{1-Z_3}) = Z_2 \times \frac{1}{1-Z_3} = \frac{Z_2}{1-Z_3}. \end{aligned} \tag{3.20}$$

Given that there is only CO_2 in the whole counterflow field for a unity Z_3, whereas a zero Z_3 gives a non-diluent environment, these two cases should also be considered.

The extensions above are the conditional one-dimensional flamelet model based on the two-dimensional flamelet formulation; therefore, these models are referred to as quasi-two-dimensional flamelet (Q2DF) models in this study.

In these three Q2DF model cases, the mass fractions and the total enthalpy have already been tabulated prior to running the simulation, but Eqs. (3.1),(3.2),(3.5), and (3.6), as well as the progress variable transport equation, need to be solved. Progress variable C is one of the tracking parameters used for lookup in the flamelet library, and it is defined as the sum of the mass fractions of CO_2,H_2O,CO and H_2 in this work. The transport equation for C is given as Eq.(3.21):

$$\frac{\partial \rho C}{\partial t} + \frac{\partial \rho u_i C}{\partial x_i} = \frac{\partial}{\partial x_i}\left(\rho D \frac{\partial C}{\partial x_i}\right) + \rho \dot{\omega}_{\mathrm{c}}, \tag{3.21}$$

here $\dot{\omega}_{\mathrm{c}}$ is the source term, which is the sum of the source terms for the mass fractions of CO_2,H_2O,CO and H_2.

Besides Z and C, the additional tracking parameter W_1 or W_2 or W_3 is indispensable for lookups in the library. Together with W_1, W_2, and W_3, the flamelets file are generated by using FLAMEMASTER code [66] with a detailed chemical mechanism given by GRI-Mech version 3.0 [72], in which 53 species and 634 reactions have been taken into account. A summary for the libraries for the three Q2DF cases is given in Table 3.1 and variables are looked up by the quadruple-linear interpolation. It should be noted that these libraries can be directly used for LES, and in order to make them workable for DNS, the variances in the codes are set to be zero for this work. Figure 3.1 shows the temperature profiles of the flamelets for each case when the stoichiometric scalar dissipation rate is unity; the abscissa mixture fractions, however, differ for the three cases according to Eqs.(3.13), (3.15), and (3.19).

Table 3.1 Q2DF cases presented.

Cases	Method	Parameter & Resolution
Q2DF1	FPVA	$\widetilde{Z}_1 \times \widetilde{Z_1''} \times \widetilde{C} \times W_1$=81×41×61×21
Q2DF2	FPVA	$(\widetilde{Z}_1+\widetilde{Z}_3) \times \widetilde{Z_2''} \times \widetilde{C} \times W_2$=81×41×61×21
Q2DF3	FPVA	$Z_1/\widetilde{(1-Z_3)} \times [Z_1/\widetilde{(1-Z_3)}]'' \times \widetilde{C} \times W_3$=81×41×61×21

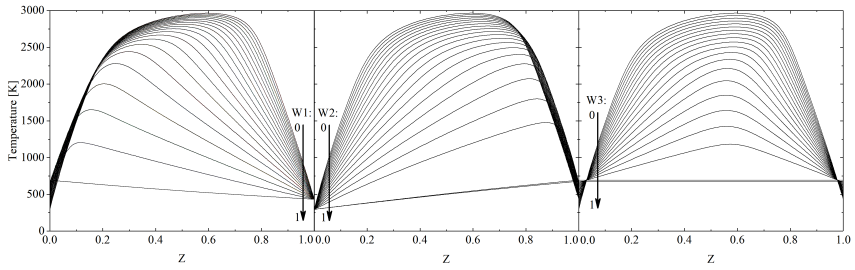

Fig. 3.1 Flamelet solutions for temperature as a function of mixture fraction Z and diluent fraction W evaluated at a constant stoichiometric scalar dissipation rate of $\chi_{Z_{st}}$=1s^{-1} for three quasi-two-dimensional flamelet (Q2DF) cases, (a) Q2DF1, (b) Q2DF2 and (c) Q2DF3.

3.2.3 Computational details

In this study, the three-feed non-premixed flame was investigated by two-dimensional DNS with a surrounding pressure of 1.0 atm. Diluent, oxygen, and fuel are injected into the computational domain simultaneously. The central inflow is the diluent stream, which is CO_2, and its neighbor inflows are fuel streams consisting of CO and H_2. The outer layers are oxygen injected at relatively low speed. Two layers of the stoichiometric mixture of fuel and oxygen are issued between the fuel and the oxygen streams to ignite and maintain the flame. These stoichiometric mixture hot co-flows are obtained from the flamelet library by tracking the stoichiometric mixture fraction Z_{st}, which is 0.56944; a progress variable C, 0.775; and a diluent fraction, zero. Parameters for the inflow streams are listed in Table 3.2. It should be mentioned here the temperature of the three streams are determined according to the experiment boundary condition which will be given in the next chapter. The jet Reynolds number is roughly 12500 based on half of the domain inlet length (0.025 m) and slip velocity between the fuel and diluent. The length is nondimensionalized by the fuel inlet width ($L = 2$ mm), and the dimensions of the computational domain are 100 in the x direction ($0 \leq x/L \leq 100$) and 25 in the y direction ($|y/L| \leq 12.5$). A schematic of the computational domain is given in Figure 3.2. The computational

Table 3.2 Flow parameters of the inflow streams.

Compounds in fuel stream(mass fraction)	
CO	0.9749
H_2	0.0251
Compounds in Oxidizer stream(mass fraction)	
O_2	1.0
Compounds in diluent stream(mass fraction)	
CO_2	1.0
Mean velocity,m/s	
Diluent inflow	40
Fuel inflow	20
Hot co-flow inflow	20
Oxydizer inflow	3
Temperture, K	
Fuel inflow	433.35
Oxidizer inflow	296.15
Diluent inflow	693.45

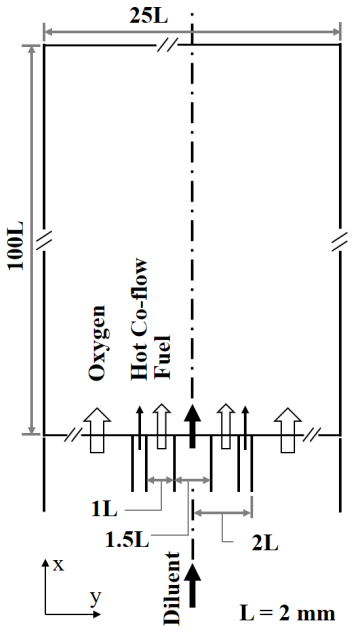

Fig. 3.2 Sketch of the computational domain.

domain is divided by 2000×500 nonuniform grid points (a total of 1.0 million cells) in the x and y directions. The finest mesh is arranged around the centerline ($|y/L| = 0$), which is 35 μm in the lateral direction, and the grid size grows gradually toward the lateral boundaries by a very small ratio. This resolution is considered to be fine enough to exhibit the flame behaviors given by the flamelet modeling [18, 23, 73, 74]. The number of grid points has been further determined from comparisons of a finer case (2500×700) and a coarser case (1000×250) for the Q2DF1 case.

For the boundary setting in the y direction, a nonslip adiabatic wall is applied. For the purpose of generating velocity perturbation, continuous sine functions [18, 23, 74] with a magnitude of 5% are employed for the central stream. The velocity components in the lateral direction for other inflows are imposed to be zero.

The simulations were performed by an in-house program referred to as FK^3 [75, 76, 24, 77], which employs a pressure-based semi-implicit solver for compressible flows [78]. The fractional-step method for the compressible flows is used as the computational algorithm [78, 20, 21].

All four cases were carried out by parallel computations on a Fujitsu PRIMERGY CX2550/CX2560 M4. For ARF case, the wall clock time was roughly 500 h with 2000 cores, whereas for each Q2DF case the wall clock time was about 68 h with 500 cores. Sixteen flow-through times were run first for each case to eliminate the effect of the initial flow field, ensuring that the flame was fully developed. Here, the flow-through time was calculated according to the definition given in the literature [77]. From that point, the statistics were collected for a period equivalent to another eight flow-through times, which is considered to be more than long enough to attain statistical stationarity.

3.3 Result and analysis

3.3.1 Overview of three-feed non-premixed flame

Figure 3.3 shows distributions of the instantaneous temperature (T), fuel mass fraction (Y_{fuel}), fuel mixture fraction (Z_1), CO_2 mass fraction ($Y_{\mathrm{CO_2}}$), and diluent mixture fraction (Z_3) for the ARF case. The fuel streams are ignited soon after they are injected, forming separated flames in the upper stream. The flame temperature achieves its peak in the upper stream owing to the presence of sufficient fuel and oxygen supply. Then, toward the middle of the stream, the flame temperature

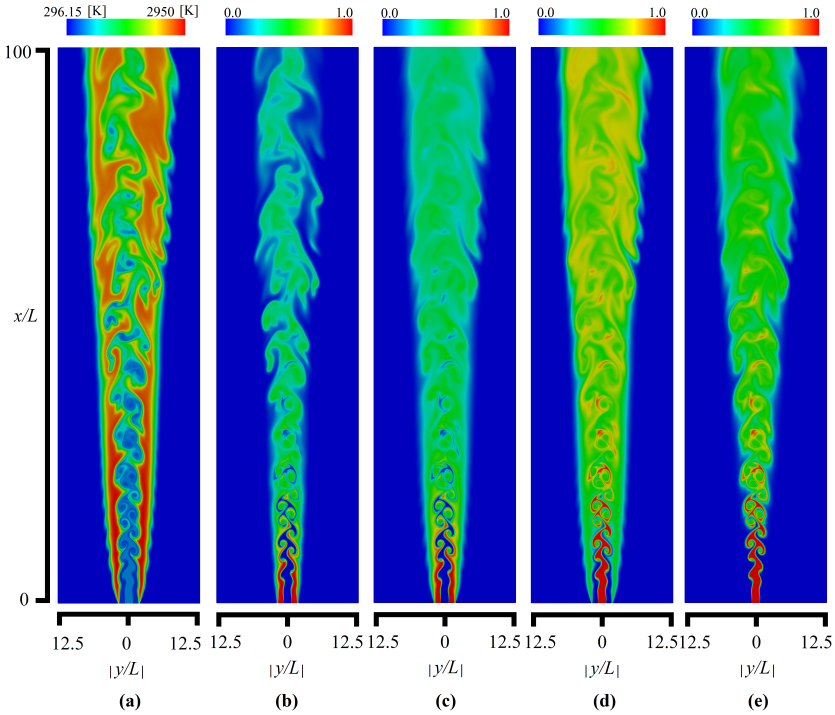

Fig. 3.3 Instantaneous distributions for (a) temperature, (b) fuel mass fraction, (c) fuel mixture fraction (Z_1), (d) CO_2 mass fraction, and (e) diluent mixture fraction (Z_3) in the Arrhenius formation (ARF) case.

decreases markedly, but from the midstream to the lower stream, the temperature reduction is not significant. From the upper stream, a portion of the burned gases is entrained into the central stream. It is found that the interaction between the diluent and fuel gases is promoted as the turbulence developed, and vortexes can be observed even near the inlet. As the turbulence evolves further, the initially separate flames touch each other and converge in the midstream, and larger vortexes are generated. The flame maintains a relatively high temperature between oxygen and the fuel stream because of the weak diluent convection. According to the fuel mass fraction, the fuel stream turbulence has developed mainly in the axial direction; in the lateral direction, its convection and diffusion are limited. The instantaneous fuel mixture fraction snapshot takes a shape similar to that of the temperature distribution. Given that the fuel mixture fraction also tracks the products that contain the elements from the fuel, the edge of the fuel mixture fraction can indicate the product concentrations. Thus, in the high-temperature flame area, the combustion is complete, whereas there is a fuel-rich area in the central stream, and a fuel-lean condition occurs on the oxygen-stream side. Fuel is consumed in the reaction process, whereas the fuel mixture fraction is a conserved scalar, and unlike these variables, CO_2 almost does not take part in the reaction, and the total amount vastly increases. The diluent mixture fraction is the CO_2 part injected, whereas the CO_2 mass fraction takes both injected and produced parts into account. It is found that sufficient mixing of the fuel stream and the diluent stream can be obtained, as well as that of the fuel mixture fraction and diluent mixture fraction. The mixing of the three mixture fractions is essential for this combustion system as temperature and the mass fractions of all the species in Q2DF cases are based on the lookup process. To enable further investigation, Figure 3.4 shows scatter plots of the three instantaneous mixture fractions for all four cases and provides a quantitative description of their mixing. It is found that considerably many dots are located in $0 < Z_1 + Z_3 < 1$ area (the mixing area), particularly when when $0.25 \leq Z_1 \leq 0.5$, indicating that a thorough blending of the three mixture fractions has been obtained. However, there are slight differences concerning the closed areas that are formed by gray borderlines and vertical axials as shown in Figure 3.4. The mixing is varied slightly from ARF to Q2DF cases when $Z_3 > 0.25$. However, overall, the mixing areas in the scatter plots for the three Q2DF cases are in very good agreement with that of ARF in terms of the mixing of the mixture fractions.

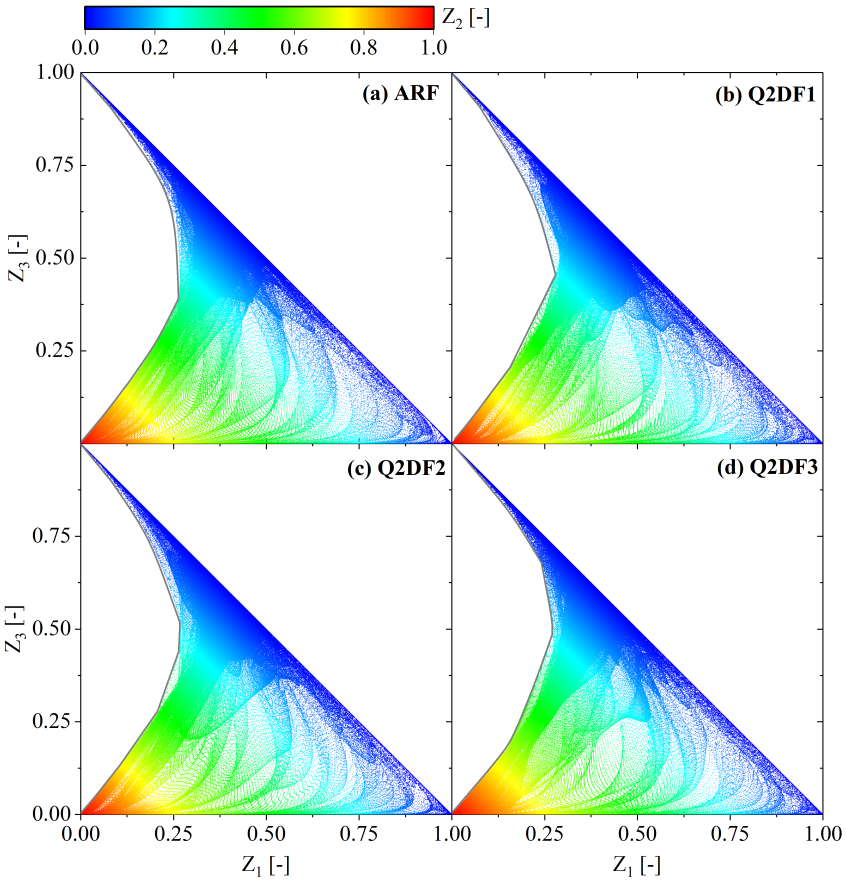

Fig. 3.4 Scatter plots of instantaneous diluent mixture fraction (Z_3) and fuel mixture fraction (Z_1), colored by oxygen mixture fraction (Z_2), for four cases: (a) ARF, (b) Q2DF1, (c) Q2DF2, and (d) Q2DF3.

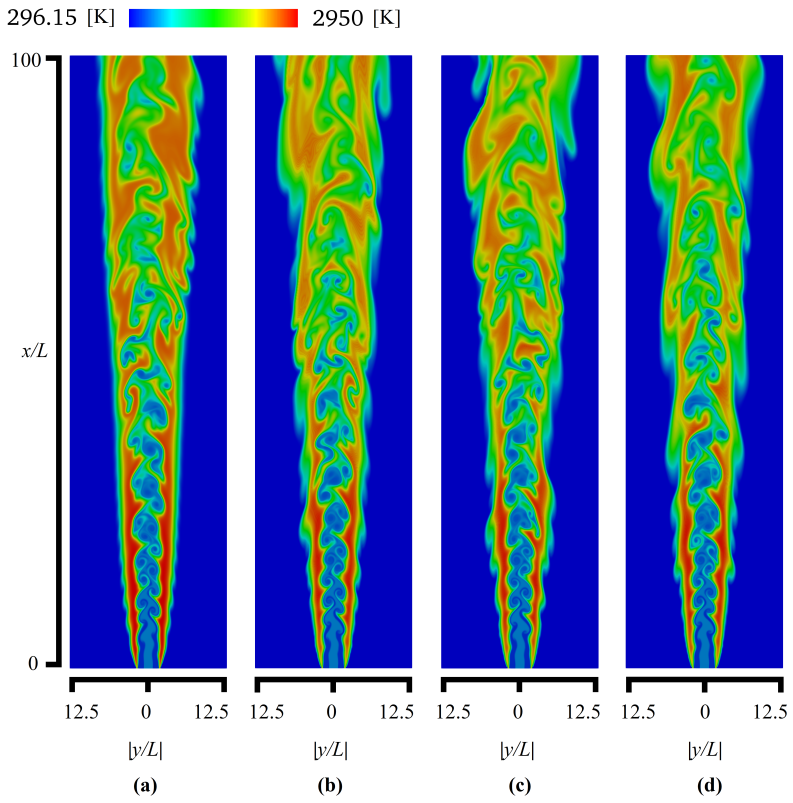

Fig. 3.5 Distributions of instantaneous temperature for four cases: (a) ARF, (b) Q2DF1, (c) Q2DF2, and (d) Q2DF3.

3.3.2 Comparison between ARF and Q2DF cases

Instantaneous Variables

An overview of the flame characteristics for the ARF case was given in section 3.3.1. Figure 3.5 here shows the instantaneous temperature snapshots for all four cases. In general, the features in the ARF case are captured by the three Q2DF cases. However, there are some differences that should not be overlooked. It is found that the flame edge in the ARF case is smoother than that in Q2DF cases, and there is an apparent wrinkling of the flame edge in Q2DF cases. Additionally, compared with the ARF case, there is more severe turbulence occurring in the lower stream, but there is no significant difference among the three Q2DF cases. To analyze the temperature distribution further, scatter plots have been used because scatter plots for species mass fraction and temperature can essentially represent the lookup results. Figure 3.6 shows the instantaneous temperature distribution in $Z_1 \times Z_2$ space, colored by Z_3. The high temperature appears around Z_{st} (0.56944) for the ARF case; as the

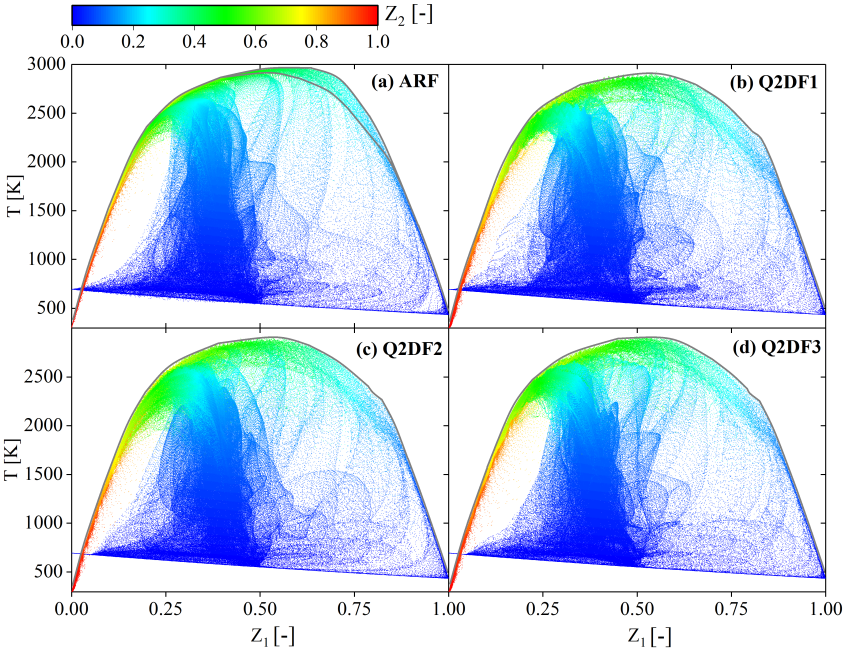

Fig. 3.6 Scatter plots of instantaneous temperature (T) and fuel mixture fraction (Z_1), colored by oxygen mixture fraction (Z_2), for four cases: (a) ARF, (b) Q2DF1, (c) Q2DF2, and (d) Q2DF3.

fuel mixture fraction gradually increases, it can still maintain high temperature as indicated by the gray borderline. However, from this perspective, the borderlines in the Q2DF cases differ from that in the ARF case. The closed borderline area in the ARF case has not been predicted in the Q2DF cases. According to the raw data extracted from the flamelet solutions (Figure 3.1), the closed borderline area in the ARF case is included in the libraries for the Q2DF cases, which means that the deviation is due to the difference in the distributions of the tracking parameters between the ARF case and the Q2DF cases. More diluent mixture fractions have become involved in the combustion area because of the more severe turbulence predicted in the Q2DF cases; thus, the diluent effect has been promoted, which results in a larger diluent fraction and a lower lookup temperature in the libraries. Although the deviation is inevitable, the scatter plots for the Q2DF cases generally represent the temperature shown in the ARF case. The area with a high density of dots is captured well by the Q2DF cases. It is observed that there are overlapping areas, and in these areas, the temperature is very sensitive to the oxygen mixture fraction, which may also explain why the flame temperature is not decreased (or not much decreased) from the midstream, as in the lower stream the oxygen mixture fraction has been largely entrained into the central stream.

In this three-feed non-premixed combustion system, CO_2 plays an essential role; therefore, its instantaneous behavior is worth investigating. Figure 3.7(a) shows the scatter plots of CO_2 mass fraction for all four cases. It is clear that CO_2 mass fraction is not unique in any sole mixture fraction space, and it can be described properly in the joint mixture fraction space. CO_2 mass fraction is zero when $Z_1 = 1$ or $Z_2 = 1$, and it is unity as $Z_1 = 0$ and $Z_2 = 0$. CO_2 mass fraction can be split into two parts as mentioned above. As fuel increases while the oxygen is consumed, the generated CO_2 increases first, and this part of CO_2 reduces when $Z_1 > Z_{st}$. From $Z_1 = 1, Z_2 = 0$, as Z_1 decreases, there are two directions for Z_2 development toward $Z_1 = 0$: One is that Z_2 increases until it is unity, which results in a zero CO_2 mass fraction; the other is that it maintains the same level, leading to a CO_2 mass fraction of unity. These two directions correspond to the fuel interactions with the diluent and oxygen, respectively. Moreover, the fuel interactions with the diluent and oxygen will definitely promote the mixing and coexistence of the three streams. Although there are some deviations that should be noted, as shown in the marked area (such as the range where $0.25 \leq Z_1 \leq 0.3$ is shown), in Z_1 space, the Q2DF cases obtained good agreement with respect to the ARF case, and the Q2DF cases can essentially capture the distribution of CO_2 in $Z_1 \times Z_2$ space.

The mass fraction of CO accounts for more than 97% in the fuel stream, and Figure 3.7(b) shows the distribution of the instantaneous CO mass fraction in $Z_1 \times Z_2$ space. Naturally, its concentration is low when Z_1 is small and increases as Z_1 tends to unity. In the oxygen stream and the diluent stream, CO mass fraction is low before the turbulence predominates, which is the reason the scatter plots split into two branches from $Z_1 = 0$. However, the interaction of fuel with the diluent side and the oxygen side in the Q2DF cases is more intense than that in the ARF case, as it is observed that there are more dots in the marked area in the Q2DF cases, and the marked area is smaller in the Q2DF cases as well. In spite of this, however, the Q2DF cases describe the behavior of CO accurately overall.

Figure 3.8(a) illustrates the distribution of the instantaneous oxygen mass fraction. As mentioned above, the three mixture fractions mixed very well, especially when $0.25 \leq Z_1 \leq 0.5$. However, Z_2 includes not only the oxygen in the domain but also that in the products. It is observed that the variation is the same for both Z_2 and oxygen mass fraction; this is because those areas with less oxygen distribution have a lower production. Even when the oxygen mass fraction is low, the interaction with both fuel and diluent is strong owing to the entrainment and reaction, corresponding to $0.2 \leq Z_2 \leq 0.3$. A slight difference exists between the Q2DF cases and the ARF

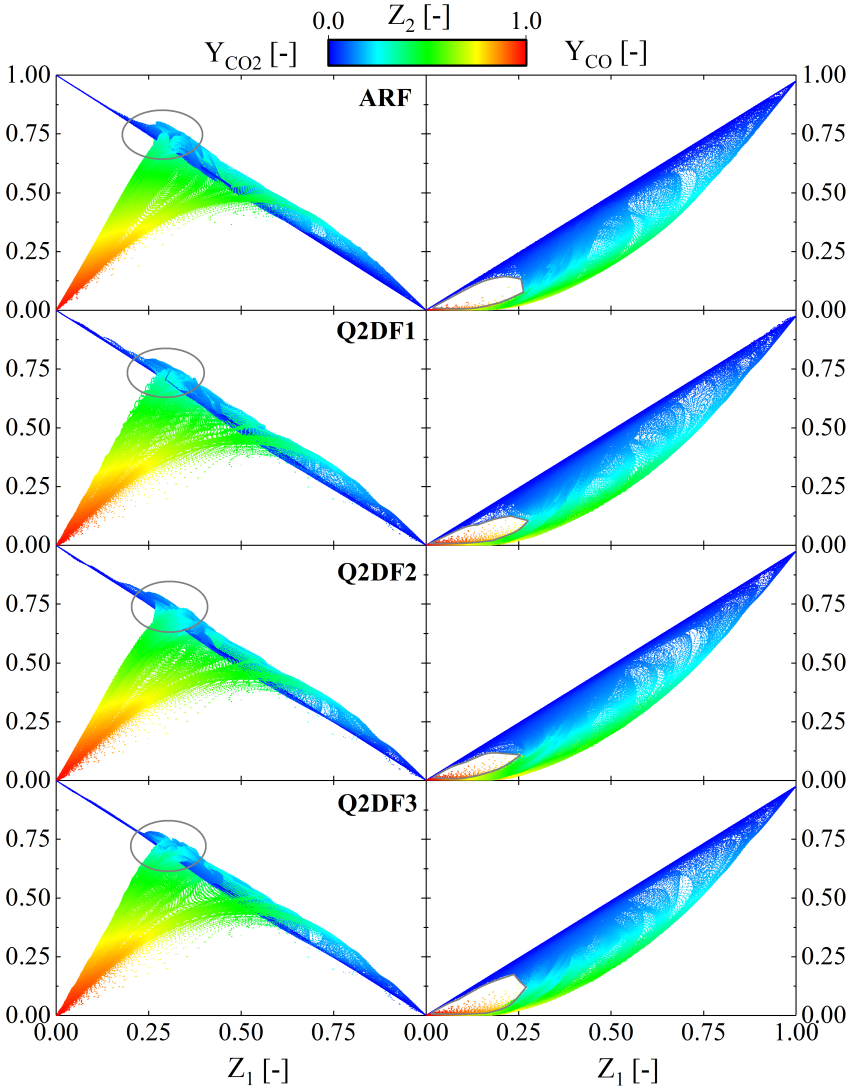

Fig. 3.7 Scatter plots of instantaneous CO_2 mass fraction (a) or CO mass fraction (b) and fuel mixture fraction (Z_1), colored by oxygen mixture fraction (Z_2), for four cases (top to bottom): ARF, Q2DF1, Q2DF2, and Q2DF3.

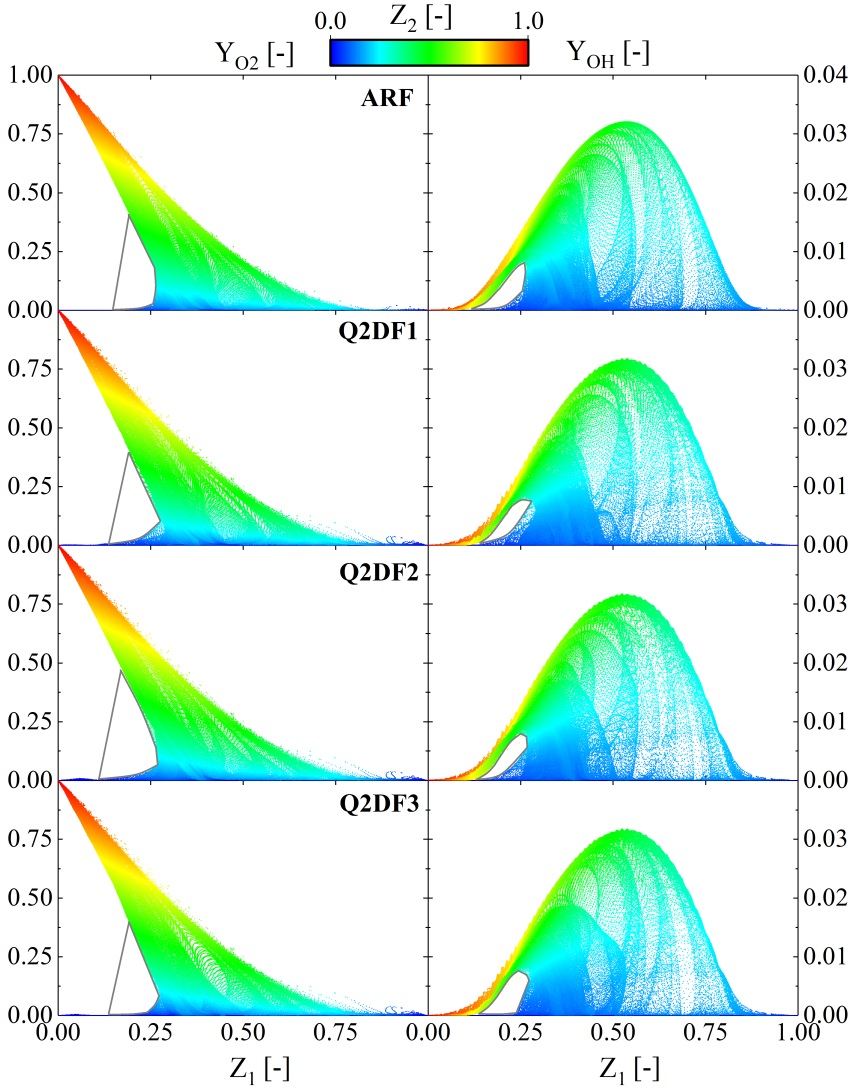

Fig. 3.8 Scatter plots of instantaneous O_2 mass fraction (a) or OH mass fraction (b) and fuel mixture fractions (Z_1), colored by oxygen mixture fraction (Z_2), for four cases (top to bottom): ARF, Q2DF1, Q2DF2, and Q2DF3.

case, as shown in the marked area. However, the main O_2 characteristics are captured very well.

OH is one of the typical intermediate species, and it is sensitive to the mixing and interaction of three feeds. Figure 3.8(b) shows its scatter plots; the Q2DF cases obtained good agreement with the ARF case. Local OH achieves its peak when diluent is almost absent and $Z_1 = Z_{st}$, which is consistent with temperature distribution. In the lower stream, OH is generated in high temperature area in general and can be considered a symbol species for the reaction rate. The scatter plots here for OH is not exactly the same as those given in Ref [45], in which an error rate of greater than 20% occurred. However, deviations exist in the marked area for the Q2DF cases, and the Q2DF cases predict a smaller marked area.

Time-averaged Variables

Figure 3.9∼3.11 present lateral profiles of time-averaged variable values for the four cases. These are taken from the axial locations $x/L = 20$, 40, 60, and 80.

Figure 3.9 shows the time-averaged results for temperature and Z_1. It is found that in the centerline ($|y/L| = 0$) the flame temperature grows gradually from $x/L = 20$ to 80. In addition, the peak temperature of the flame gradually deviates from the centerline as x/L increases. The three Q2DF cases underestimate the peak temperature of the flame, and as the turbulence develops, this discrepancy tends to become larger with the largest discrepancy of 14%. Additionally, the temperature gradients in the Q2DF cases toward the oxygen sides are smaller than that of the ARF case, which means that the flame in the ARF case is narrower than that in the Q2DF cases, and the flame is the widest in the midstream and lower stream in the Q2DF1 case. The difference among the three Q2DF cases is not large, which means that the three Q2DF cases share similar advantages and shortcomings. In general, the three flamelet models predict the temperature well. The three Q2DF cases achieve fairly good agreement with the ARF case, especially in the upper stream and midstream areas. In the lower stream, for the flame temperature deviation, there are corresponding Z_1 deviations (maximum 7%). It is worth noting that mixture fractions other than that of the fuel also play a role in the lookup process, and variables such as species and temperature may not be precisely consistent with Z_1.

Figure 3.10 presents the profiles for CO_2 and CO mass fractions. The overestimation and underprediction for CO_2 occur at the same position as those for the temperature profile, in the middle and lower streams. It is believed that this deviation

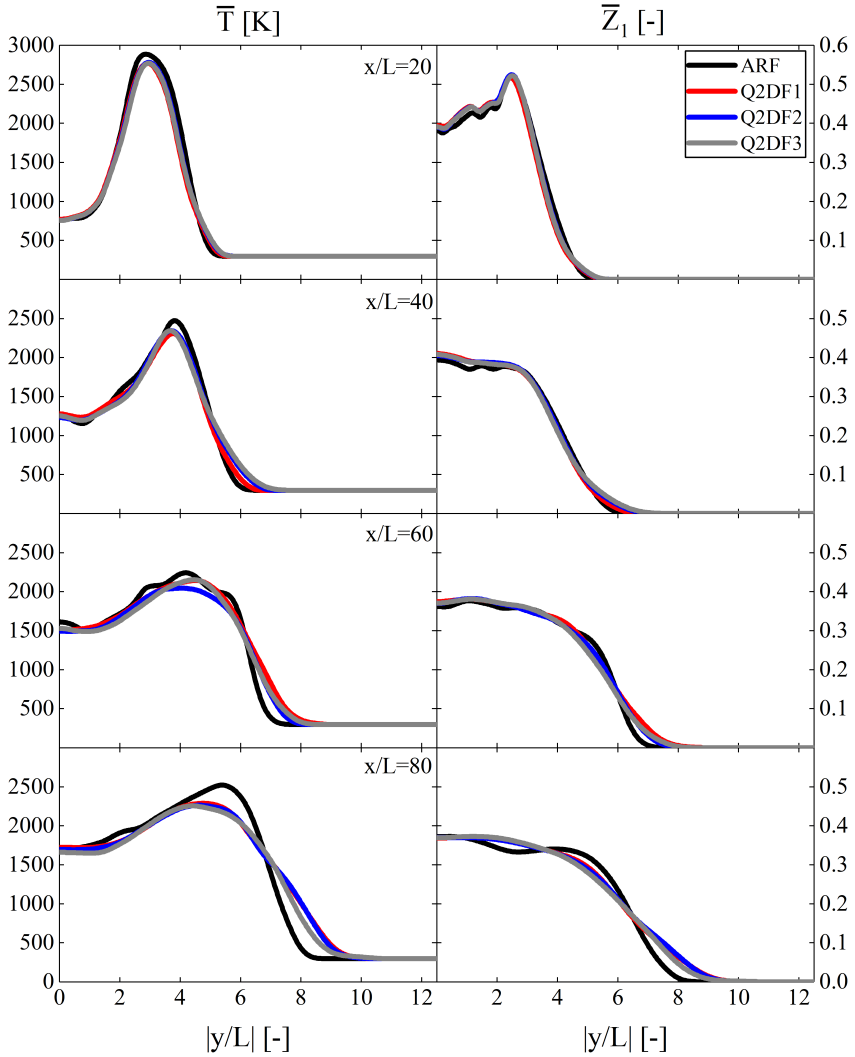

Fig. 3.9 Lateral profiles of time-averaged temperature (a) or fuel mixture fraction (Z_1) (b) at four streamwise locations x/L (top to bottom): 20, 40, 60, and 80.

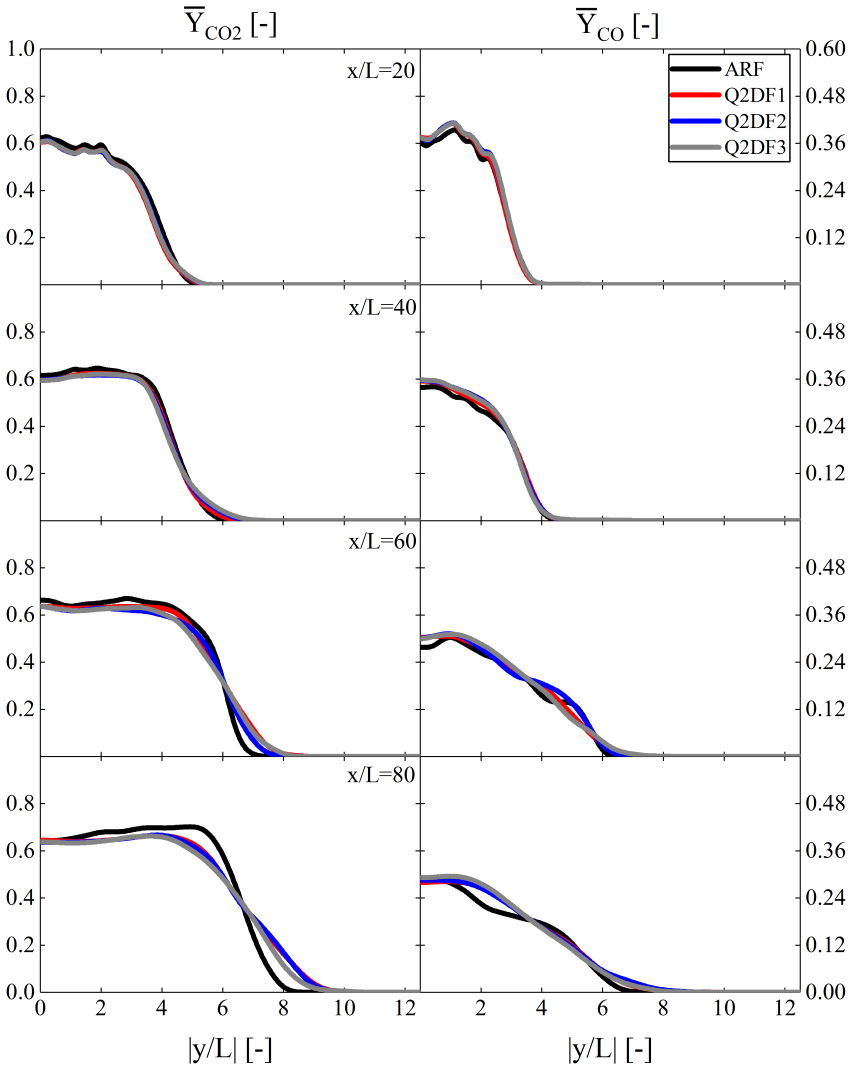

Fig. 3.10 Lateral profiles of time-averaged mass fraction of CO_2 (a) or CO (b) at four streamwise locations x/L (top to bottom): 20, 40, 60, and 80.

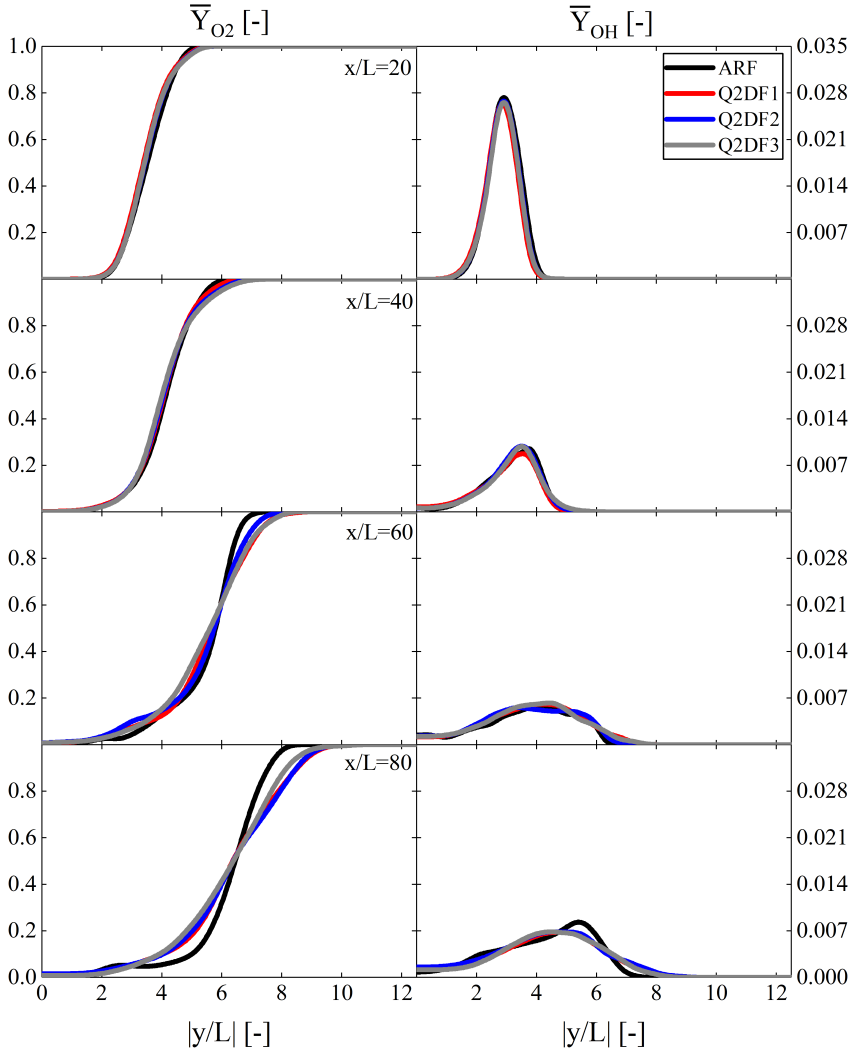

Fig. 3.11 Lateral profiles of time-averaged mass fraction of (a) O_2 or (b) OH at four streamwise locations x/L (top to bottom): 20, 40, 60, and 80.

is largely due to the reaction-generated part, as the peak value is consistent with the peak temperature, which corresponds to the severest reaction; thus, the reaction rate is underestimated by the Q2DF cases. Overall, the CO_2 prediction in the Q2DF cases is also satisfied, although the Q2DF1 case presents a larger deviation at $x/L = 60$. It is expected that CO would be difficult to predict by the non-premixed steady flamelet approach, but very good agreement has been achieved with the Q2DF cases. It is seen that the deviation in Z_1 in the lower stream with $4 \leq |y/L| \leq 6$ does not cause large deviation for CO computation because (as mentioned previously) Z_1 is not the sole parameter in the lookup process. The Q2DF cases perform almost the same and capture the CO variation very well in general.

Figure 3.11 shows the averaged simulation results for the mass fractions of O_2 and OH. The simulation for O_2 and OH variation in the upper stream and midstream is quite good, and the three Q2DF cases predict almost the same results. However, as with CO_2 and CO, a discrepancy is found in the lower stream. In addition, it can be seen that just at the centerline of the domain there is almost no oxygen, which is considered to be caused by severe consumption or limited entrainment. It is observed that at the centerline OH is not exactly zero in the lower stream, which means that combustion is taking place. The predicted peak OH for the Q2DF cases does not match that for the ARF case; this is consistent with the underestimation of temperature in the Q2DF cases.

Figure 3.12 shows lateral profiles for the fluctuation of temperature and Z_1, which are generally predicted by calculating the root mean square (RMS) of the corresponding variables. It is found that the largest deviations essentially arise in the locations corresponding to the sharpest gradient for temperature and Z_1. The Q2DF cases overestimate these fluctuations for both temperature and Z_1. A maximum deviation of 466 K for the temperature fluctuation between the ARF case and Q2DF cases has been computed, whereas for Z_1, the largest gap is 0.07. Around the centerline, however, the fluctuations are predicted well. Among the three Q2DF cases, Q2DF2 generally performs better, although its advantage is very small.

Discrepancy analysis

Although the Q2DF cases generally predict the results in ARF well, some discrepancies occur. It is mentioned in section 3.3.2 that variables such as temperature and species mass fractions are not determined solely by a single mixture fraction, and Figure 3.13 gives the time-averaged lateral distributions of temperature, Z_1, and fuel scalar dissipation rate χ_1 at $x/L = 40$, 60, and 80 for the ARF case. It is found that $\overline{\chi}_1$ has its peak value at the sharpest point of $\overline{Z}_1$ gradient. Generally, the flame front will be formed at these locations [79]; however, except at the location of $x/L = 40$, the behavior of temperature is not synchronized as that of $\overline{\chi}_1$ is, which means that a single scalar dissipation rate is insufficient for establishing a complete database for the three-feed non-premixed combustion system.

As described in section 3.2.2, the three Q2DF models are derived from the two-dimensional flamelet model based on assumptions in terms of the diluent stream. However, as long as the assumptions are adopted, the Q2DF cases formulated do not coordinate exactly with the assumptions. For Q2DF1, the diluent stream has been

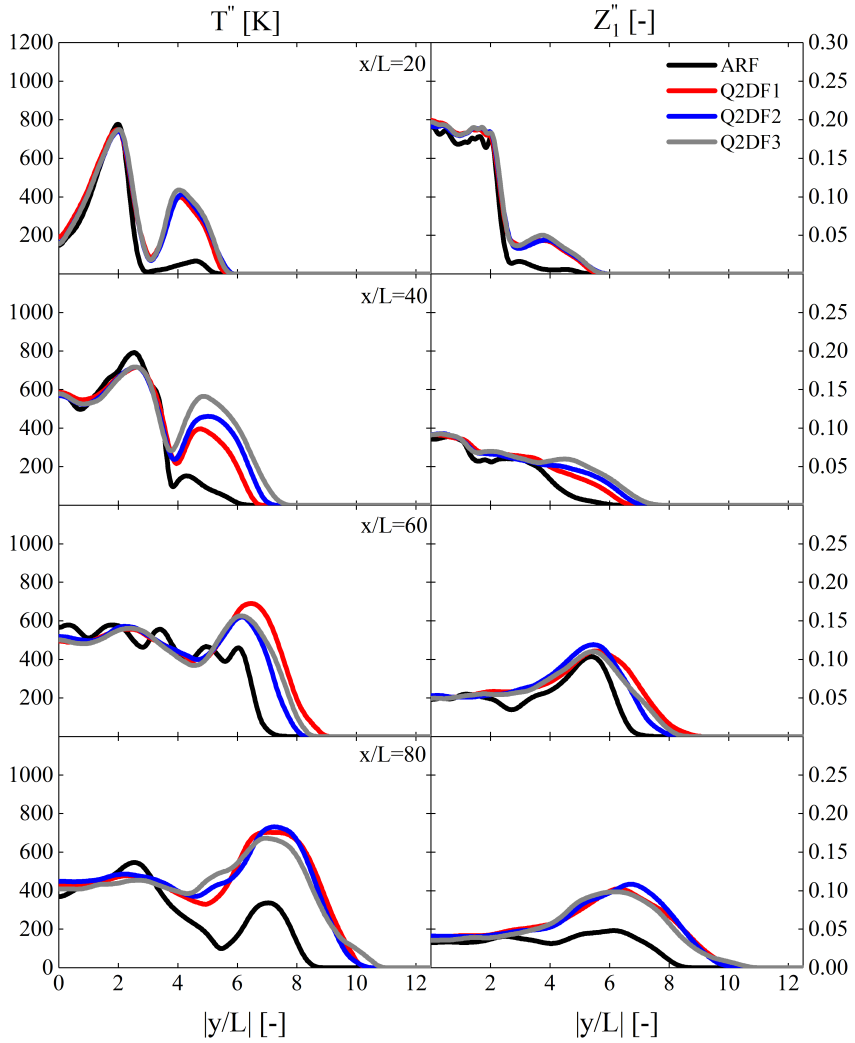

Fig. 3.12 Lateral profiles of RMS of temperature (a) or fuel mixture fractions (Z_1) (b) at four streamwise locations x/L (top to bottom): 20, 40, 60, and 80.

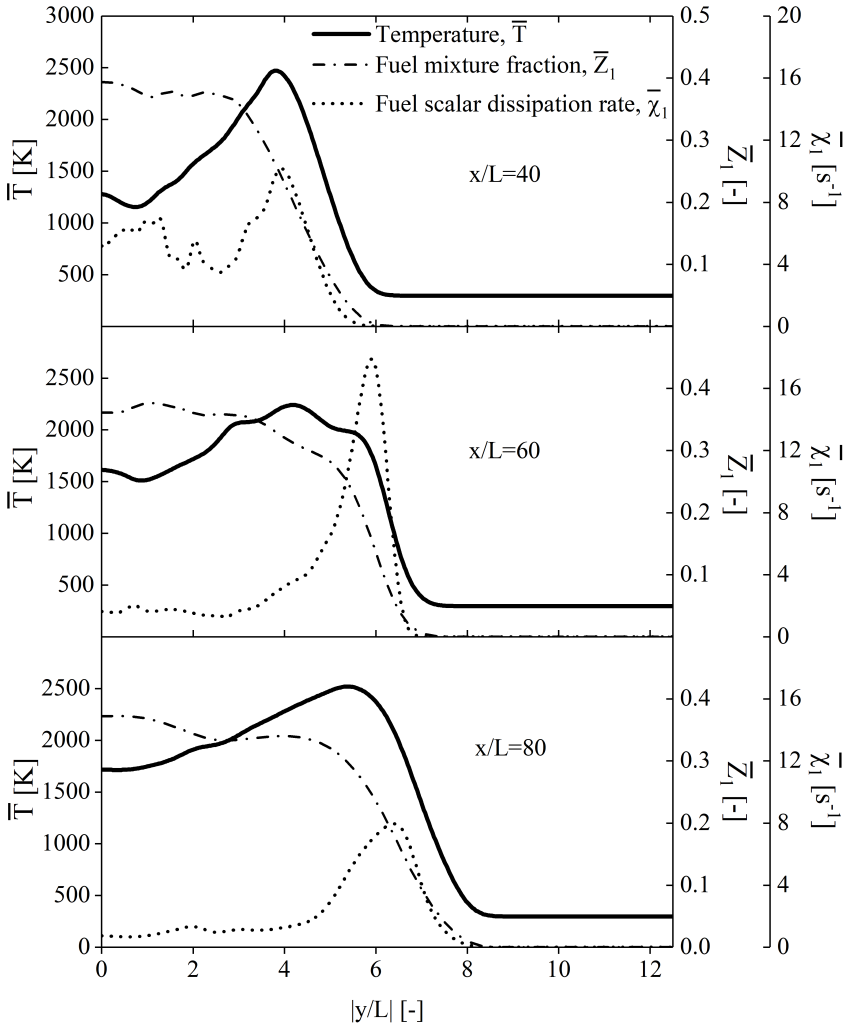

Fig. 3.13 Distributions of time-averaged temperature, fuel mixture fraction, and fuel scalar dissipation rate in physical space, for the ARF case.

classified as belonging on the oxidizer side; however, the diluent mixture fraction is not essentially zero but shares the oxygen mixture fraction with the oxidizer, and the summation is then $1-Z$. This also applies to the Q2DF2, in which the diluent stream shares mixture fraction Z with fuel on the fuel side. Naturally, the cross-scalar dissipation rate for the diluent and oxygen in the Q2DF1 (χ_{23}) or for the diluent and fuel in the Q2DF2 (χ_{13}) should not be overlooked. These cross-scalar dissipation rates can be expressed in Eqs. (3.10) and (3.22).

$$\chi_{23} = 2D\left(\frac{\partial Z_2}{\partial x_i}\right)\left(\frac{\partial Z_3}{\partial x_i}\right). \tag{3.22}$$

Knowing that the sum of the three mixture fractions is unity the cross-scalar dissipation rates in two-dimensional flamelet model can also be given as:

$$\chi_{13} = \frac{1}{2}(\chi_2 - \chi_1 - \chi_3), \chi_{23} = \frac{1}{2}(\chi_1 - \chi_2 - \chi_3). \tag{3.23}$$

The gradient of Z_2 and Z_3 in the Q2DF1 should share the same properties, as well as that of Z_1 and Z_3 in the Q2DF2. Hence, the cross-scalar dissipation rate for the diluent and oxygen in the Q2DF1 or for the diluent and fuel in the Q2DF2 should always have positive values, which differs from that in the two-dimensional flamelet model in the three-feed counterflow system. It is clear that the cross-scalar dissipation rates can be either positive or negative in Eq. (3.23). While the cross-dissipation rate for the fuel and the oxidizer obtained by the two-dimensional flamelet model can be negative and positive, that obtained by Q2DF1 and Q2DF2 models is always negative apparently. The Q2DF3 takes the advantages as well as the disadvantages from both Q2DF1 and Q2DF2, and the model has not been fundamentally promoted. After this DNS investigation, more researches are need to understand the differences among the three Q2DF models, and thus to obtain deeper understanding of the Q2DF models.

Chapter 4

Quasi-Two-Dimensional Flamelet Model for LES

4.1 Background

In the last chapter three Q2DF models have been proposed and validated by a DNS. Although three Q2DF model could achieve good agreements with the reference case, there still remain two problems which need further exploration: (1) what are the differences between the three Q2DF models? (2) what are the fundamental natures for the three Q2DF models? Further more, these models are proposed to tackle with a three-feed non-premixed combustion system, which means it is supposed to be applied to industrial issues. DNS is prohibitively expensive for application in a industrial facility, and in the other hand RANS method is undesirable in terms of the instantaneous phenomena interests and high accuracy. To be compromise, LES is the agreeable approach. Therefore, how to apply the Q2DF models by LES is of great significance in this work.

In this chapter, LES modeling for the tracking parameter will be proposed in terms of Q2DF2 and Q2DF3. Afterwards, LES coupled with the three Q2DF models will be used to compare with the experimental data. In addition, besed on the results, the analysis and discussion of the Q2DF will be made.

4.2 Methodology

4.2.1 LES governing equations

In this study, LES coupled with three Q2DF models is implemented on a three-feed non-premixed combustion system. The governing equations in this study are identical with the mass, momentum, and energy conservation equations which have been presented in chapter 2. Aditionally, the progress variable are solved by the same way in chapter 2. Transport equations for two mixture fractions are solved by Eq. (4.1).

$$\frac{\partial(\overline{\rho}\widetilde{Z}_k)}{\partial t}+\frac{\partial(\overline{\rho}\widetilde{u}_i\widetilde{Z}_k)}{\partial x_i}=\frac{\partial}{\partial x_i}\left(\overline{\rho}\widetilde{D}_{Z_k}\frac{\partial\widetilde{Z}_k}{\partial x_i}\right)+\frac{\partial J^{sgs}_{Z_k}}{\partial x_i},(k=1,2), \tag{4.1}$$

In this chapter, modeling of the subgrid flux and governing equations solving are in the same way as presented in chapter 2 section 2.2.1. $\widetilde{Z}_1$ and $\widetilde{Z}_2$ are the mixture fractions for the fuel and the oxygen stream, respectively, and thus the diluent mixture fraction $\widetilde{Z}_3$ is $1-\widetilde{Z}_1-\widetilde{Z}_2$.

4.2.2 LES coupled with quasi-two-dimensional flamelet model

For a three-feed non-premixed combustion system, the 2DF model is advisable as three mixture fractions are involved in the system. The 2DF formulations in terms of species mass fraction and temperature have been described in chapter 3 section 3.2.2. The Q2DF models are derived from the two-dimensional flamelet model based on the assumptions regarding the third stream, and the detailed information has also been presented in last chapter. It is assumed that the scalar dissipation rate for Z_3 is zero in the three-feed counterflow system and that the diluent stream is placed either in the oxidizer stream (Q2DF1) or the fuel stream (Q2DF2). In addition, the diluent stream can be placed on both the fuel and oxygen sides with an identical mass fraction (Q2DF3). The three options reduce the triple counterflow system by removing the third stream, which makes the Z_3 to be zero; by this way, the two-dimensional flamelet formulation is transferred to a conventional one-dimenisonal flamelet model. In the reduced two-feed counterflow system, for each case, the diluent is mixed with either oxidizer and/or fuel streams with a varing ratio which retains the effects of the third stream, therefore the ratio is essential to distinguish the diffrence among the three models. This ratio is defined as the dilunet fraction, based on which a series

of one-dimensional flamelets is then generated and integrated. The varying diluent fractions are denoted as W_1, W_2, and W_3 for the Q2DF1, Q2DF2, and Q2DF3 cases, respectively; and they can be calculated based on diluent mass fraction.

Here the mixture fraction will be denoted by Z for all reduced one-dimensional flamelet models. For the Q2DF1 model, the diluent fraction and the LES modeling of the mixture fraction can be expressed as

$$W_1 = \frac{\widetilde{Z}_3}{\widetilde{Z}_2 + \widetilde{Z}_3}, \tag{4.2}$$

$$\widetilde{Z} = \widetilde{Z}_1, \tag{4.3}$$

$$\widetilde{Z''^2} = \widetilde{Z_1''^2}. \tag{4.4}$$

In the Q2DF2 case, the entire diluent stream is put on the fuel side, which makes the mixture fraction Z in the one-dimensional flamelet model equal to the sum of the fuel mixture fraction and the diluent mixture fraction. The diluent fraction and the mixture fraction mean value and its variance, which are used to look up the library in LES, are described as

$$W_2 = \frac{\widetilde{Z}_3}{\widetilde{Z}_1 + \widetilde{Z}_3}, \tag{4.5}$$

$$\widetilde{Z} = \widetilde{Z}_1 + \widetilde{Z}_3, \tag{4.6}$$

$$\widetilde{Z''^2} = \widetilde{(Z_1 + Z_3)''^2}. \tag{4.7}$$

Rieth et al. [47] solved a transport equation for the variance above, which makes the calculation complicated. As the summation of Z_1, Z_2, and Z_3 is unity, and also the link of the Favre-filtered variable and the residual fluctuation can be given by [8, 80, 81]

$$\phi = \widetilde{\phi} + \phi'', \tag{4.8}$$

the mixture fraction variance can be written as

$$\widetilde{Z''^2} = \widetilde{Z_2''^2}. \tag{4.9}$$

For the Q2DF3 model, W_3 and the mixture fraction moments are written as

$$W_3 = \widetilde{Z}_3, \tag{4.10}$$

$$\widetilde{Z} = \widetilde{\left(\frac{Z_1}{1-Z_3}\right)}, \tag{4.11}$$

$$\widetilde{Z''^2} = \widetilde{\left(\frac{Z_1}{1-Z_3}\right)}^{''2}. \tag{4.12}$$

In the Q2DF1 and Q2DF2 models, the LES modeling for Z and its variance is quite straightforward, since Z is a linear combination of two-mixture fractions and its variance can be also readily derived; however, Z in the Q2DF3 model is more complicated than in the other two cases, whcih results in complex LES modeling. In the physical flow field, Z_3 is a continuous variable and thus makes Z in Eq. (4.11) non-conserved; this is illustrated in Eq. (4.13). Knowing that Z_1 and Z_3 are both conserved scalars, and Z_1 can be replaced by $Z \times (1-Z_3)$, the transport equation for Z can be derived as

$$\frac{\partial \rho Z}{\partial t} + \frac{\partial (\rho u_i Z)}{\partial x_i} = \frac{\partial}{\partial x_i}\left(\rho D_Z \frac{\partial Z}{\partial x_i}\right) - \frac{2}{1-Z_3}\rho D_Z \frac{\partial Z_3}{\partial x_i}\frac{\partial Z}{\partial x_i}. \tag{4.13}$$

This equation keeps the same form as Eq.(9b) in the literature [39] and then the mean value and variance can be fixed by using the same modeling. However, there are also assumptions and many ignored terms, and physical meanings for some terms are not very clear; in addition, solving additional transport equations makes the computation more laborious. It should be noted that close-knit relationships exist among the three mixture fractions, which makes modeling the mean and variance of Z possible. By expanding $\widetilde{Z}$ and discarding the very small terms such as $\widetilde{(Z_1 Z_3^n)'' Z_3''}$ (n=1, 2, 3, ...), we obtain

$$\widetilde{\left(\frac{Z_1}{1-Z_3}\right)} = \frac{\widetilde{Z}_1}{1-\widetilde{Z}_3} + \frac{\widetilde{Z_2''^2} - \widetilde{Z_1''^2} - \widetilde{Z_3''^2}}{2(1-\widetilde{Z}_3)}. \tag{4.14}$$

As for the variance, neglecting $(Z_1 Z_3^n)''$ (n=2, 3, 4 ...) and other very small terms then

$$\widetilde{\left(\frac{Z_1}{1-Z_3}\right)}^{''2} = \left(1+\widetilde{Z}_3\right)\left(1+\widetilde{Z}_3-\widetilde{Z}_1\right)\widetilde{Z_1''^2} + \widetilde{Z}_1\left(1+\widetilde{Z}_3\right)\widetilde{Z_2''^2} - \widetilde{Z}_1\left(1+\widetilde{Z}_3-\widetilde{Z}_1\right)\widetilde{Z_3''^2}. \tag{4.15}$$

The variance of the three mixture fractions for the corresponding three streams in the above equations can be modeled by

$$\overline{\rho}\widetilde{Z_i''^2} = C_{Z_i}\overline{\rho}\Delta^2 \left|\frac{\partial \widetilde{Z}_i}{\partial x_i}\right|^2, (i = 1,2,3). \tag{4.16}$$

Here the coefficients C_{Z_i} are determined by a dynamic procedure [59].

Three Q2DF models have been given above, however, the zero scalar dissipation rate assumption for Z_3 maybe not consistent with the one calculated in the reduced two-feed counterflow system, since the Z_3 is not discarded directly and its influence is still kept. In the reduced system the Z_3 is mixed with other mixture fractions, and we separate it from the mixtures then the three scalar dissipation rates can be calculated. It is found that there are some correlations for these scalar dissipation rates in each case. For the Q2DF1 model, the relationships among the scalar dissipation rates can be expressed as

$$\chi_1 = \frac{1}{(1-W_1)^2}\chi_2 = \frac{1}{W_1^2}\chi_3. \tag{4.17}$$

The correlations for the three scalar dissipation rates can be also derived for the Q2DF2 model as

$$\chi_2 = \frac{1}{(1-W_2)^2}\chi_1 = \frac{1}{W_2^2}\chi_3. \tag{4.18}$$

For the Q2DF3 model, the corresponding correlations can be described as

$$\frac{1}{(1-W_3)^2}\chi_1 = \frac{1}{(1-W_3)^2}\chi_2, \chi_3 = 0. \tag{4.19}$$

Here, the χ_2 is the scalar dissipation rate for Z_2. In these correlations the χ_3 cannot be zero in the Q2DF1 and Q2DF2 models, and thus only the Q2DF3 observes the zero χ_3 assumption, which means the reduced one-dimensional flamelet formulation for the Q2DF1 and Q2DF2 model may result in dangerous deviations. However, according to the last chapter, in some cases these deviations are not apparent. The reference scalar dissipation rate used to calculate the one-dimensional formulations in the Q2DF1 model is χ_1, whereas in the Q2DF2 model the reference scalar dissipation rate is determined by the fuel side mixture. Knowing that in the reduced two-feed counterflow system, the sum of the mixture fraction in the two sides is unity. For the Q2DF2 model, set the mixture fracion in the fuel side is Z_f and it is Z_o in the oxidizer side, then the reference scalar dissipation rate can be calculated as

$$\chi_\mathrm{ref} = 2D\frac{\partial Z_\mathrm{f}}{\partial x_i}\frac{\partial Z_\mathrm{f}}{\partial x_i} = 2D\frac{\partial\left(1-Z_\mathrm{o}\right)}{\partial x_i}\frac{\partial\left(1-Z_\mathrm{o}\right)}{\partial x_i} = 2D\frac{\partial Z_\mathrm{o}}{\partial x_i}\frac{\partial Z_\mathrm{o}}{\partial x_i} = \chi_2 \tag{4.20}$$

It is obvious that χ_3 is a function of the reference scalar dissipation rates. When the diluent fraction is large then the W_1^2 and W_2^2 in the Q2DF1 and Q2DF2 models cannot be neglected, making the χ_3 is the same order of the magnitude with the reference scalar dissipation rates. It is also observed that when the reference scalar dissipation

rates are very small a tiny χ_3 can be also achieved even the diluent fraction is large. Based on the above, the Q2DF1 and Q2DF2 models are valid on the condition that either the diluent fraction is such a tiny value that its square can be ignored or the reference scalar dissipation rates are so small that the χ_3 can be neglected.

On the basis of the three models, steady flamelet calculations were performed by using the FlameMaster code [66]. The tracking variables and resolution in the flamelet libraries can be found in Table 1 in the last chapter. These three libraries have been used for DNS validation cases previously as shown in the last chapter. It should be noted that, for all the three cases above, in each library, Z is a conserved scalar owing to the discrete distribution of Z_3. Therefore, to obtain the variable mean values, the β-pdf is still appropriate. The flamelet solutions regarding the temperature and the CO_2 mass fraction based on a unity stoichiometric scalar dissipation rate are demonstrated in Figure 4.1. In the present work, GRI-Mech ver.3.0 [72] is used for all three cases, in which 53 species and 634 reactions are included.

4.2.3 Experiment and computational details

In the current study, the burner and the reactor in the simulations are identical with the facilities in experiments that were described in previous reports [82, 83]. The schematic of the core section is shown in Figure 4.2(a). Three streams were conveyed into the annual configuration of the swirl burner. Fire-resistant material was applied on the inside wall of the reactor, while on the outside wall, a water-cooled copper tube was arranged to for cooling. The geometry of the burner comprised three layers of circularly arranged nozzles as shown in Figure 4.2(b) and (c). Fuel and oxygen nozzles were arranged alternately on the same innermost circumference with a swirl angle of 25°. The diameter of the fuel nozzles was 1.7 mm, whereas it was 1.3 mm for the oxygen nozzles. The other two layers were set for the diluent stream, in which the outermost was for the direct flow nozzles with a diameter of 1.2 mm, whereas the swirling angle was 30° and the diameter was 2.4 mm for the rest. Fuel and oxygen were issued at a rate of 103.0 L/min and 35.1 L/min, respectively, whereas that of diluent amounted to 654.7 L/min. The surrounding pressure and other information of the inflow streams are listed in Table 4.1. The reactor part also beared the gas sampling and temperature measuring holes at various lengths that corresponded to distances from the burner outlet along the axial direction. The distances (x) were x = 120 mm, x = 260 mm, x = 400 mm, x = 580 mm, and x = 800 mm; all the available experimental results were obtained through experiments performed at the Central

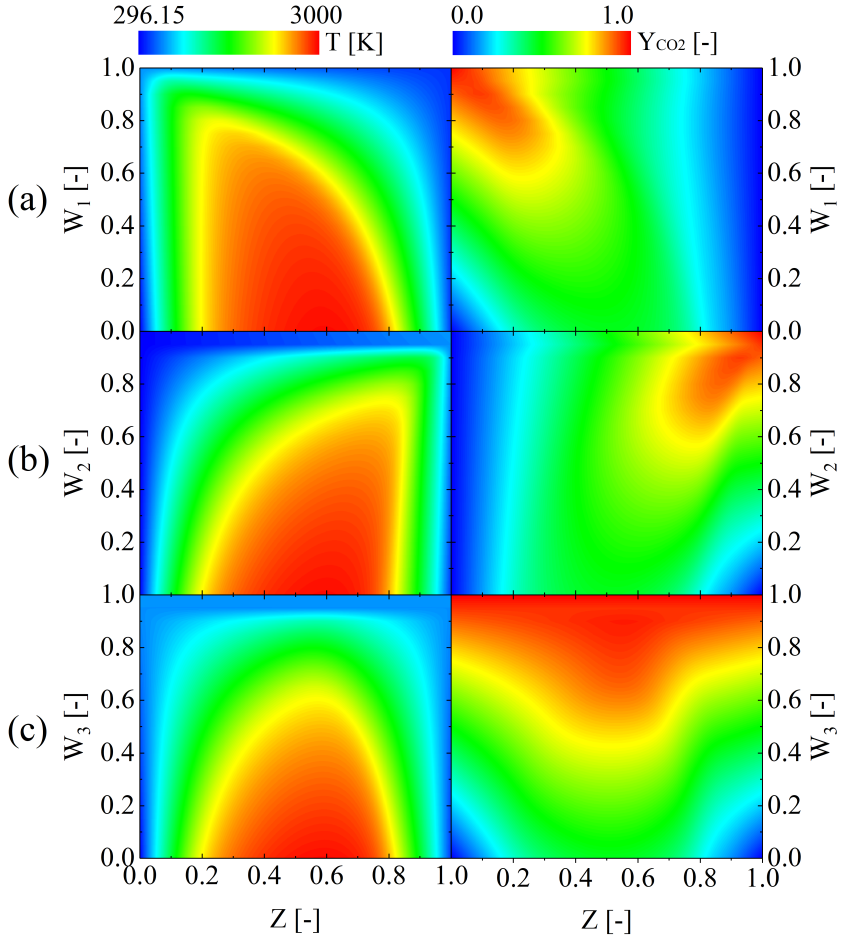

Fig. 4.1 Flamelet solution of the temperature and CO_2 mass fraction for three quasi-two-dimensional (Q2DF) model cases. The flamelet here is a function of mixture fraction Z and diluent fraction W and is evaluated at a constant stoichiometric scalar dissipation rate of $\chi_{Z,st}$=1s^{-1}. The W_1 coordinate axis is for Q2DF1 case, W_2 is for the Q2DF2 case, and W_3 is for the Q2DF3 case.

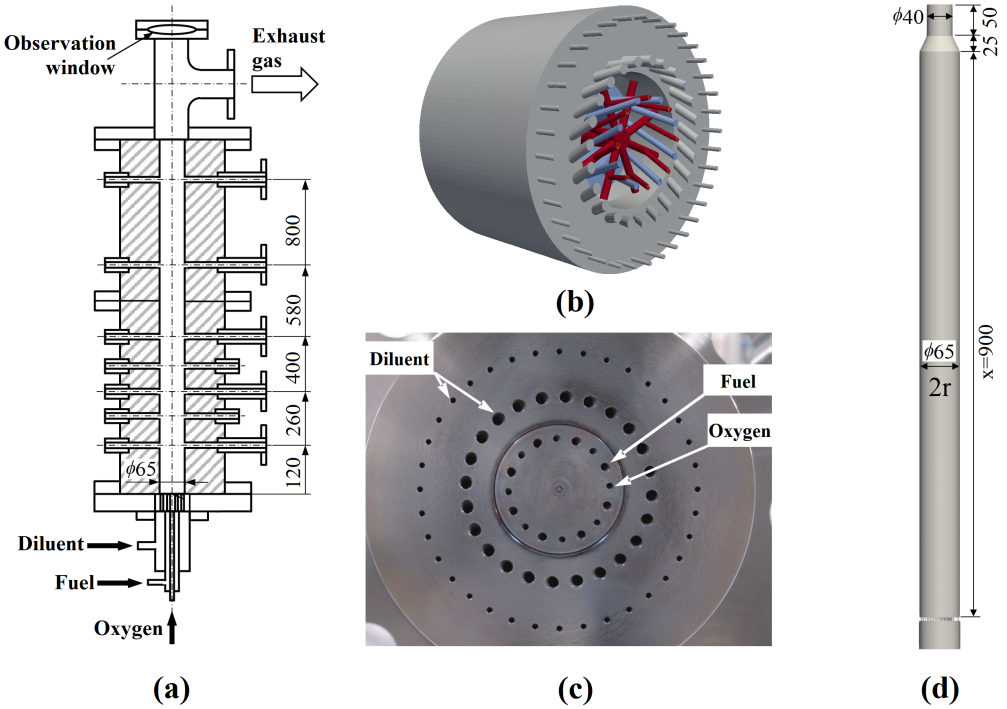

Fig. 4.2 Experimental reactor and computational domain (length unit: mm).

Table 4.1 Boundary conditions for LES.

Compounds in fuel stream(mass fraction)	
CO	0.9749
H_2	0.0251
Compounds in Oxidizer stream(mass fraction)	
O_2	1.0
Compounds in diluent stream(mass fraction)	
CO_2	1.0
Volume flux,L/min	
Fuel	103
Oxidizer	35.1
Diluent	654.7
Temperture, K	
Fuel inlet	433.35
Oxidizer inlet	296.15
Diluent inlet	693.45
Surrounding pressure, atm	1.0

Research Institute of Electric Power Industry in Japan (CRIEPI) and will be used as reference data for the model validation in this study.

A sketch of the computational domain is illustrated in Figure 4.2(d). The inner diameter of the reactor cylinder is 65 mm (2r), and the length is 900 mm (x). The computational domain consists of roughly 7.1 million unstructured cells with finer cells arranged in the upper stream. The simulations were performed by employing the unstructured code FFR-Comb (NuFD/FrontFlowRed), which was extended by Kyushu University, Kyoto University, CRIEPI and NuFD [19, 64, 65]. Spatial derivatives were discretized by the second-order finite volume formulations [19]. For each case, a total of 576 cores of Fujitsu PRIMERGY CX2550/CX2560 M4 at Kyushu University were used, and the wall clock time was around 95 h with constant time step interval of 5×10^{-7}s. The largest convection Courant number was about CFL=0.35-0.4. Each simulation was performed for 250,000 steps to eliminate the effect of the initial field, ensuring the reacting flow to be fully developed in the entire domain. Another 240,000 steps were calculated to collect time-averaged statistics. The instantaneous variables used in the following discussions were obtained from the last step.

4.3 Results and discussion

4.3.1 Model Comparisons and Validation

Figure 4.3 shows the instantaneous mixture fraction scatter plots for the three cases. Three white empty areas are idendified and marked as A_i, B_i, and C_i (i=1,2,3). It is found that almost everywhere in the flow field, all three mixture fractions are involved in the mixing process, since none of the areas is zero. Regions completely lacking one of the three streams only occur in the inflows. The well achieved mixing of the three mixture fractions are appropriate for the investigation of the three Q2DF models.

To validate the three Q2DF models, the time-averaged variables are compared with experimental data in this section. It should be mentioned here that the species mole fractions discussed in the present work were obtained based on a dry gas sample, i.e., a sample in which the steam has been removed.

Figure 4.4 compares the experimental results with the radial profiles of the time-averaged temperature and the time-averaged oxygen mole fraction ($\overline{X}_{O_2}$) at different

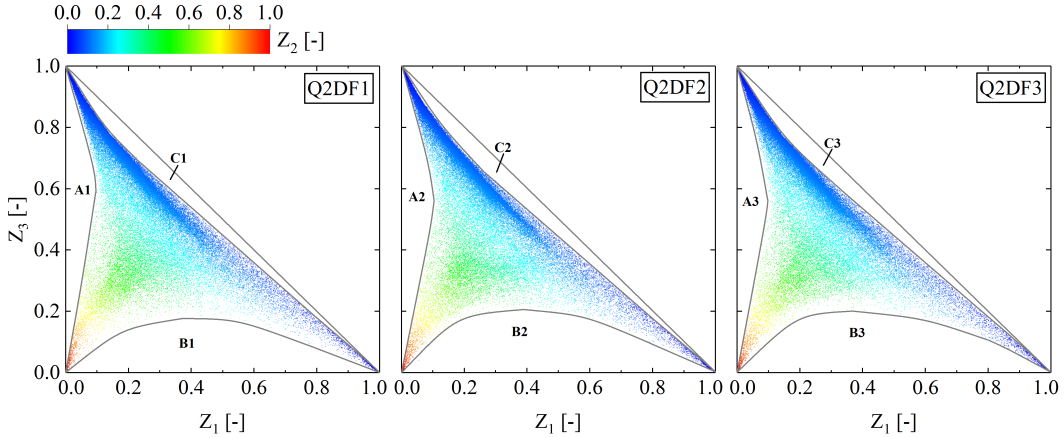

Fig. 4.3 Scatter plots of instantaneous diluent mixture fraction (Z_3) and fuel mixture fraction (Z_1), colored by oxygen mixture fraction (Z_2), for the three cases (top to the bottom): Q2DF1, Q2DF2 and Q2DF3.

axial locations. It is found that the temperature measured at r = 10 mm is higher than that on the center regarding four cross-sections from x = 120 mm to x= 580 mm, although the difference is not apparent in the lower stream. Furthermore, the temperature starts to reduce radially outward from this point (r = 10 mm) on. This is attributed to the flow field that has been mentioned in section 3.1. As x = 800 mm, the temperature decreases continuously from the center point towards the wall owing to the heat transfer and the fully developed mixing of all the flows in the lower stream. This trend has been captured well by the three Q2DF model cases. Among the three Q2DF model cases, the Q2DF3 case has the highest temperature result, while the Q2DF1 case has the lowest one. As mentioned in section 3.2.1, the heat lost plays an important role in the experiments in this work. It should be mentioned that a nonadiabatic FPV would be more desirable with regards to the heat loss [25–27]. However, the adiabatic FPV is adopted here for the sake of a good resolution as another dimension (Δh) has to be added in the library in the nonadiabatic FPV. In addition, this work is mainly focused on the diluent fractions, which are W_1, W_2 and W_3 in the three Q2DF models.

The oxygen is already low at x = 120 mm and it is almost completely depleted at the next measurement plane. All the three cases overestimate the oxygen value, and the Q2DF3 model case exhibit the best performance. It can be seen that the $\overline{X}_{O_2}$ increases from the center towards the wall in the cross-section of x = 120 mm, x = 260 mm, and x = 400 mm. The three cases and especially the Q2DF3 model case can capture this trend in the cross-section located at x = 120 mm, while all of them present stable distributions beyond this location. In the downstream region,

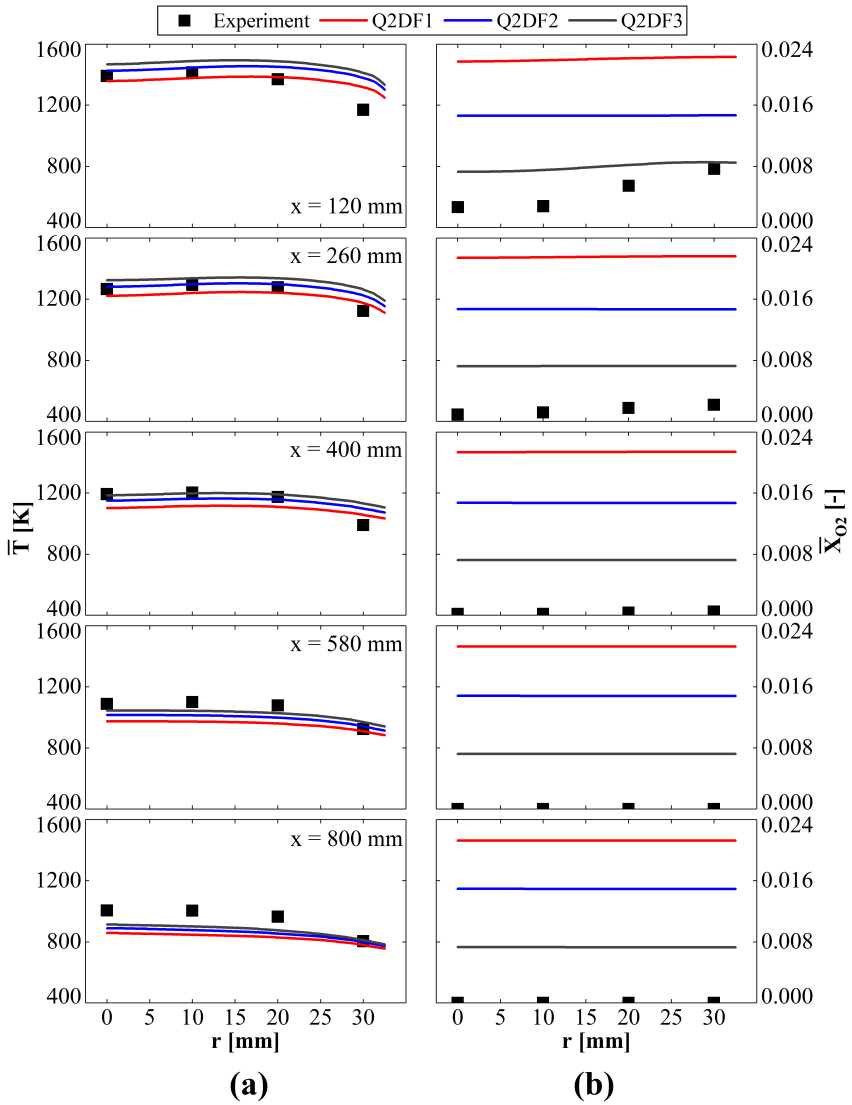

Fig. 4.4 Radial profiles and experiment results of time-averaged temperature (a) or O_2 mole fraction (X_{O_2}) in dry gas sample (b) at five streamwise locations x (top to the bottom): 120 mm, 260 mm, 400 mm, 580 mm, and 800 mm.

even the best agreement is with the Q2DF3 model, which predicts approximate 0.8% of $\overline{X}_{O_2}$, while O_2 is almost zero in the experimental measurements. Figure 4.5 illustrates the performances of the three model formulations in terms of the time-averaged mole fractions of CO_2 ($\overline{X}_{CO_2}$) and CO ($\overline{X}_{CO}$). The Q2DF3 model case gives a fairly accurate prediction for $\overline{X}_{CO_2}$ in the cross-section located at x = 120 mm, while the deviations for the Q2DF1 and the Q2DF2 model cases are 6.55% and 2.36%, respectively. The deviations for the three cases increase gradually along the streamwise direction, although the discrepancies are still small. This trend is similar for the prediction of $\overline{X}_{CO}$. There are some remaining deviations in CO predictions provided by the steady FPV approach [13], and the results have been greatly improved by an unsteady FPV method [28]. However, CO prediction given by the steady flamelet model have been found reliable in some other studies [47]. In the present case, the Q2DF3 model case provides a satisfactory prediction, although CO is a dominant species composition of the fuel stream.

Overall, the three cases can give a good prediction of the temperature distribution, and the Q2DF3 model outperforms the other two formulations in terms of the time-averaged mole fractions of species.

4.3.2 Analysis of remaining discrepancies

As discussed in section 2.2, the reduced one-dimensional flamelet formulations for Q2DF1 and Q2DF2 model are valid only when the diluent fracion square or the χ_3 can be ignored. Figure 4.6 shows the square of diluent fraction for the Q2DF1 and Q2DF2 model models, and the χ_3 has also been examined for all three cases. It has been found that the square of the diluent fraction is uniformly distributed in the experimental measurement planes with a value larger than 0.8; this large diluent fraction will make the χ_3 cannot be overlooked if χ_1 is large. However, the χ_1 is small in these positions since the χ_3 observed is a tiny value. This is considered the reason even the diluent fraction is large the prediction of the Q2DF1 and Q2DF2 models still can provide a reasonable prediction.

The small χ_3 make the reduced formulation valid for the all three cases, but the comparisons with experimental data reveal that the three formulations perform differently. To further investigate why this is the case, the mixture fractions of the three streams and the root mean square of the velocities inside the reactor were checked for the three cases. Figure 4.7 shows Z_1 and Z_2 in the experimental measurement planes as function of radial direction for all three cases. The comparison shows that

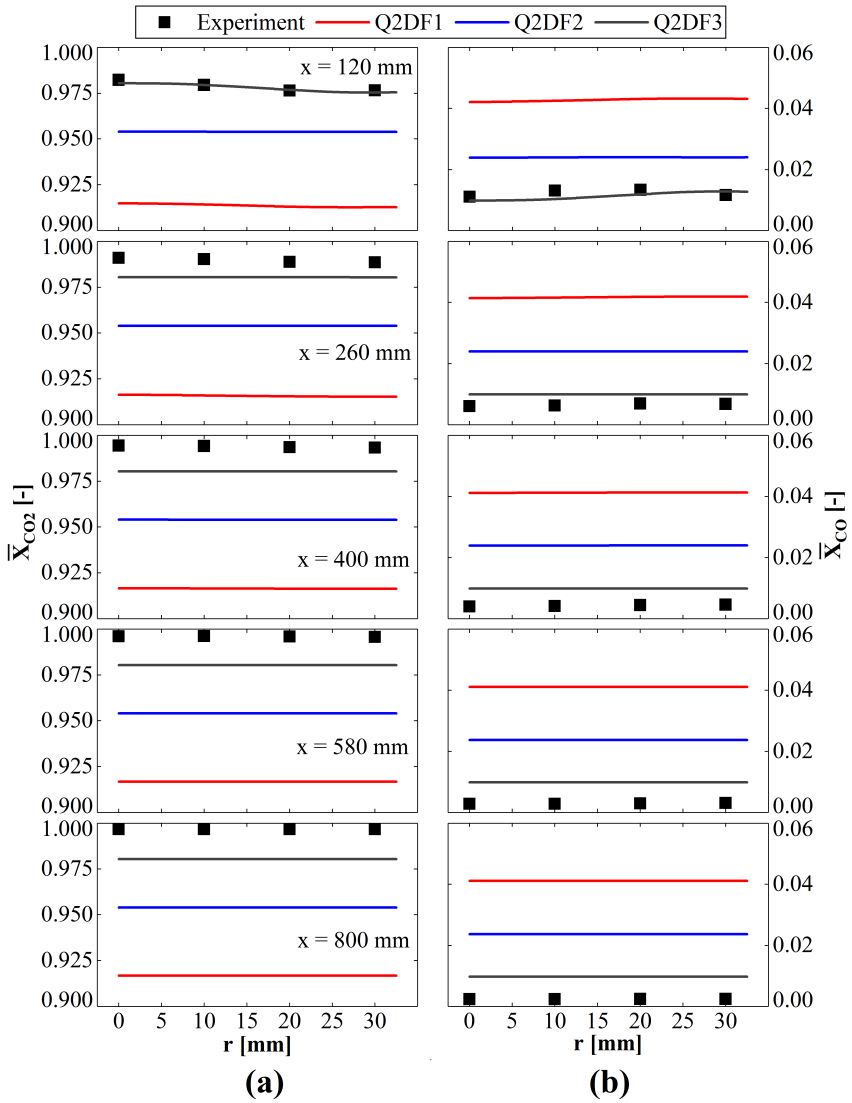

Fig. 4.5 Radial profiles and experiment results of time-averaged CO_2 mole fraction (X_{CO_2}) (a) or CO mole fraction (X_{CO}) (b) in the dry gas sample at five streamwise locations x (top to the bottom): 120mm, 260 mm, 400 mm, 580 mm, and 800 mm.

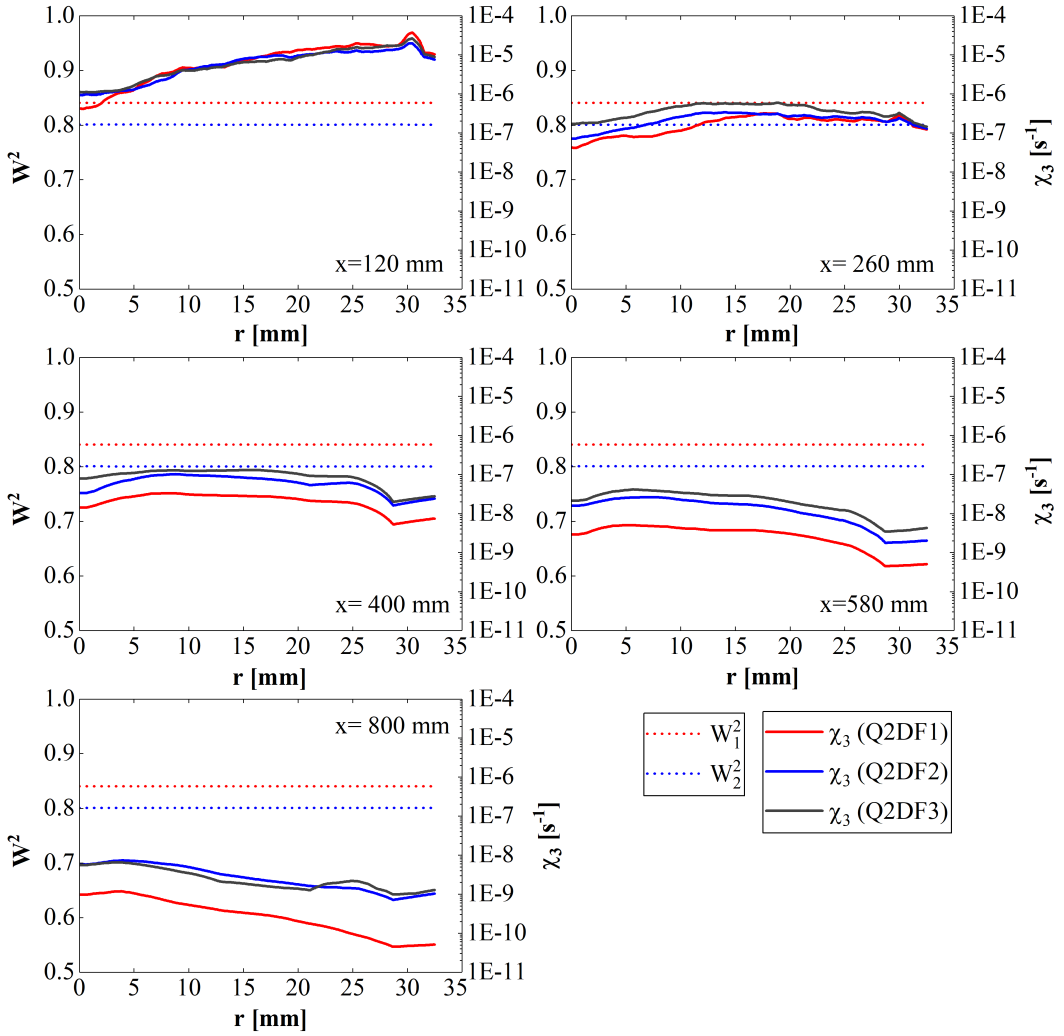

Fig. 4.6 Radial profiles of the time-averaged diluent fraction sqaure (W_1^2 for the Q2DF1 model, W_2^2 for the Q2DF2 model) and the time-averaged scalar dissipation rate for the diluent stream at five streamwise locations x: 120mm, 260 mm, 400 mm, 580 mm, and 800 mm.

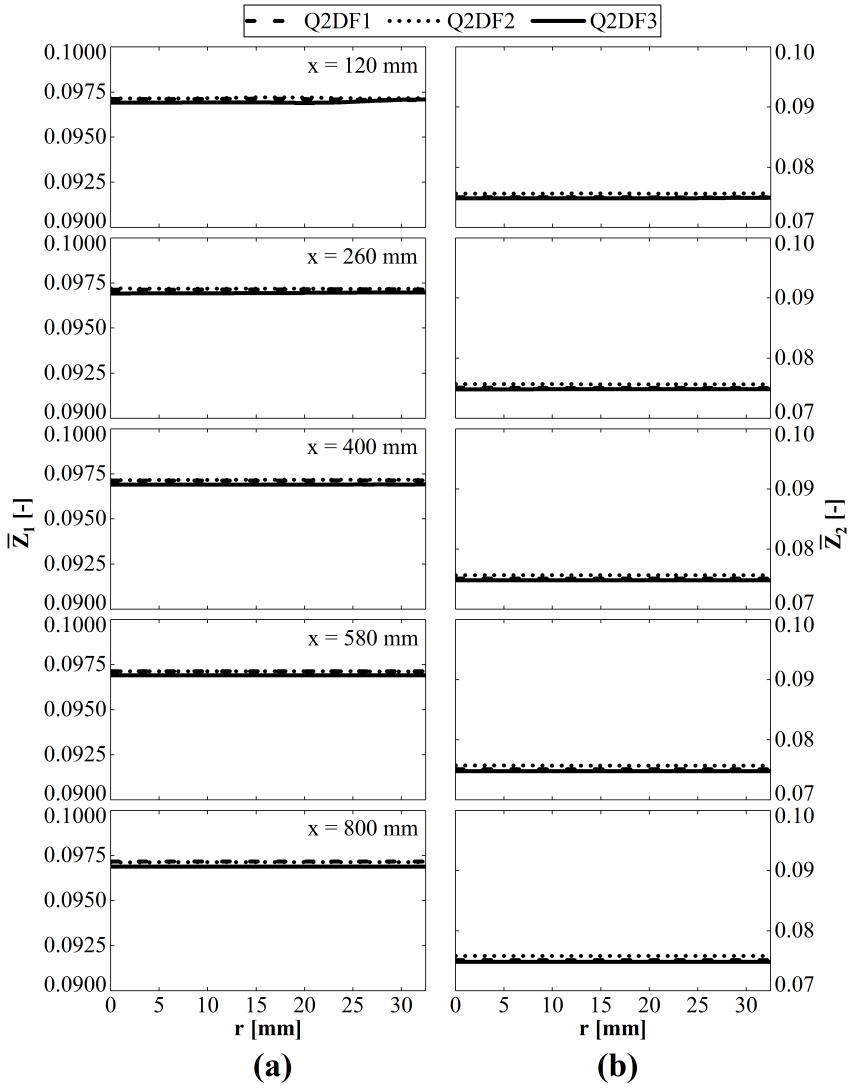

Fig. 4.7 Radial profiles of the time-averaged fuel mixture fraction (Z_1) (a) or oxygen mixture fraction (Z_2) (b) at five streamwise locations x (top to the bottom): 120mm, 260 mm, 400 mm, 580 mm, and 800 mm.

the three cases have almost the same mixture fraction distributions. Figure 4.8 shows the velocity fluctuations in the same locations. $\langle U'^2 \rangle^{1/2}$ and $\langle V'^2 \rangle^{1/2}$ are the root mean squares for the axial velocity and radial velocity, respectively. Except for areas close to the center on the cross-section of x = 260 mm, the differences in the velocity fluctuation for the three cases are very small, which means the computed flow fields for the three cases are almost the same.

Other than the measurement plane, the flow fields computed by the three cases are also worth checking. Figure 4.9 shows a snapshot of the instantaneous distributions of Z_3 for the three cases. It can be seen that the lean diluent ($Z_3 < 0.2$) areas are restricted to a very small area near the fuel and the oxygen inflows. There difference is very small for the three cases with regard to the Z_3 distribution, and considering the distributions of Z_1 and Z_2 in Figures. 4.3, the all three cases basically predict similar mixture distributions in the whole domain; this allows us to directly compare the three models, as the mass fractions are obtained on the basis of the libraries mapping process. The instantaneous scatter plots for species mass fractions are considered the reproductions of the lookup results, so it is also interesting to check them. Figure 4.10 shows instantaneous scatter plots for the mass fractions of CO_2 (Y_{CO_2}), CO (Y_{CO}), O_2 (Y_{O_2}), and OH (Y_{OH}). The inflows can be described by three points in which a unity Y_{CO_2} and a zero Z_1 are the diluent inflow, and a zero Y_{CO_2} with zero or unity Z_1 defines oxygen stream or fuel stream, respectively. The instantaneous Y_{CO_2} distributions differ among cases in the vicinity of the diluent inflow ($Z_1 < 0.1$), which is consistent with the Z_3 distributions that were previously mentioned. Overlapping areas exist because the lookup results are not only determined by a single mixture fraction. Consistent with the scatter plots for Y_{CO_2}, Y_{CO} of the different inlets can be found in the instantaneous Y_{CO} scatter plots. Near both oxygen and fuel inflow, there are differences in the Y_{CO} distribution among the three cases. In the vicinity of the diluent inflows ($Z_1 < 0.1$), there are apparent differences in the Y_{O_2} distributions but not for Y_{OH}. OH is a radical generated only in the reaction regions and there are almost no reactions in areas near the diluent inflows. Overall, for each case, the main features for the instantaneous distributions are identical in terms of instantaneous Y_{CO_2}, Y_{CO}, Y_{O_2}, and Y_{OH}, but differences also exist concerning lookup results.

The three cases present similar flow field, however, give different predictions of the time-averaged scalar variables in terms of the temperature and the typical chemical species concentrations, illustrating that the databases and the lookup procedures of the three models play essential roles. In the current study, the flux of the diluent stream is much larger than that of the other two streams, especially for the

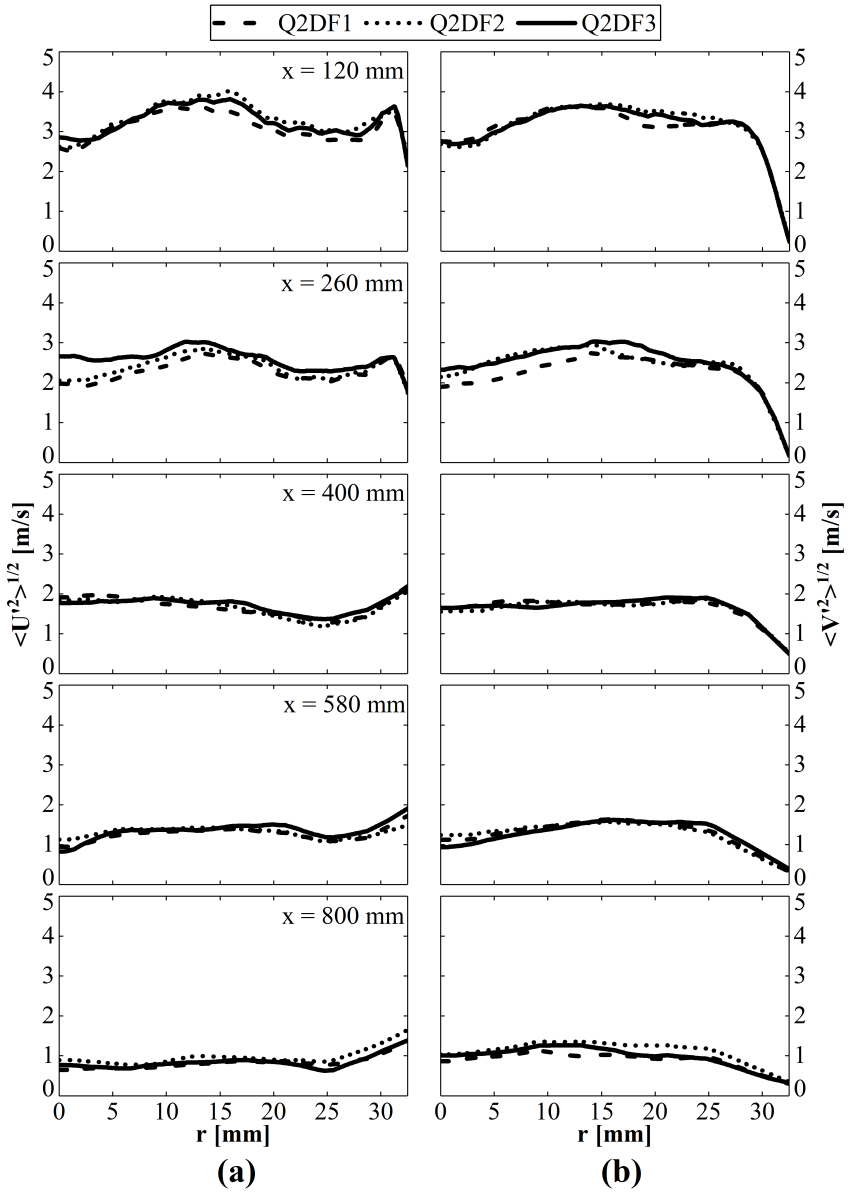

Fig. 4.8 Comparisons of the velocity root mean square for the three cases on the measurement cross-section: (a) axial velocity root mean square and (b) radial velocity root mean square.

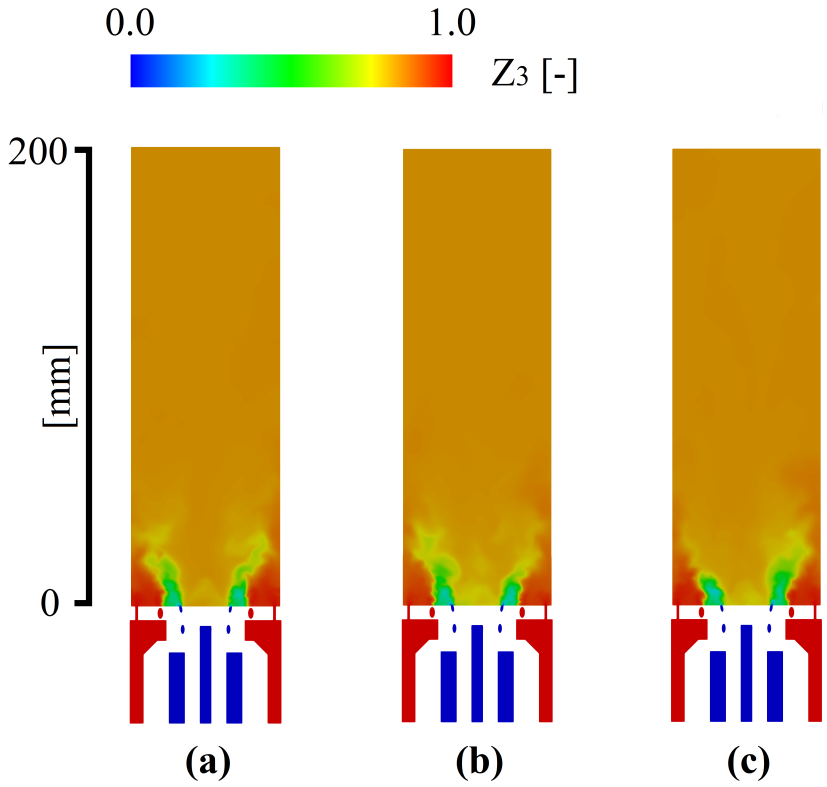

Fig. 4.9 Instantaneous distributions of diluent mixture fractions for the three cases: (a) Q2DF1, (b) Q2DF2, and (c) Q2DF3.

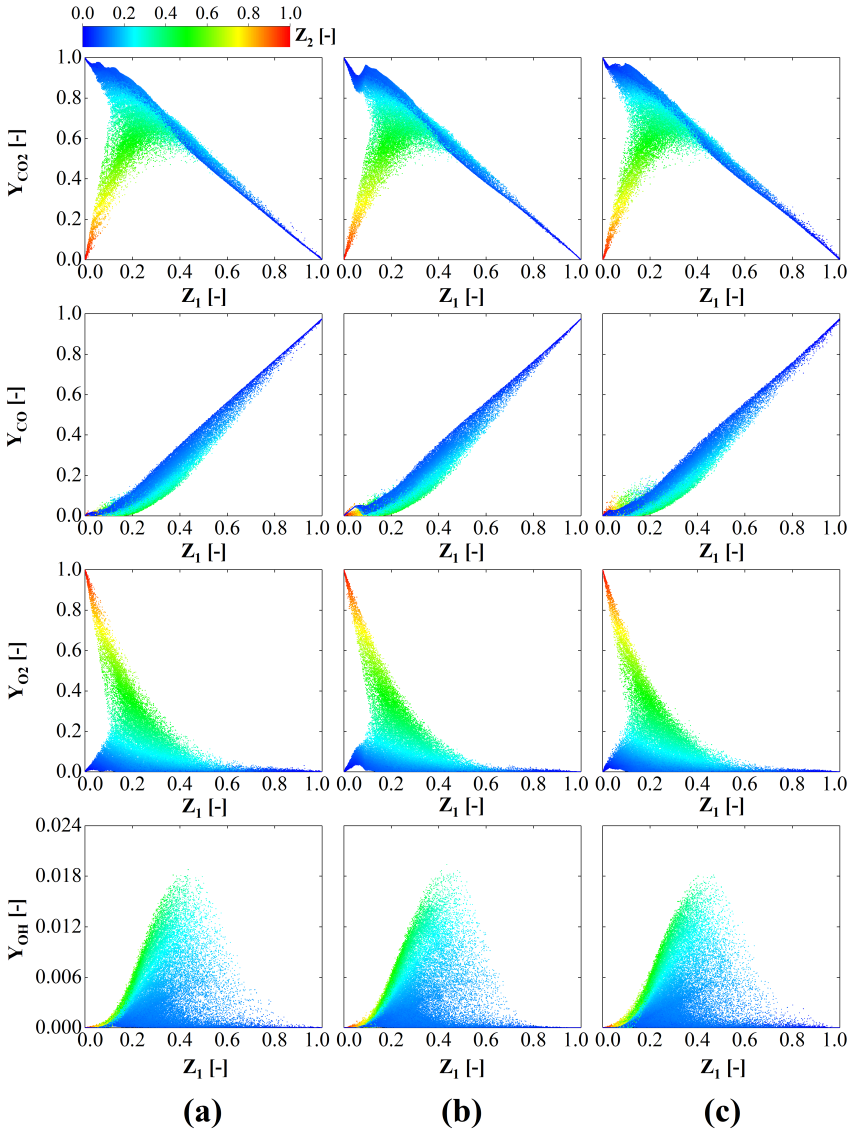

Fig. 4.10 Scatter plots of the instantaneous mass fraction of CO_2, CO, O_2, or OH (top to the bottom) and fuel mixture fraction (Z_1), colored by the oxygen mixture fraction (Z_2), for the three cases (left to the right): (a) Q2DF1, (b) Q2DF2, and (c) Q2DF3.

fuel, and the effect of Z_3 in the lookup process is therefore enormous. This would become more apparent if the tracking parameters were checked. These parameters have been described in section 2.1 and section 2.2, and summarized in Table 1 in the last chapter. It was found that, in the Q2DF3 model, the diluent fraction W_3 is exactly equal to the Z_3, which makes the influence direct. Although Z_3 is also included in W_1 and W_2, the influence is weaker than that of W_3. It was also noticed that Z_3 is considered in the $\widetilde{Z}$ and the $\widetilde{Z''^2}$ expressions for the Q2DF2 and the Q2DF3 models, but not in the Q2DF1 model. This is considered to be a reason why the Q2DF3 model outperforms the other two, and the Q2DF1 model offers no advantages in the current computation.

Besides the differences among the three Q2DF models, the discrepancies between three Q2DF cases and the experimental results are also of interest of model applications. The 2DF formulations can be reduced to a one-dimensional model on the basis of a zero scalar dissipation rate assumption for Z_3 in the three-feed counterflow system, which also results in a zero cross-scalar dissipation rate for the diluent and the two reactant streams. However, as for the established Q2DF model, for each corresponding one-dimensional flamelet library, the influence of the diluent stream still plays a very important role as mentioned before, and the diluent streams influence the model through the cross-scalar dissipation rates. In the Q2DF1 model, the diluent and oxygen form a mixture in which the two groups of mixture fractions move in the same direction locally owing to convection and diffusion. This is also applied to the fuel and diluent streams in the Q2DF2 model. As in the Q2DF3 model, the mixtures for the fuel and oxidizer sides both include the diluent, making the situation more complicated. The arrangement of the counterflow makes the cross-scalar dissipation rate for oxygen and the diluent positive, whereas it is negative for the diluent and fuel in the Q2DF1 model. In the same way, for the Q2DF2 model, the cross-scalar dissipation rate is positive for the diluent and the fuel, and it is negative for the diluent and oxygen. In the Q2DF3 model, however, the cross-scalar dissipation rates for the diluent and any reactant stream can be both positive and negative. It should be noted that the cross-scalar dissipation rate for the fuel and oxygen streams are always negative in the three models, which is different from that in a three-feed counterflow system. Overall, in terms of the cross-scalar dissipation rate, the Q2DF3 model is closer to a two-dimensional flamelet model in a three-feed counterflow system. However, this advantage does not work as shown in the last chapter, as Z_3 does not dominate the flow field.

According to Eqs. (4.17), (4.18), and (4.19), the inherent relationships among the three scalar dissipation rates exist in the Q2DF models, which may be not consistent with the flow field. Actually, in the 2DF model, there is no correlation limitation for the reference scalar dissipation rates of the three streams. To generate a 2DF library, all reference scalar dissipation rates in the flow field in theory can be specified. For instance, Figure 4.11(a) shows the typical flamelet results obtained from the 2DF formulations, in which the reference scalar dissipation rates for Z_1 ($\chi_{1,st}$), Z_2 ($\chi_{3,st}$), and Z_3 ($\chi_{3,st}$) are all unity. The boundary conditions such as temperature and species compositions are exactly the same as those used for solving the Q2DF formulations. For numerical convenience, the $Z_1 \times Z_3$ triangle space is transformed into a $\varepsilon \times \eta$ square space in the 2DF model. In this study, the chosen transformation is the one used by Doran [84], which can be given as:

$$\varepsilon = Z_1, \eta = \frac{Z_3}{Z_2 + Z_3}. \tag{4.21}$$

The corresponding scalar dissipation rates such as χ_ε, χ_η, and $\chi_{\varepsilon\eta}$ and the transformed 2DF formulations can be also found in the literature [84]. It is found that the space $Z \times W_1$ in the Q2DF1 model is identical with the $\varepsilon \times \eta$ in Doran's format according to Eqs. (4.2), (4.3), and (4.21). However, differences exist in the treatments of W_1 and η. W_1 is a discrete parameter in the Q2DF1 model, whereas η is continuously distributed in the 2DF formulations. Figure 4.11(b) is the result used in Figure 4.1(a), and the contour lines are shown simultaneously to make the comparisons clearer. For Figure 4.11(a) and Figure 4.11(b), the colors of the right side contour lines are consistent with the temperature in the left contour, and the same color corresponds to the same temperature for the contour lines in the two cases. Differences can be observed as comparisons are made between Figure 4.11(a) and Figure 4.11(b), especially when the diluent fraction is large; thus, the weakness of the Q2DF model can be found. First, in the Q2DF1 model, as the reference scalar dissipation rate (equal to $\chi_{1,st}$) is set to unity, $\chi_{2,st}$ and $\chi_{3,st}$ cannot be unity simultaneously. In addition, $\chi_{2,st}$ and $\chi_{3,st}$ are varied when W_1 is changed, but this variation is restricted according to Eq. (4.17). This would also be applied to the Q2DF2 and Q2DF3 models as the corresponding space transformations can be made in the 2DF model. Hasse et. al. [41, 42] transformed the triangle space in another way which is given as

$$\varepsilon = Z_1 + Z_3, \eta = \frac{Z_3}{Z_1 + Z_3}. \tag{4.22}$$

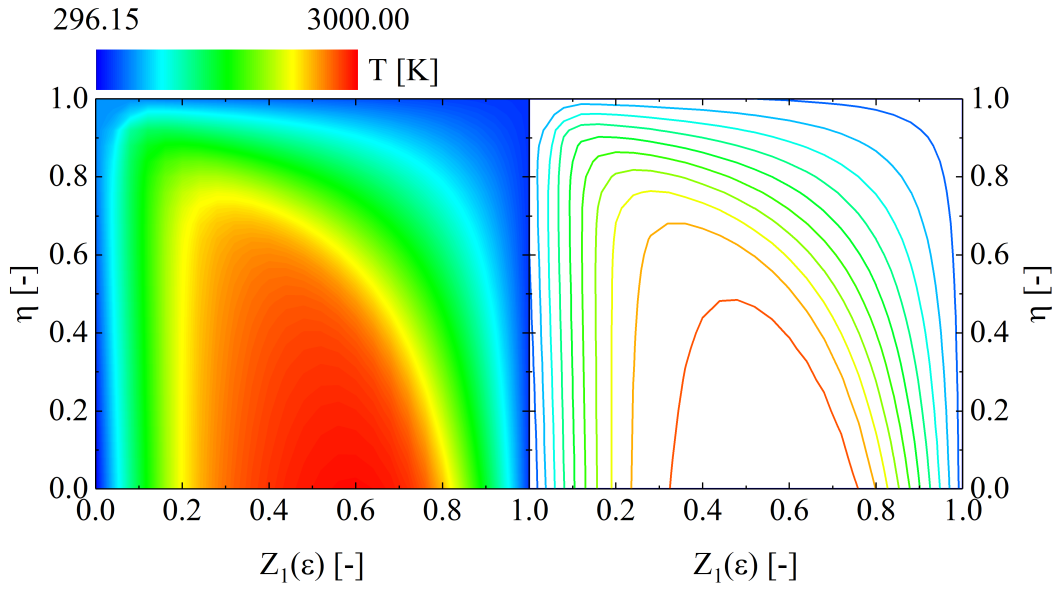

(a) Flamelet result from the 2DF formulations.

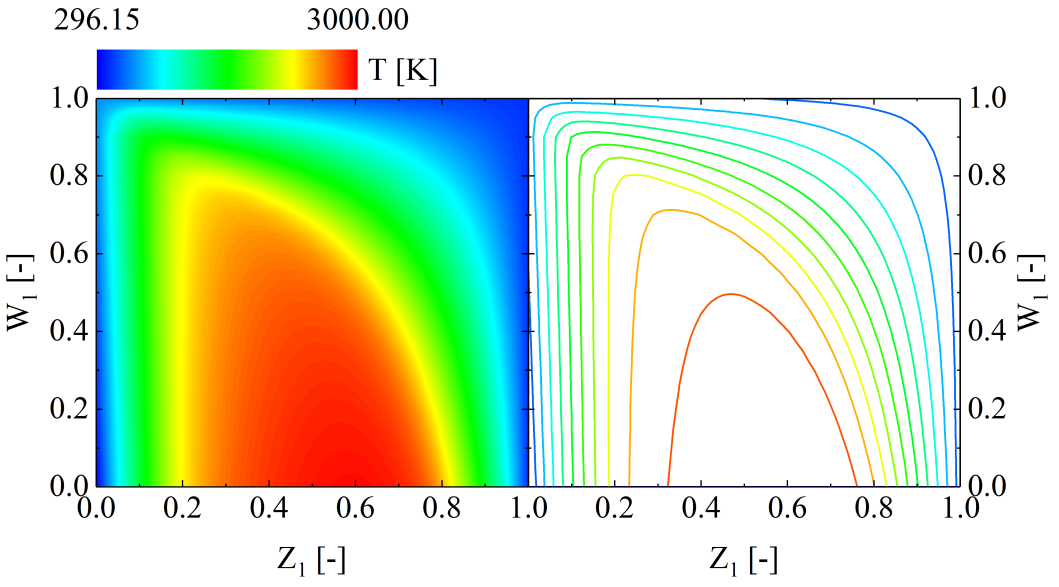

(b) Flamelet result from the Q2DF1 formulations.

Fig. 4.11 Comparisons of flamelet results of the Q2DF1 and 2DF models with regard to temperature evaluated at constant reference stoichiometric scalar dissipation rates: (a) the 2DF model with reference scalar dissipation rates for Z_1, Z_2 and Z_3 are all unity and (b) the Q2DF1 model with a reference scalar dissipation rate of unity.

This transformation is identical with the Q2DF2 model in terms of the space $Z \times W_2$ according to Eqs. (4.5) and (4.6). If the transformation was implemented as

$$\varepsilon = \frac{Z_1}{Z_1 + Z_2}, \eta = Z_3. \tag{4.23}$$

then it would be an expression of the set of independent coordinates for the Q2DF3 model. Based on these transformations, the same comparisons can be made between the 2DF model and the corresponding Q2DF models. The flamelet formulations are essentially described by Eqs. (3.8) and (3.9) for the 2DF model, and there should be no impact from the set of independent coordinates on the results as there are no additional assumptions made in the solving processes. However, different transformed coordinates result in different databases and lookup procedure for the Q2DF models. This is partially attributed to the treatments of scalar and cross-scalar dissipation rates in the cases. Moreover, in the Q2DF models, the diluent fraction is a discrete parameter, which is different from η in the transformed 2DF model. It is clear that the Q2DF models proposed in the current study are essentially the 2DF model in which the scalar and cross-scalar dissipation rates are incompletely considered, and η is treated as a discrete parameter. To improve the model, more scalar dissipation rates should be taken into consideration, however, the dimensions of the library will be vastly increased, especially for LES, if a complete 2DF model library would be established. In this case, a reduction in the dimensions would be important.

Chapter 5

Conclusions

The aims of this thesis are to develop a flamelet model for a three-feed non-premixed combution system. In order to carry out the validation, DNS and LES for turbulent combustion are implemented. A priori test for the FPV has been implemented to check whether it is suitable to handle the syngas combustion in chapter 2. Then in chapter 3 three Q2DF models have been proposed for the three mixture fraction space, and have been further validated by comparisons between the instatantaneous variables and time-averaged variables. Afterwards, in chapter 4, LES modeling of the tracking parameters are properly presented for the Q2DF2 model and the Q2DF3 model. Comparisons have been made to analyze the deviations betweem the exprimental results and Q2DF model cases, as well as to discuss the differences among the three Q2DF model. In this chapter, the results obtained in previous chapters are presented and summarized. Finally, future work is suggested to close this chapter.

5.1 The performance of the FPV on sysgas reactions

In the priori test a detailed mechansim which includes 257 species and 2216 reactions is coupled by an extended FPV to simulate the HCOG reforming results. Extension was made to handle the tarry species representatives since they are PAH from C9 to C30. But this extension will not change the nature of the FPV in terms of chemical features of other species. It has been confirmed that the FPV can capture the syngas combustion well and can be used as a basis of the extension for the three-feed non-premixed combustion system. In addition, the extension can be used in the case in which the coal tar was considered in the raw syngas.

5.2 The Q2DF models in DNS and LES

Three models have been proposed for a three-feed non-premixed combustion system. By assuming the scalar dissipation rate of the third stream is zero in the three-feed counterflow system, the two-dimensional flamelet model is reduced to a one-dimensional flamelet mdoel. Three reducing options result in three models, which are called the quasi-two-dimensional flamelet model and abbreviated as Q2DF. Firstly, they were validated by DNS without any turbulence model. In the DNS, a DNS coupled with Arrhenius formation was used as a reference case. The comparisons are made for both instantaneous variables and time-averaged variables. It has been confirmed that three Q2DF models can basically represent the characteristics in the reference case. And the three Q2DF can also obtain very good agreements in terms of the time-averaged temperature and the concentrations of the major species. However, there are deviations occurred with regard to the RMS fluctuations. The performances of the three Q2DF models are not apparent when the difference of the fluxes for the three streams is small.

The LES modelings for the tracking parameters were proposed by directly connecting the three mixture fractions, rather than solving extra transport equations. The comparisons made between experimental data and LES results indicate those LES modeling for the tracking parameters are effective and accurate. In the LES the flux of the diluent stream is quite large and much more than the fuel stream, which results in the Q2DF3 model outperform the other two models. Moreover, the Q2DF1 case has no advantages in the LES in this work. It is concluded that the dominant mixture fracion in the flow field affects the models vastly. The mixtrue fraction of the diluent stream will has direct impact on the diluent fraction in Q2DF3 model, while the mixtrue fraction of the fuel stream influence the Q2DF1 greatlysince it equals to the mixture fraction in the reduced two-feed counterflow system in Q2DF1 model. Hence, the Q2DF2 model compromises the two cases.

5.3 The essence of the Q2DF models

In the process of the models valiation, both the DNS and LES, the deviations can be observed, although they are small. These deviations illustrate the models themsevles still have room to improve. It can be seen that the treatments of the cross-scalar dissipation rates in the Q2DF models have difference with the three-feed counterflow system, indicating the difference between Q2DF models and the 2DF model. This

difference is not out of the expectation since the three Q2DF models are derived from the 2DF based on some assumptions. In the three-feed counterflow system, the cross-scalar dissipation rate between any two streams can be positive or negetive. However, since the three-feed counterflow system has been reduced to two-feed counterflow system in the Q2DF models, the cross-scalar dissipation rates are changed greatly. The cross-scalar dissipation rate between fuel and oxidizer is always negetive in the Q2DF models. In addition, the mixture in one or two sides contains one or two-stream compositions, and it affects the cross-scalar dissipation rate. In the Q2DF1 model, the diluent and oxygen form a mixture and the fuel and diluent streams in the Q2DF2 model is also a mixture. As in the Q2DF3 model, the mixtures for the fuel and oxidizer sides both include the diluent. In one mixture, the mixture fraction dissipates in the same direction locally. The arrangement of the counterflow makes the cross-scalar dissipation rate for oxygen and the diluent positive, whereas it is negative for the diluent and fuel in the Q2DF1 model. In the same way, for the Q2DF2 model, the cross-scalar dissipation rate is positive for the diluent and the fuel, and it is negative for the diluent and oxygen. In the Q2DF3 model, however, the cross-scalar dissipation rates for the diluent and any reactant stream can be both positive and negative. It should be noted that the three Q2DF models are proposed based on a zero χ_3 assumption, according to the inherent scalar dissipation rates for the three streams, however, only the Q2DF3 model observe the pre-assumption. And the χ_3 is not zero after the reducing of the two-dimenisonal flamelet formulations for the Q2DF1 and Q2DF2 models, which makes the reduced one-dimensional flamelet formulations are invalid. The one-dimensional flamelet formulations for the Q2DF1 and Q2DF2 are valid only when the χ_3 itself is very small in the flow field thus it can be ignored.

Furthermore, the inherent correlations for the three scalar dissipation rates actaully limit the models, and this also give rise to the difference between the Q2DF models and the 2DF. By means of solving the 2DF formulations, the difference between the Q2DF models and the 2DF models can be further investigated. The complete scalar dissipation rates considered in the 2DF model will give a more accurate prediction results in terms of the chemitry events. In addition, in the process of solving the 2DF models, necessary transformations have to be made. It is found the diluent fraction exactly equals to one of the transformed new set of the independent coordinates. However, it should be noted that diluent fracions in the Q2DF models are discrete parameter, whereas in the 2DF model transformed format, it is continuously distributed. Therefore, the Q2DF models in this work are essentially

the 2DF models with the scalar dissipation rates are considered incompletely and the diluent fraction is treated as a discrete parameter.

5.4 Future work

It is considered that the 2DF model has taken the complete scalar dissipation rates into accounts and the diluent fraction is continuously distributed. Therefore, it is reasonable to solve the 2DF model directly and generete library for the LES. However, in the two-dimensional flamelet model library, the dimensions should be paid much attention. Two mixture fracions with their two moments require four dimensions. If a joint probability density fuction is considered then the covariance is needed, which means only for the mixture fractions there are five dimensions. Taking three scalar dissipation rates into accounts, then an entire eight-dimensional library in the complete two-dimensional flamelet model, which is unacceptable at present. So in the future work, the reduction of the dimensions in the two-dimensional flamelet library is essential. And in order to reduce the dimensions, the investigation of the characteristics of a specific flow field is important.

References

[1] E. I. A. (US), G. P. Office, International Energy Outlook 2016: With Projections to 2040, Government Printing Office, 2016.

[2] H. Watanabe, K. Tanno, H. Umetsu, S. Umemoto, Modeling and simulation of coal gasification on an entrained flow coal gasifier with a recycled CO2 injection, Fuel 142 (2015) 250–259.

[3] Y. Oki, J. Inumaru, S. Hara, M. Kobayashi, H. Watanabe, S. Umemoto, H. Makino, Development of oxy-fuel IGCC system with CO2 recirculation for CO2 capture, Energy Procedia 4 (2011) 1066–1073.

[4] H. Watanabe, S. Ahn, K. Tanno, Numerical investigation of effects of CO2 recirculation in an oxy-fuel IGCC on gasification characteristics of a two-stage entrained flow coal gasifier, Energy 118 (2017) 181–189.

[5] S. Patankar, Numerical heat transfer and fluid flow, CRC press, 1980.

[6] B. Cuenot, The flamelet model for non-premixed combustion, in: Turbulent Combustion Modeling, Springer, 2011, pp. 43–61.

[7] N. Peters, Laminar diffusion flamelet models in non-premixed turbulent combustion, Progress in energy and combustion science 10 (3) (1984) 319–339.

[8] N. Peters, Turbulent combustion, Cambridge university press, 2000.

[9] H. Pitsch, Large-eddy simulation of turbulent combustion, Annu. Rev. Fluid Mech. 38 (2006) 453–482.

[10] T. Poinsot, D. Veynante, Theoretical and numerical combustion, RT Edwards, Inc., 2005.

[11] H. Pitsch, N. Peters, A consistent flamelet formulation for non-premixed combustion considering differential diffusion effects, Combustion and flame 114 (1-2) (1998) 26–40.

[12] H. Pitsch, Creating flamelet library for the steady flamelet model or the flamelet/progress variable approach, A c++ computer program for 0-D and 1-D laminar flame calculations (2006).

[13] C. D. Pierce, P. Moin, Progress-variable approach for large-eddy simulation of non-premixed turbulent combustion, Journal of Fluid Mechanics 504 (2004) 73–97.

[14] M. Ihme, H. Pitsch, Prediction of extinction and reignition in nonpremixed turbulent flames using a flamelet/progress variable model: 1. a priori study and presumed pdf closure, Combustion and flame 155 (1-2) (2008) 70–89.

[15] M. Ihme, Pollutant formation and noise emission in turbulent non-premixed flames, Vol. 68, 2007.

[16] E. Knudsen, H. Pitsch, A general flamelet transformation useful for distinguishing between premixed and non-premixed modes of combustion, Combustion and flame 156 (3) (2009) 678–696.

[17] M. Ihme, L. Shunn, J. Zhang, Regularization of reaction progress variable for application to flamelet-based combustion models, Journal of Computational Physics 231 (23) (2012) 7715–7721.

[18] Y. Baba, R. Kurose, Analysis and flamelet modelling for spray combustion, Journal of Fluid Mechanics 612 (2008) 45–79.

[19] H. Moriai, R. Kurose, H. Watanabe, Y. Yano, F. Akamatsu, S. Komori, Large-eddy simulation of turbulent spray combustion in a subscale aircraft jet engine combustor—predictions of no and soot concentrations, Journal of Engineering for Gas Turbines and Power 135 (9) (2013) 091503.

[20] R. Kurose, H. Makino, Large eddy simulation of a solid-fuel jet flame, Combustion and Flame 135 (1-2) (2003) 1–16.

[21] O. Stein, G. Olenik, A. Kronenburg, F. C. Marincola, B. Franchetti, A. Kempf, M. Ghiani, M. Vascellari, C. Hasse, Towards comprehensive coal combustion modelling for LES, Flow, turbulence and combustion 90 (4) (2013) 859–884.

[22] H. Watanabe, R. Kurose, S. Komori, H. Pitsch, Effects of radiation on spray flame characteristics and soot formation, Combustion and Flame 152 (1) (2008) 2–13.

[23] A. Fujita, H. Watanabe, R. Kurose, S. Komori, Two-dimensional direct numerical simulation of spray flames-part 1: Effects of equivalence ratio, fuel droplet size and radiation, and validity of flamelet model, Fuel 104 (2013) 515–525.

[24] Y. Hu, R. Kurose, Nonpremixed and premixed flamelets LES of partially premixed spray flames using a two-phase transport equation of progress variable, Combustion and Flame 188 (2018) 227–242.

[25] L. Shunn, P. Moin, Large-eddy simulation of combustion systems with convective heat-loss, Ph.D. thesis; Stanford University, 2009.

[26] D. Carbonell, C. D. Perez-Segarra, P. Coelho, A. Oliva, Flamelet mathematical models for non-premixed laminar combustion, Combustion and Flame 156 (2) (2009) 334–347.

[27] L. Ma, D. Roekaerts, Modeling of spray jet flame under MILD condition with non-adiabatic fgm and a new conditional droplet injection model, Combustion and Flame 165 (2016) 402–423.

[28] H. Pitsch, M. Ihme, An unsteady/flamelet progress variable method for LES of nonpremixed turbulent combustion, in: 43rd AIAA Aerospace Sciences Meeting and Exhibit, 2005, p. 557.

[29] M. Ihme, Y. C. See, Prediction of autoignition in a lifted methane/air flame using an unsteady flamelet/progress variable model, Combustion and Flame 157 (10) (2010) 1850–1862.

[30] Y. Hu, R. Kurose, Large-eddy simulation of turbulent autoigniting hydrogen lifted jet flame with a multi-regime flamelet approach, International Journal of Hydrogen Energy 44 (12) (2019) 6313–6324.

[31] A. Cavaliere, M. de Joannon, Mild combustion, Progress in Energy and Combustion science 30 (4) (2004) 329–366.

[32] T. Plessing, N. Peters, J. G. Wünning, Laseroptical investigation of highly preheated combustion with strong exhaust gas recirculation, in: Symposium (International) on combustion, Vol. 27, Elsevier, 1998, pp. 3197–3204.

[33] I. Özdemir, N. Peters, Characteristics of the reaction zone in a combustor operating at mild combustion, Experiments in fluids 30 (6) (2001) 683–695.

[34] Y. Minamoto, N. Swaminathan, Scalar gradient behaviour in MILD combustion, Combustion and Flame 161 (4) (2014) 1063–1075.

[35] Y. Minamoto, N. Swaminathan, R. S. Cant, T. Leung, Reaction zones and their structure in MILD combustion, Combustion Science and Technology 186 (8) (2014) 1075–1096.

[36] B. B. Dally, A. Karpetis, R. Barlow, Structure of turbulent non-premixed jet flames in a diluted hot coflow, Proceedings of the combustion institute 29 (1) (2002) 1147–1154.

[37] F. C. Christo, B. B. Dally, Modeling turbulent reacting jets issuing into a hot and diluted coflow, Combustion and flame 142 (1-2) (2005) 117–129.

[38] M. Ihme, Y. C. See, Les flamelet modeling of a three-stream MILD combustor: Analysis of flame sensitivity to scalar inflow conditions, Proceedings of the Combustion Institute 33 (1) (2011) 1309–1317.

[39] M. Ihme, J. Zhang, G. He, B. Dally, Large-eddy simulation of a jet-in-hot-coflow burner operating in the oxygen-diluted combustion regime, Flow, turbulence and combustion 89 (3) (2012) 449–464.

[40] X. Huang, M. Tummers, D. Roekaerts, Experimental and numerical study of MILD combustion in a lab-scale furnace, Energy Procedia 120 (2017) 395–402.

[41] C. Hasse, N. Peters, A two mixture fraction flamelet model applied to split injections in a DI diesel engine, Proceedings of the Combustion Institute 30 (2) (2005) 2755–2762.

[42] C. Felsch, M. Gauding, C. Hasse, S. Vogel, N. Peters, An extended flamelet model for multiple injections in DI diesel engines, Proceedings of the Combustion Institute 32 (2) (2009) 2775–2783.

[43] H. Barths, H. Pitsch, N. Peters, 3D simulation of DI diesel combustion and pollutant formation using a two-component reference fuel, Oil & Gas science and technology 54 (2) (1999) 233–244.

[44] E. M. Doran, H. Pitsch, D. J. Cook, A priori testing of a two-dimensional unsteady flamelet model for three-feed combustion systems, Proceedings of the Combustion Institute 34 (1) (2013) 1317–1324.

[45] J. Watanabe, K. Yamamoto, Flamelet model for pulverized coal combustion, Proceedings of the Combustion Institute 35 (2) (2015) 2315–2322.

[46] J. Watanabe, T. Okazaki, K. Yamamoto, K. Kuramashi, A. Baba, Large-eddy simulation of pulverized coal combustion using flamelet model, Proceedings of the Combustion Institute 36 (2) (2017) 2155–2163.

[47] M. Rieth, F. Proch, M. Rabaçal, B. Franchetti, F. C. Marincola, A. Kempf, Flamelet LES of a semi-industrial pulverized coal furnace, Combustion and Flame 173 (2016) 39–56.

[48] Coal statistic; 2010, <http://www.worldcoal.org/resources/carbon/coal-statistics/>, [accessed December 20th, 2016].

[49] T. Aramaki, Status of the coke oven gas in japan, Nihon Enerugi Gakkaishi/Journal of the Japan Institute of Energy 85 (5) (2006) 342–347.

[50] R. Razzaq, C. Li, S. Zhang, Coke oven gas: Availability, properties, purification, and utilization in china, Fuel 113 (2013) 287 – 299.

[51] A. Jess, Mechanisms and kinetics of thermal reactions of aromatic hydrocarbons from pyrolysis of solid fuels, Fuel 75 (12) (1996) 1441 – 1448.

[52] K. Norinaga, Y. Sakurai, R. Sato, J. ichiro Hayashi, Numerical simulation of thermal conversion of aromatic hydrocarbons in the presence of hydrogen and steam using a detailed chemical kinetic model, Chemical Engineering Journal 178 (2011) 282 – 290.

[53] K. Norinaga, J.-i. Hayashi, Numerical simulation of the partial oxidation of hot coke oven gas with a detailed chemical kinetic model†, Energy & Fuels 24 (1) (2009) 165–172.

[54] K. Norinaga, H. Yatabe, M. Matsuoka, J.-i. Hayashi, Application of an existing detailed chemical kinetic model to a practical system of hot coke oven gas reforming by noncatalytic partial oxidation, Industrial & Engineering Chemistry Research 49 (21) (2010) 10565–10571.

[55] S. Appari, R. Tanaka, C. Li, S. Kudo, J.-i. Hayashi, V. M. Janardhanan, H. Watanabe, K. Norinaga, Predicting the temperature and reactant concentration profiles of reacting flow in the partial oxidation of hot coke oven gas using detailed chemistry and a one-dimensional flow model, Chemical Engineering Journal 266 (2015) 82–90.

[56] C. Li, S. Appari, R. Tanaka, K. Hanao, Y. Lee, S. Kudo, J.-i. Hayashi, V. M. Janardhanan, H. Watanabe, K. Norinaga, A CFD study on the reacting flow of partially combusting hot coke oven gas in a bench-scale reformer, Fuel 159 (2015) 590–598.

[57] J. Truelove, Discrete-ordinate solutions of the radiation transport equation, Journal of Heat Transfer (Transcations of the ASME (American Society of Mechanical Engineers), Series C);(United States) 109 (4) (1987).

[58] W. Fiveland, Three-dimensional radiative heat-transfer solutions by the discrete-ordinates method, Journal of Thermophysics and Heat Transfer 2 (4) (1988) 309–316.

[59] P. Moin, K. Squires, W. Cabot, S. Lee, A dynamic subgrid-scale model for compressible turbulence and scalar transport, Physics of Fluids A: Fluid Dynamics 3 (11) (1991) 2746–2757.

[60] T. Poinsot, D. Veynante, Theoretical and numerical combustion, R.T. Edwards, Inc., Philadelphia, PA, 2001.

[61] D. Veynante, L. Vervisch, Turbulent combustion modeling, Progress in Energy and Combustion Science 28 (3) (2002) 193 – 266. doi:https://doi.org/10.1016/S0360-1285(01)00017-X.
URL http://www.sciencedirect.com/science/article/pii/S036012850100017X

[62] H. Pitsch, H. Steiner, Large-eddy simulation of a turbulent piloted methane/air diffusion flame (sandia flame D), Physics of fluids 12 (10) (2000) 2541–2554.

[63] A. Kishimoto, H. Moriai, K. Takenaka, T. Nishiie, M. Adachi, A. Ogawara, R. Kurose, Application of a non-adiabatic flamelet/progress-variable approach to les of H2/O2 combustion under a pressurized condition, Journal of Heat Transfer.

[64] M. Muto, H. Watanabe, R. Kurose, S. Komori, S. Balusamy, S. Hochgreb, Large-eddy simulation of pulverized coal jet flame–effect of oxygen concentration on NOx formation, Fuel 142 (2015) 152–163.

[65] S. Ahn, K. Tanno, H. Watanabe, Numerical analysis of particle dispersion and combustion characteristics on a piloted coaxial pulverized coal jet flame, Applied Thermal Engineering 124 (2017) 1194–1202.

[66] H. Pitsch, A C++ computer program for 0-D combustion and 1-D laminar flame calculation, rWTH Aachen, Aachen, Germany. (1998).

[67] H. Richter, J. B. Howard, Formation and consumption of single-ring aromatic hydrocarbons and their precursors in premixed acetylene, ethylene and benzene flames, Physical Chemistry Chemical Physics 4 (11) (2002) 2038–2055.

[68] M. Ihme, H. Pitsch, Modeling of radiation and nitric oxide formation in turbulent nonpremixed flames using a flamelet/progress variable formulation, Physics of Fluids (1994-present) 20 (5) (2008) 055110.

[69] I. Danaila, B. Boersma, Mode interaction in a forced homogeneous jet at low reynolds numbers, Proc. Summer Prog. Center Turbul. Res (1998) 141–58.

[70] G.-S. Jiang, C.-W. Shu, Efficient implementation of weighted ENO schemes, Journal of computational physics 126 (1) (1996) 202–228.

[71] P. Coelho, N. Peters, Numerical simulation of a mild combustion burner, Combustion and flame 124 (3) (2001) 503–518.

[72] G. P. Smith, D. M. Golden, M. Frenklach, N. W. Moriarty, B. Eiteneer, M. Goldenberg, C. T. Bowman, R. K. Hanson, S. Song, W. Gardiner Jr, et al., Gri-mech 3.0, 1999, URL http://combustion.berkeley.edu/gri-mech/ (2011).

[73] T. Kitano, T. Nakatani, R. Kurose, S. Komori, Two-dimensional direct numerical simulation of spray flames–part 2: Effects of ambient pressure and lift, and validity of flamelet model, Fuel 104 (2013) 526–535.

[74] H. Watanabe, R. Kurose, M. Hayashi, T. Kitano, S. Komori, Effects of ambient pressure and precursors on soot formation in spray flames, Advanced Powder Technology 25 (4) (2014) 1376–1387.

[75] T. Hara, M. Muto, T. Kitano, R. Kurose, S. Komori, Direct numerical simulation of a pulverized coal jet flame employing a global volatile matter reaction scheme based on detailed reaction mechanism, Combustion and Flame 162 (12) (2015) 4391–4407.

[76] T. Kitano, T. Tsuji, R. Kurose, S. Komori, Effect of pressure oscillations on flashback characteristics in a turbulent channel flow, Energy & Fuels 29 (10) (2015) 6815–6822.

[77] A. L. Pillai, R. Kurose, Numerical investigation of combustion noise in an open turbulent spray flame, Applied Acoustics 133 (2018) 16–27.

[78] V. Moureau, C. Bérat, H. Pitsch, An efficient semi-implicit compressible solver for large-eddy simulations, Journal of Computational Physics 226 (2) (2007) 1256–1270.

[79] H. Watanabe, R. Kurose, S.-M. Hwang, F. Akamatsu, Characteristics of flamelets in spray flames formed in a laminar counterflow, Combustion and Flame 148 (4) (2007) 234–248.

[80] M. Ihme, H. Pitsch, Prediction of extinction and reignition in nonpremixed turbulent flames using a flamelet/progress variable model: 1. a priori study and presumed PDF closure, Combustion and flame 155 (1-2) (2008) 70–89.

[81] M. Ihme, H. Pitsch, Prediction of extinction and reignition in nonpremixed turbulent flames using a flamelet/progress variable model: 2. application in LES of sandia flames D and E, Combustion and flame 155 (1-2) (2008) 90–107.

[82] I. Yuri, H. Nishida, Characteristics of coal gasified fuel oxy-combustion in H2O/CO2 (emission characteristics of nh3 contained coal gasified fuel)(in japanese), https://doi.org/10.1299/jsmemecj.2016.S0810107 (2016).

[83] I. Yuri, H. Nishida, Characteristics if coal gasified fuel oxy-combustion in H2O/CO2 (effect of exhaust recirculation on exhaust gas composition)(in japanese), https://doi.org/10.1299/jsmemecj.2017.S0810104 (2017).

[84] E. M. Doran, A multi-dimensional flamelet model for ignition in multi-feed combustion systems, Stanford University, 2011.

Appendix A

Modeling of the tracking parameters in the LES

For the Q2DF3 LES modeling, two options have been proposed in chapter 4 in terms of $\widetilde{Z}$ and $\widetilde{Z''^2}$. The first one is the approach in the literature [39], here only the derivation of the transport equation of Z is presented in detail in this appendix since the LES modelings were not adopted. The basic equations for Z_1 and Z_2 are given as

$$\frac{\partial \rho Z_1}{\partial t} + \frac{\partial \rho u_i Z_1}{\partial x_i} = \frac{\partial}{\partial x_i}\left(\rho D \frac{\partial Z_1}{\partial x_i}\right), \tag{A.1}$$

$$\frac{\partial \rho Z_3}{\partial t} + \frac{\partial \rho u_i Z_3}{\partial x_i} = \frac{\partial}{\partial x_i}\left(\rho D \frac{\partial Z_3}{\partial x_i}\right). \tag{A.2}$$

Repalce the Z_1 in Eq A.1 by $Z(1-Z_3)$. Then it can be transferred to

$$\underbrace{\rho \frac{\partial Z(1-Z_3)}{\partial t}}_{U} + \underbrace{\rho \frac{\partial u_i Z(1-Z_3)}{\partial x_i}}_{C} = \underbrace{\frac{\partial}{\partial x_i}\left(\rho D \frac{\partial Z(1-Z_3)}{\partial x_i}\right)}_{D}, \tag{A.3}$$

here for each term the extension can be made as below:

$$U = \rho Z \frac{\partial (1-Z_3)}{\partial t} + \rho (1-Z_3)\frac{\partial Z}{\partial t} = -\rho Z \frac{\partial Z_3}{\partial t} + \rho \frac{\partial Z}{\partial t} - \rho Z_3 \frac{\partial Z}{\partial t}, \tag{A.4}$$

$$C = -\rho Z u_i \frac{\partial Z_3}{\partial x_i} + (1-Z_3)\rho u_i \frac{\partial Z}{\partial x_i} = -\rho Z u_i \frac{\partial Z_3}{\partial x_i} + \rho u_i \frac{\partial Z}{\partial x_i} - \rho u_i Z_3 \frac{\partial Z}{\partial x_i}, \tag{A.5}$$

$$
\begin{aligned}
D &= \frac{\partial}{\partial x_i}\left(\rho DZ\frac{\partial(1-Z_3)}{\partial x_i}\right)+\frac{\partial}{\partial x_i}\left(\rho D(1-Z_3)\frac{\partial Z}{\partial x_i}\right)\\
&= -Z\frac{\partial}{\partial x_i}\left(\rho D\frac{\partial Z_3}{\partial x_i}\right)-\rho D\frac{\partial Z_3}{\partial x_i}\frac{\partial Z}{\partial x_i}\\
&+\frac{\partial}{\partial x_i}\left(\rho D\frac{\partial Z}{\partial x_i}\right)-Z_3\frac{\partial}{\partial x_i}\left(\rho D\frac{\partial Z}{\partial x_i}\right)-\rho D\frac{\partial Z}{\partial x_i}\frac{\partial Z_3}{\partial x_i},
\end{aligned}
\tag{A.6}
$$

Combine the Eqs. (A.2), (A.4), (A.5) and (A.6), then

$$
\frac{\partial\rho Z}{\partial t}+\frac{\partial(\rho u_i Z)}{\partial x_i}=\frac{\partial}{\partial x_i}\left(\rho D_Z\frac{\partial Z}{\partial x_i}\right)-\frac{2}{1-Z_3}\rho D_Z\frac{\partial Z_3}{\partial x_i}\frac{\partial Z}{\partial x_i}. \tag{A.7}
$$

Since the modelings used in this work was not according to the literature [39], it is necessary to give the detailed information how the modelings are derived. A very important rule should keep in mind is one of the Maclaurin Series

$$
\frac{1}{1-x}=\sum_{i=0}^{\infty}x^i,(|x|<1). \tag{A.8}
$$

In addition, the connection between the Favre-filtered, the residual fluctuation mentioned in chapter 4 is essential to derive the connections between the variances

$$
\widetilde{Z_1''Z_3''}=0.5\times\left(\widetilde{Z_2''^2}-\widetilde{Z_1''^2}-\widetilde{Z_3''^2}\right). \tag{A.9}
$$

The special case when Z_3 is unity can be considered seperately. Z expressed by Z_1 and Z_3 can be expanded as following

$$
\begin{aligned}
\widetilde{\frac{Z_1}{1-Z_3}} &= Z_1\left(1+Z_3+Z_3^2+\widetilde{Z_3^3+Z_3^4}+...+Z_3^n+...\right)\\
&= Z_1+Z_1Z_3+Z_1Z_3^2+Z_1\widetilde{Z_3^3+Z_1Z_3^4}+...+Z_1Z_3^n+...
\end{aligned}
\tag{A.10}
$$

.

For each term, discard the terms $\widetilde{(Z_1 Z_3^n)''}\widetilde{Z_3''}$ (n = 1, 2, 3, ...) since they are tiny values.

$$\begin{aligned}
\widetilde{Z_1 Z_3} &= \widetilde{Z}_1\widetilde{Z}_3 + \widetilde{Z_1'' Z_3''} \\
\widetilde{Z_1 Z_3^2} &= \widetilde{(Z_1 Z_3) Z_3} \\
&= \widetilde{Z_1 Z_3}\widetilde{Z}_3 + \widetilde{(Z_1 Z_3)''}\widetilde{Z_3''} \\
&\approx \widetilde{Z_1 Z_3}\widetilde{Z}_3 \\
\widetilde{Z_1 Z_3^3} &= \widetilde{(Z_1 Z_3^2) Z_3} \\
&= \widetilde{Z_1 Z_3^2}\widetilde{Z}_3 + \widetilde{(Z_1 Z_3^2)''}\widetilde{Z_3''} \\
&= \widetilde{Z_1 Z_3}(\widetilde{Z}_3)^2 + \widetilde{(Z_1 Z_3)''} Z_3''\widetilde{Z}_3 + \widetilde{(Z_1 Z_3^2)''}\widetilde{Z_3''} \\
&\approx \widetilde{Z_1 Z_3}(\widetilde{Z}_3)^2 \\
\widetilde{Z_1 Z_3^n} &\approx \widetilde{Z_1 Z_3}(\widetilde{Z}_3)^{n-1}
\end{aligned} \tag{A.11}$$

Place each term in Eq. (A.11) back to Eq. (A.10) then we obtain

$$\begin{aligned}
\frac{\widetilde{Z_1}}{1-Z_3} &= Z_1\left(1 + Z_3 + Z_3^2 + \widetilde{Z_3^3 + Z_3^4} + ... + Z_3^n + ...\right) \\
&= \widetilde{Z}_1 + \widetilde{Z_1 Z_3}\left(1 + \widetilde{Z}_3 + \widetilde{Z}_3{}^2 + \widetilde{Z}_3{}^3 + \widetilde{Z}_3{}^4 + ... + \widetilde{Z}_3{}^n + ...\right) \\
&= \widetilde{Z}_1 + \frac{\widetilde{Z_1 Z_3}}{1-\widetilde{Z}_3} \\
&= \frac{\widetilde{Z}_1}{1-\widetilde{Z}_3} + 0.5 \times \frac{\widetilde{Z_2''^2} - \widetilde{Z_1''^2} - \widetilde{Z_3''^2}}{1-\widetilde{Z}_3}.
\end{aligned} \tag{A.12}$$

For the variance of Z, the Maclaurin Series and Eq. (A.9) are also very important. It is reasonable that the very small terms $(Z_1 Z_3^n)''$ (n = 2, 3, 4, ...) here are also neglected.

$$\begin{aligned}
\left(\frac{Z_1}{1-Z_3}\right)'' &= \left[Z_1\left(1 + Z_3 + Z_3^2 + Z_3^3 + Z_3^4 + ... + Z_3^n + ...\right)\right]'' \\
&= Z_1'' + (Z_1 Z_3)'' + (Z_1 Z_3^2)'' + (Z_1 Z_3^3 + Z_1 Z_3^4)'' + ... + (Z_1 Z_3^n)'' + ... \\
&\approx Z_1'' + (Z_1 Z_3)''.
\end{aligned} \tag{A.13}$$

As for the last term in Eq. (A.13)

$$\begin{aligned}(Z_1Z_3)'' &= Z_1Z_3 - \widetilde{Z}_1\widetilde{Z}_3 - \widetilde{Z_1''Z_3''} \\ &= Z_1(\widetilde{Z}_3 + Z_3'') - \widetilde{Z}_1\widetilde{Z}_3 - \widetilde{Z_1''Z_3''} \\ &= Z_1''\widetilde{Z}_3 + \widetilde{Z}_1Z_3'' + Z_1''Z_3'' - \widetilde{Z_1''Z_3''}.\end{aligned} \tag{A.14}$$

So the Eq. (A.13) can be calculated as

$$\left(\frac{Z_1}{1-Z_3}\right)'' \approx Z_1'' + Z_1''\widetilde{Z}_3 + \widetilde{Z}_1Z_3'' + Z_1''Z_3'' - \widetilde{Z_1''Z_3''}. \tag{A.15}$$

The square of the Eq. (A.15) will generate a sum of 25 terms, and ignore very small terms then

$$\widetilde{\left(\frac{Z_1}{1-Z_3}\right)}^{''2} = \left(1+\widetilde{Z}_3\right)\left(1+\widetilde{Z}_3-\widetilde{Z}_1\right)\widetilde{Z_1''^2} + \widetilde{Z}_1\left(1+\widetilde{Z}_3\right)\widetilde{Z_2''^2} - \widetilde{Z}_1\left(1+\widetilde{Z}_3-\widetilde{Z}_1\right)\widetilde{Z_3''^2}. \tag{A.16}$$

Appendix B

List of Publications

The results of this thesis have been published and submitted in the following journal articles:

1. Yu P, Norinaga K, Watanabe H, et al. Prediction of hot coke oven gas reforming by LES coupled with the extended flamelet/progress variable approach[J]. *Fuel*, 2018, 231: 234-243.
2. Yu P, Watanabe H, Zhang W, et al. Flamelet model for a three-feed non-premixed combustion system with diluent stream: Analysis and validation of quasi-two-dimensional flamelet (Q2DF) models[J]. *Energy & Fuels*, 2019.
3. Yu P, Watanabe H, Yuri Isao, et al. LES of oxy-fuel combustion on a three-feed non-premixed swirling burner by the quasi-two-dimensional flamelet model, *Combustion and Flame*, submitted, July, 2019.

and presented in the following conferences:

1. Panlong Yu, Koyo Norinaga, Hiroaki Watanabe, Toshiaki Kitagawa. LES coupled with the extended flamelet/progress variable approach for HCOG reforming. *Combustion Society of Japan the 55 th combustion symposium*, Toyamashi, Japan, 2017.
2. Panlong Yu, Hiroaki Watanabe, Ryoichi Kurose, Toshiaki Kitagawa, Flamelet model for a three-feed non-premixed combustion system with diluent stream. *Combustion Society of Japan the 56 th combustion symposium*, Oosaka, Japan, 2018.

3. Panlong Yu, Hiroaki Watanabe, Isao Yuri, Hiroyuki Nishida, Toshiaki Kitagawa. LES of oxy-fuel combustion on a three-feed non-premixed swirling burner with quasi-two-dimensional flamelet model. *International Conference on Numerical Combustion (NC19)*, Aachen, Germany, 2019.